DOCTOR OF PHILOSOPHY

Plasticity length-scale effects fundamentals

dislocation generation and mobility as a function of applied stress distribution and stacking fault energy

Abbassi Monjezi, Mohammadreza

Award date:
2024

Awarding institution:
Coventry University

Plasticity Length-Scale Effects Fundamentals: Dislocation Generation and Mobility as a Function of Applied Stress Distribution and Stacking Fault Energy

Mohammadreza Abbassi

A thesis submitted in partial fulfilment of the University's requirements for the degree of Doctor of Philosophy

December 8, 2023

Supervisory team:
Prof. Nigel Jennett
Dr. Vit Janik
Dr. Xiaodong Hou
Dr. Mingwen Bai

Centre for Materials, Mechanics, and Measurement

Coventry University, United Kingdom

Table of Contents

Declaration:

I, Mohammadreza Abbassi, declare that the PhD thesis entitled “Plasticity length-scale effects fundamentals: dislocation generation and mobility as a function of applied stress distribution and stacking fault energy” is my own and has been generated by me as the result of my own original research works.

To the best of my knowledge and belief, this thesis contains no material previously published or written by another person. The references have been made on the parts which has been taken from other studies.

Signature: Date: 8th December 2023

Acknowledgement:

First and foremost, I am extremely grateful to my supervisors, Prof. Nigel Jennett, Dr. Vit Janik, Dr. Xiadong Hou and Dr. Mingwen Bai for their invaluable advice, unwavering encouragement, and commitment to academic excellence during my PhD study. Their immense knowledge and plentiful experience have shaped both the direction of my research and my personal growth. Without their tremendous understanding and encouragement in the past few years, it would not be impossible for me to complete my study. Additionally, I express my appreciation to managerial team of Faculty of Engineering, Environment and Computing and the personnel of University of Coventry who make it possible for students to have a proper environment to practice research and study.

I would like to express my sincere gratitude to Dr. David Parfitt, Dr. Christophe Bastien and Dr. Ian Dunwell insights and comments who were subject expert and chair in my PRP sessions which helped me to improve this body of work.

I appreciate Dr. Christopher Waldron, Dr. Evans Mogire and Mr. Steven Hindmarsh at University of Warwick for their technical support and giving me the opportunity to use the facilities (EPSRC grant code: EP/V007688/1).

I am deeply grateful to Dr. Helen Ryder and Dr. Elisabeth Francis at University of Manchester for awarding me the funding and the opportunity to perform FIB and TKD using their facilities.

I am thankful to Dr. Thomas Chudoba from Zwick/Roell company and Dr. Andrea Cerreta from Park system company for their useful technical and scientific consultation to get the best out of Nanoindentation and AFM equipment.

I want to thank my examiners of my Viva, Prof. James Marrow of Oxford University and Dr. Niall Smyth of Coventry university for taking their time to go through my work and for their comments which helped this work to become more rigorous.

I thank the PhD researchers of my study group Naresh Radaliyagoda, C.J. Wong, Anuradha Herath, Qamar Hayat and Rohit Sharma for the stimulating discussions, exchange of knowledge and for all the fun we have had throughout our studies.

Last but not the least, I would like to thank my parents and my brothers for supporting me throughout writing this thesis and my life in general.

Abstract:

Over a range from nano to micro, metals display size-dependence when deformed non-uniformly into the plastic range. This is a behavior which cannot be characterized by conventional plasticity theories because they incorporate no material length scale.

This body of work is dedicated to advancing our comprehension of the mechanisms influencing the strength of metallic materials. The focus is on experimental investigations aimed at understanding how the physical dimensions of a structure impact the mechanisms that dictate strength, particularly when the scale of the structure is on the order of a few micrometres and nanometres.

Instrumented Indentation testing (nanoindentation) enables us to obtain valuable information on the mechanical properties of materials, including hardness and modulus and with that various information about microstructure can be disclosed. The test can be done not only bulk materials but also grains, inclusions, or phases too small to be probed by other techniques.

A Berkovich indenter was employed to apply deformation to single crystal metals with high purity (>99.9%) in two crystal structures: body-centred cubic (BCC) and face-centred cubic (FCC) to reduce the number of factors affecting the test results, such as grain boundaries and microstructural defects.

In various studies, only a restricted amount of data has been collected and a model based on the collected data in that regime has been proposed. Later on, the model had to go through modification due to accessible wider range of data or collected data from another material which has shown different response to the performed test. In this work, an attempt was made to cover a wide range single crystal material, and the data was collected in a wide range of indentation depth in order to succeed to give a comprehensive definition of hardness.

The analysis of the collected data was done based on slip-distance theory and using Hou and Jennett [1] model. The analysed data leads to a linear function fitted to the data. The constants of that linear function are indicators of plastic zone size and dislocation density.

It was found that there is a consistent trend in all tested materials that shows a change in plasticity mechanism in regard to length scale. In FCC materials, more than one linear function can be fitted to the data which demonstrates the variety of governing plasticity mechanisms at different length scales, while BCC materials are found to be less pronounced to that. The change can be realized based on change in the contribution of plastic zone size and dislocation density. The ratio of those parameters, which in combination give the hardness, varies in different regimes.

In-depth microstructural analysis was done using Transmission Kikuchi Diffraction (TKD) to characterize the highly deformed areas in nanoscale. Lamellas samples were prepared by in-situ lift-out using a focused-ion-beam scanning electron microscope (FIB-SEM) system from indented materials. The area of interest is the volume below the middle of the indented area to investigate the deformation-induced zone. The result of TKD analysis shows high density geometrically necessary dislocations (GND) in low depth indentation and activation of different slip systems by increasing the indentation depth. Based on TKD images obtained from FCC materials, it was observed that there is a connection between stacking fault energy and plastic zone size. By increasing SFE, the mobility of dislocation increases, and the possibility of dislocation interactions decreases which defers the formation of plastic zone. In low stacking fault energy FCC materials and in BCC materials, a network of dislocations has shaped the plastic zone below the indent. The shape of the plastic zone resembles the shape of the indent.

List of abbreviations and symbols:

α	Indent Tip Contact Radius
Ac	Contact Area of indentation
AFM	Atomic Force Microscopy
b	Burger's Vector
BCC	Body-Centred Cubic
C_T	Contact compliance
C_s	Machine Compliance
C_F	Frame Compliance
C	Element of Stiffness Matrix
E	Elastic Modulus
E_r	Reduced Elastic Modulus
E_{VRH}	Voigt-Reuss-Hill Average Elastic Modulus
EBSD	Electron Backscatter Diffraction
F	Force
FCC	Face-Centred Cubic
FIB	Focused Ion Beam
G	Shear Modulus
GND	Geometry Necessary Dislocation
h_c	Indentation depth
h_f	Final depth of contact impression after unloading
h_{max}	Indenter displacement at maximum load
h_s	Displacement of surface
H	Hardness
HCP	Hexagonal Close-Packed
IIT	Instrument Indentation Testing
ISE	Indentation Size Effect
KAM	Kernel Average Misorientation
S	Stiffness
SEM	Scanning Electron Microscopy

SFE	Stacking Fault Energy
SSD	Statistically Stored Dislocation
TEM	Transmission Electron Microscopy
TKD	Transmission Kikuchi Diffraction

Latin and Greek characters:

ρ_m	Density of Mobile Dislocations
ρ_t	Total Density of Dislocations
ρ_s	Density of Sessile Dislocations
γ	Stacking Fault Energy
ε_{pl}	Plastic Strain
µm	Micrometre
π	Pi
ν	Poisson's ration
τ	Shear stress

Elements:

Ag	Silver
Al	Aluminium
Au	Gold
Cu	Copper
Fe	Iron
Mo	Molybdenum
Nb	Niobium
Ni	Nickel
Ta	Tantalum
V	Vanadium

List of Figures

List of Tables

1. Introduction:

1.1 Material testing to discover material properties:

Metallic materials have intrinsic properties which make them applicable in a wide variety of applications including automotive, aerospace and energy sectors. However, there is an increasing demand for low carbon emission, lightweight structures, high performance, and durability. It thus requires more efforts to further improve mechanical properties of materials and discover deformation mechanisms that occur when they are used in service.

Advanced technology necessitates the reduction of dimensions to a few micrometres or even smaller. Recent progress in the realm of experimental characterization methods, including high-sensitive measurement equipment, and small-scale sample fabrication techniques facilitate the exploration of material properties with diminishing sample dimensions. Advancements in computational capabilities has assisted broadening of the understanding about microstructure down to the size of an individual dislocation. Deformation mechanisms comprehension and mechanical performance assessment at micron and sub-micron scales are pivotal in providing insight that aids in the accomplishment or design of novel material systems possessing superior properties through controlled microstructure at the appropriate scales.

At large scales, the properties of most materials are well-stablished, however, mechanical properties change drastically at micro and nano scales. In the last few decades, several new methods, such as instrumented indentation testing, have been developed and employed to explore materials structure at smaller scales. By gaining a better understanding, changes have been applied to adjust the attributes of these materials. This has enabled the use of many novel methods to further improve the mechanical properties of metallic materials through adjustment in microstructure, strengthening mechanisms, and chemical composition, and more. There is also an increasing interest in the mechanical properties of smaller volumes, as mechanical properties at micro/nano scale may differ from the macro scale properties due to the size effect [2][3][4][5][6][7][8] when plastic deformation is controlled by a limited number of defects.

The size effect remains a challenge since it does not fit into classic mechanics and continuum mechanics theories. In a homogeneous, isotropic material, one would expect consistent values of hardness and modulus. However, experimental results indicate otherwise. Nevertheless, a challenge is also an opportunity to deepen our understanding of materials and to use that to manipulate materials properties for a better use. It can provide a better understanding of plasticity and advance the physical models so that they may include the fundamental materials science of deformation at

small scales. New experimental methods based on extended theories are needed that permit better coupling to all aspects of intrinsic and extrinsic parameters of materials and testing methods. Hence, Nanoindentation gives the opportunity to concentrates stresses in a volume small enough that a defect is unlikely to be present.

This thesis discusses the size effect observed in the strength and plastic deformation of materials at the micron and nano scales, which differ from those of macro-scale and bulk materials. The size effect has been observed in hardness measurements obtained by indentation testing and can be categorized into two groups: intrinsic and extrinsic. Intrinsic size effects are due to microstructural constraints such as grain size and second-phase particles, while extrinsic size effects arise from dimensional constraints due to a sample size. The thesis aims to study the size effects in crystal-plasticity through instrumented indentation testing using a model based on slip distance theory, offering a new way to interpret the length scale size effect by breaking down the concept of hardness into grain size, plastic zone size, and dislocation spacing.

1.2 Crystallography:

In crystalline materials, atoms are arranged periodically and repeatedly over a long atomic distance. This repetitive pattern is divided into unit cell which can represent the whole crystallographic structure.

Most of the metallic materials form one of these three structures: Face-Centred Cubic, Body-Centred Cubic, and Hexagonal Close-Packed crystal structure (FCC, BCC, and HCP, respectively). Fig. 1 shows the schematic structure for a unit cell of FCC and BCC structures.

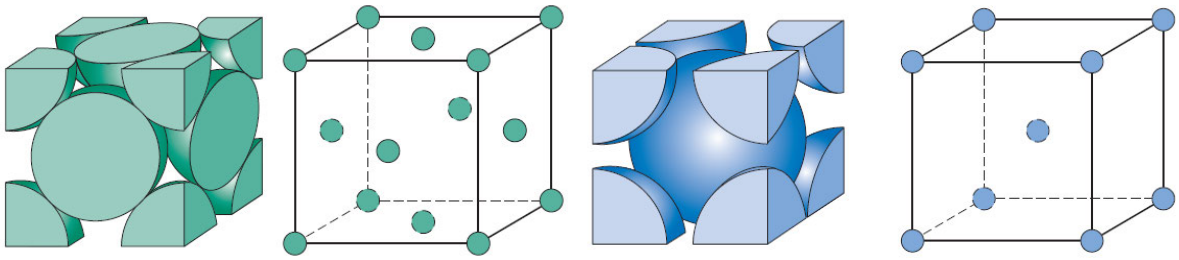

Fig. 1: a) FCC, b) BCC unit cells show the arrangement of atoms in a unit cell [9]

On all atomic crystallographic planes and in all crystallographic directions, dislocations do not move with the same ease. Typically, a preferred plane exists, and within that plane, dislocation motion happens in a certain direction. Given that this plane is known as the slip plane and the movement's direction as the slip direction, The slip system refers to this union of the slip plane and slip direction [9].

Slip happens on {111} planes (close-packed planes) along <110> directions (close packed directions) in FCC construction materials. There are 4 octahedral planes: (111), (1-11), (11-1), and (-111), each with 6 directions (110). There are 12 slip systems altogether because each direction shares two octahedral planes. Slip on (101) along <10-1> is also conceivable. In general, there are twelve independent slip systems [10].

Slip in BCC occurs on 12 possible {110} planes (close packed planes) and in slip directions of [1-11], [-111], [-11-1], and [1-11] (close packed directions), 24 possible {112} planes with slip directions of [-1-11] and [11-1] and 48 {123} planes with possible slip directions of [-1-11] and [11-1] [10].

1.3 Plasticity and dislocation theory:

Although there are many techniques now available for the direct observation of dislocations, the existence of dislocation was proved (1934 to the early 1950s) long before its first-hand observation. The discovery explained that plastic deformation occurs by atomic planes sliding over each other with the help line defect called dislocation. The concept was suggested due to the huge difference in comparison between experimental observation and the number given by calculations. Calculation of shear stress was done in a perfect crystal without presence of dislocations. In the concept of plastic deformation without dislocation, a simultaneous breaking of bonding and creating new bonding in atoms happens that makes the sliding of one plane to another possible. The shear stress required for making that process happening is:

Equation 1-1 $$\tau_{th} = \frac{b}{a}\frac{G}{2\pi}$$

where τ is the applied shear stress, G is the shear modulus, b the spacing between atoms in the direction of the shear stress, α the spacing of the rows of atoms. Using more approximation gives τ_{th} ≈G/30 which is much higher in magnitude in comparison with experimental observations. Orowan, Polanyi and Taylor in 1934 have expressed the dislocation theory [11]. They believed that dislocation could explain deformation mechanism and experimental strength. Fundamental aspects of the concept which was proposed for existence of dislocation includes (a) crystals contain dislocations; (b) dislocation is pushed forward on a slip plane as a result of applied shear stress; (c) plastic deformation is a result of dislocation movement [12].

By means of that theory, work hardening could be interpreted as when crystals yield, dislocations move through them. Moving dislocation on different planes entangle each other and prevent other dislocation to pass through. The model proposed by Taylor establishes a relation between flow stress and dislocation density. In another word, stress increase caused by interaction of mobile dislocations passing through the material.

Equation 1-2 $\tau = \alpha G b \sqrt{\rho_{\mathrm{Total}}}$

α is a dimensionless parameter, τ_0 is the flow stress of the material in the absence of dislocation interactions, G is shear modulus, b is burger's vector and $1/\sqrt{\rho_{\mathrm{Total}}}$ is the average spacing between randomly distributed dislocations.

The foundation of the Taylor equation is based on interactions between dislocations which controls the flow stress of materials. The validation of the model has been examined for polycrystal and single crystal metals and its application to FCC, BCC and HCP structures has been approved [13].

The evolution of the dislocation density depends on both the dislocation nucleation and annihilation rates. As plastic flow proceeds, the dislocation density rises and the number of active sources increases [13].

Strength and ductility are the two main terms used to describe mechanical characteristics. However, the term toughness refers to the combination of the two terms that offers a material higher mechanical property. There have been many attempts to increase those terms, but it is already widely recognized that doing so will result in a decrease in the other. It is common knowledge that internal flaws and boundaries that prevent dislocation motion can be created under controlled conditions to generate metals with higher strengths. However, such techniques typically cause a reduction in ductility or brittleness.

There are two main deformation mechanisms which metallic materials undergo: Dislocation glide and Twinning. In mechanical twinning, all the atoms in the crystal, or some sub-volume of it, can move simultaneously to accomplish the shear. Dislocation glide takes place when planes of atoms slip over one another, leading to an overall shear that is localized within specific atom planes [14][15].

Since the very first theories on dislocation and work hardening, it has been believed that plasticity can be explained by means of continuum mechanics in terms of yield stresses which leads to hardness value H = C.Y where Y is yield stress and C is a constant approximately equal to 3 [16]. Though through works of researchers, discrepancies have been found which between in practice for hardness and yield ratio.

A strong size-dependence, observed in many thin-film experiments, further complicated the construction of a work hardening theory. It has been supported by several research that revealed that single crystalline or polycrystalline materials at the micro or nano scale often support stresses that they could not possibly support in bulk form.

1.4 Dislocation generation and mobility:

Growing crystals containing low number of dislocations is difficult since dislocations are easily introduced into microstructure. Freshly formed crystals have two main dislocation sources. First, crystals grains or other surfaces used to start crystal development during solidification may have flaws. From that point onward, any crystal dislocations that contact the expanding surface extend into the growing crystal. During growth, 'accidental' nucleation may occur. The major mechanisms are (a) heterogeneous nucleation of dislocations due to impurity particles, thermal contraction, etc., (b) when growing interfaces come in to contact with each other, and (c) creation and movement of dislocation loops caused by the collapse of vacancy platelets [11].

There are 3 types of defects in crystal structure:

- Point defect i.e., vacancy, interstitial and substitutional atom;
- Linear defect i.e., Edge and Screw dislocation;
- Surface defect i.e., Stacking fault, twinned region, low-angle boundary, and grain boundary.

The reason for existence of defects is thermodynamic equilibrium.

If a sufficiently large shear stress acts on a dislocation, the dislocation moves through the crystal. Dislocation creates a particular pattern as a matter of relative position of planes in a crystal structure. Dislocation mobility means that the position of this pattern in a crystal moves as the crystal planes change their relative positions. The slip direction and the amount of slip are determined by the Burgers vector b. Movement of a dislocation is the easier to take place in the closer packed slip plane slip direction. Therefore, slip planes and directions are preferably close-packed because atoms' movement to their new position will be shorter [17]. The mobilities of dislocations are determined by interactions between the cores of the dislocations [18]. The hardness of metals, so is their strength, depends on dislocation interactions and their individual mobilities. The elastic resistance to shear plays a dominant role because it is directly involved with dislocation mobility.

Each dislocation causes distortion in the atomic arrangement around it. The distortion inserts elastic energy to the atomic bonds in shape of compression and tension fields. Figure 2 illustrates the compression and tension surrounding a dislocation.

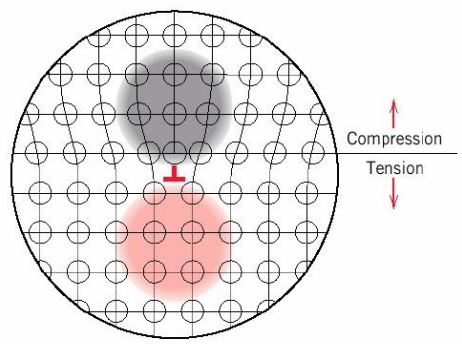

Fig. 2: Strain field around dislocation [19]

A stress-strain curve illustrates three stages of work hardening:

In Stage I, easy glide single slip system is activated and dislocation multiplication occurs; followed by stage II where high, constant hardening rate, multiple slip systems, where dislocations on multiple slip systems intersect with each other, facilitating dislocation climb and cross-slip, reducing the mean free path of dislocations, nearly independent of temperature or strain rate exist; and finally decreasing hardening rate, cross slip, and very sensitive to temperature and strain rate which are characteristics of stage III.

1.5 Tensile strength:

After yielding point, the tension required to sustain plastic deformation increases gradually till reaching highest point on the stress–strain curve called ultimate tensile strength, then necking starts to happen by which the area under stress narrows locally which concentrates stress in that area. Afterwards the stress needed to deform the test specimen drops till fracture happens. Before reaching maximum strength and necking, the deformation of the of the tensile specimen has been uniform. Necking continues till fracture occurs and the applied stress at that point called fracture strength [9].

Another important mechanical attribute is ductility. It is a measurement of the amount of plastic deformation sustained during fracture. Brittle fracture describes a material that undergoes minimal or no plastic deformation upon fracture. Figure 3 depicts the stress–strain relationships for both ductile and brittle materials under tension [9].

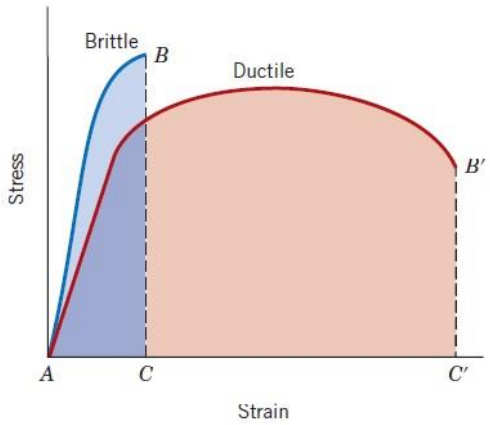

Fig. 3: Schematic representations of tensile stress–strain behaviour for brittle and ductile materials [9]

1.6 Strengthening Mechanisms:

Strength or hardness of pure metals can be enhanced by solute atoms, by cold deformation, by precipitates or hard dispersoids or by size refinement. Though these processes seem to be distinguished from one another and how they affect microstructure, however, they have one thing in common and that's their aim in restricting dislocation motion. The strengthening effect comes from the change in the amount of restriction of dislocation movement which is synonym to the length scale effect [20].

Grain size reduction decreases the space for the mobility of dislocations and therefore increases dislocation-grain boundary interaction. Grain boundaries hindering dislocation mobility and eventually cause dislocation pile-up. The repulsive interaction between piled-up dislocation leads to strength increase [9].

Alloying metal with impurity atoms which go into either substitutional or interstitial spaces between atoms of base metal, is called solid solution strengthening. Impurity atoms impose lattice strain on the surrounding atoms. This strain field interacts with dislocations and restrict their movement [9].

Strain hardening or work hardening occurs when the applied stress exceeds the elastic limit, or when the stress is greater than the yield strength. The strain-hardening is accounted for by dislocation-dislocation strain field interactions. Deformation increases the dislocation density in a metal, and as a result, the average distance between dislocations reduces. Ultimately, the existence of additional dislocations hinders the motion of other dislocations [9].

It can be comprehended from the name of each strengthening mechanism that they influence the strain field around dislocation either by adding another atom into crystal structure or particles into microstructure or even a strain field from another dislocation.

The above-mentioned mechanisms were briefly discussed, since a proposed model should take an accumulative effect of parameters affecting strength into account.

2. Literature Review:

2.1 Length Scale Size Effect:

In the range from a fraction of a micron to tens of microns, metals display a pronounced dependence on the length scale when experiencing non-uniform deformation within the plastic range. Conventional plasticity theories, lacking a material length scale and not designed to anticipate size effects, prove inadequate in describing the plastic behavior at this scale. Objects on the micron scale are too small to be effectively characterized by conventional theories, yet they are often too large for analysis using current methods based on discrete dislocation mechanics. The significant influence of a substantial number of dislocations governing plastic deformation at the micron scale necessitates the development of a continuum theory of plasticity that incorporates size-dependence. This theoretical framework aims to bridge the gap between the inadequacies of conventional theories and the challenges posed by discrete dislocation mechanics for objects at this specific length scale [21].

Different kinds of laboratory investigations such as micro-torsion, micro-bending, micro-compression, and micro-indentation hardness testing as well as simulation studies have strongly confirmed the existence of a material length scale. What these tests have in common is the ability to create non-uniform plastic deformation and when the scale is close to micron range, metallic materials exhibit considerable size effects: *"the smaller the size, the harder the material"*. Because Conventional plasticity lacks an intrinsic length scale, it cannot predict the size effects seen in studies [22].

The Size effect is the dependency of the strength of materials to the change in size, and the size can be categorized as intrinsic and extrinsic. Intrinsic size effects refer to the dependence of material strength on intrinsic microstructural properties influenced by microstructural features such as grain size, the spacing of second-phase particles or precipitates, and the dislocation mean free path. It was initially perceived that the ultimate strength of materials is governed only by internal characteristic, however, further experiments proved that the strength is a function of extrinsic size effects such as pillar diameter and indentation depth [23].

Size effect has been observed in torsional, compression, bending and indentation loading of a wide variety of materials.

Micro-compression is a methodology that typically uses FIB micromilling to produce compression samples within the surface of bulk materials. The technique involves testing small-scale samples of materials to examine their behavior under compression and explore deformation at small scales. The samples are integrally attached to the bulk substrate and can be compressed using a flat punch e.g. a

nanoindenter. The transition region between the sample and substrate effectively acts as the lower plate [24].

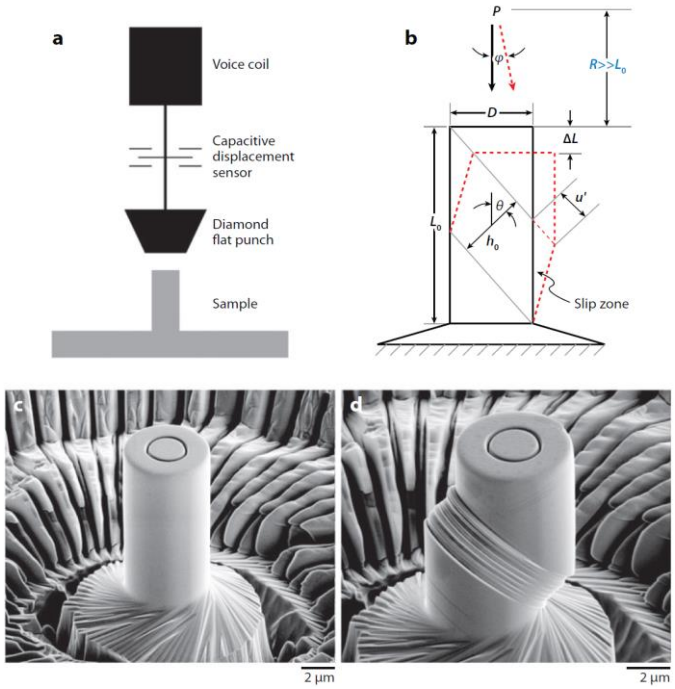

Fig. 4: a & b) Schematic of the micro-compression test that illustrated usage of a commercially available nanoindentation system (coloured in black) to apply force on the micro pillar (coloured in grey), c & d) Scanning electron microscope (SEM) image of a 5-µm-diameter microcrystal sample of pure Ni [25]

Schneider et al [26] have observed size effect in pillar compression through study of Nb and Mo single crystal pillar. The conclusion suggests the increase in screw dislocation mobility and nucleation by decrease in diameter. Other study on Mo pillars [27] has shown size effect and they found similarity in stress-strain curve of Mo and Ni and based on those findings deduced that the underlying dislocation mechanisms at small size scales are also similar. Micro compression testing of Ta pillar [28] showed not only the size effect in stress-strain curves, but also the effect of crystallographic orientation on flow stress. The micro-compression testing studies of multiple-slip oriented pure nickel microcrystals report that 200 nm diameter can support stresses of 2 GPa and higher, in contrast to bulk yield stress values for single-crystal nickel that normally range from 10 MPa and higher [29] [25]. The figure 5 is an example of the effect diameter on flow stress which was observed in Tantalum compression testing.

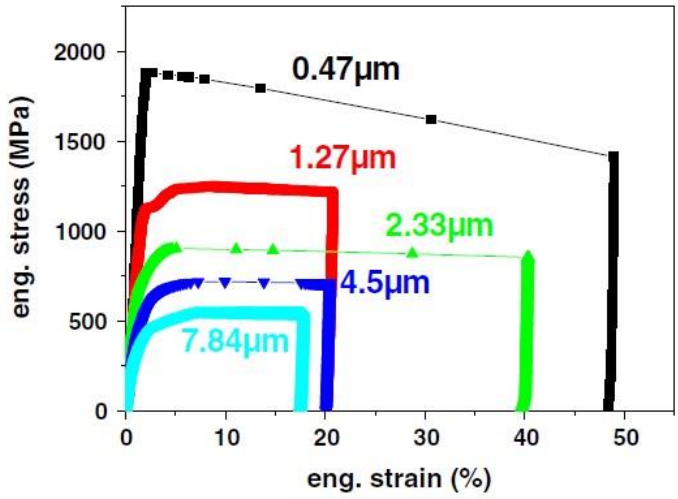

Fig. 5: Obtained stress–strain curves from micropillar compression testing for Tantalum oriented in <111> direction. The numbers next to the curves indicate the diameters of the pillars [28].

A comparative study between pillar compression testing of FCC and BCC materials has been done [30]. Though size effect has been obviously seen in both materials, however, they found that size effect is more pronounced in FCC crystal because of fundamental difference in mobility of edge and screw dislocation in FCC and BCC crystals which distinguishes size effect mechanisms in FCC and BCC.

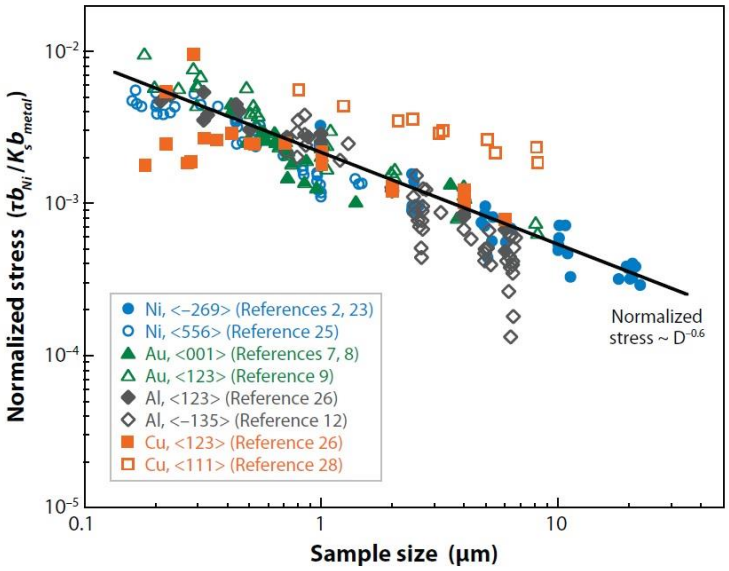

Fig. 6: Micro-compression testing composite plot of published microcrystal flow stress data as a function of sample diameter for FCC metals [25]

Micro torsion testing is a method used to study the mechanical properties of small wires. In this method, a small wire is twisted to measure its strength and deformation behaviour.

Torsion of wires from 12 to 170µm in diameter has shown that increased torsional hardening increases as the diameter of the specimens decreases [4]. Torsional testing of 20-50µm polycrystalline copper has shown size effect while that effect was not observed in tensile testing [31].

Size effect has been observed in bending testing where there is increased material hardening in bending as the thickness of the beams decreases. A classic experiment conducted by Stölken and Evans [32] demonstrated that thin nickel foils under bending display increased strengthening at large plastic strain values and, correspondingly, large plastic strain gradients. The experimental setup involves wrapping a foil of known thickness around a mandrel with a known curvature, resulting in the introduction of surface strain. Subsequently, the foil is unloaded, and the change in curvature upon unloading is measured. This measurement enables the determination of both the normalized bending moment (stress) and the extent of plasticity in the material [33]. Using the same technique for small strains and generating stress–strain curves of thin nickel foils has shown that the yield strength is greater in the thinner foils [29]. Discrete dislocation plasticity analysis shows that a strong source density dependence of the size effect that cannot be explained by geometrically necessary dislocation (GND) arguments. Source limited strengthening especially lower contribution of Frank-Read source at smaller scales is a decisive strengthening parameter. The importance of strength of a source and its exact position should not be neglected since they can dictate the plastic response of the material [34].

In the early works in micro indentation using Vickers, there was no explanation for size effect and experimental error and uncertainty assumed to be responsible. However, further analysis proved that the size effect was not primarily due to imprecision of the measurements [35]. Before invention of Nanoindentation, a pioneering works of Gane [36][37] in 1970 clearly shows the existence of size effect. A sharp conical indenter was used inside a scanning electron microscopy to indent electropolished and annealed single crystal of gold. Gold was used to avoid the effect surface oxidation. He noticed that below certain load point, the hardness fell rapidly with increasing penetration and for the same amount of strain, the measured hardness is more than macroscopic hardness of gold single crystal.

Invention of Instrument Nanoindentation testing technique, created the possibility to control and measure load and displacement carefully so that an indentation probe penetrates the material and the force applied to the probe and its penetration into the surface are measured. The ratio of the measured parameters gives the hardness for the given load or the given penetration depth [38]. The early indentation study of Ma and Clarke [39] in micron and nano range of indentation depth on silver revealed the existence of size effect in single crystal.

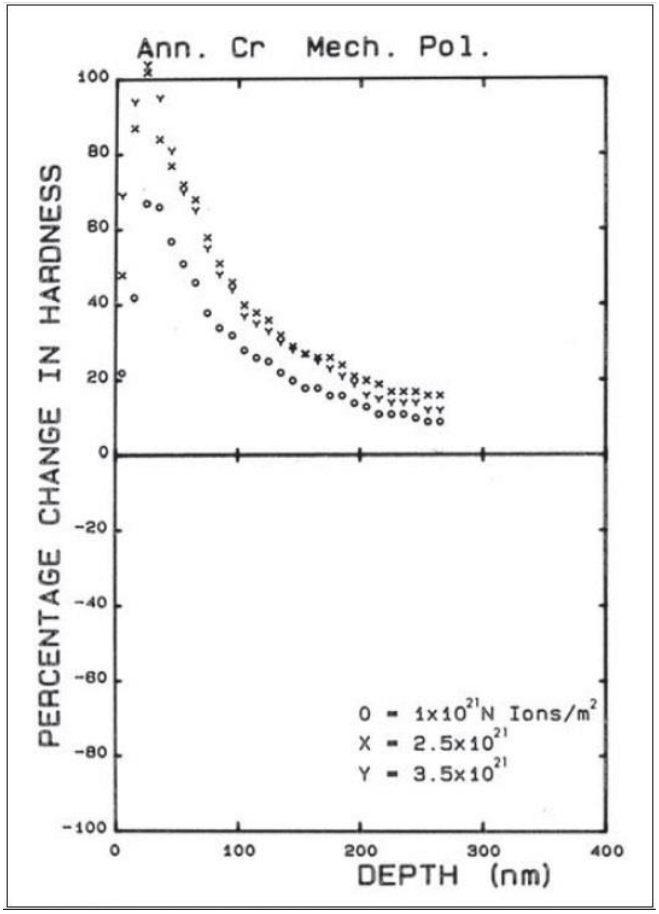

Fig. 7: The diagram depicts findings from an early investigation conducted by Oliver and Pharr using the original nanoindenter. The change in hardness as a function of indenter penetration depth was examined for a sample of annealed chromium that had been implanted with nitrogen. Indentation testing was performed using a Berkovich indenter [38].

Figure 8 shows a collective test results of micro and nanoindentation which indicates size effect observed by various researchers performed on different metallic materials [40]. Size effect has been observed in both FCC and BCC materials.

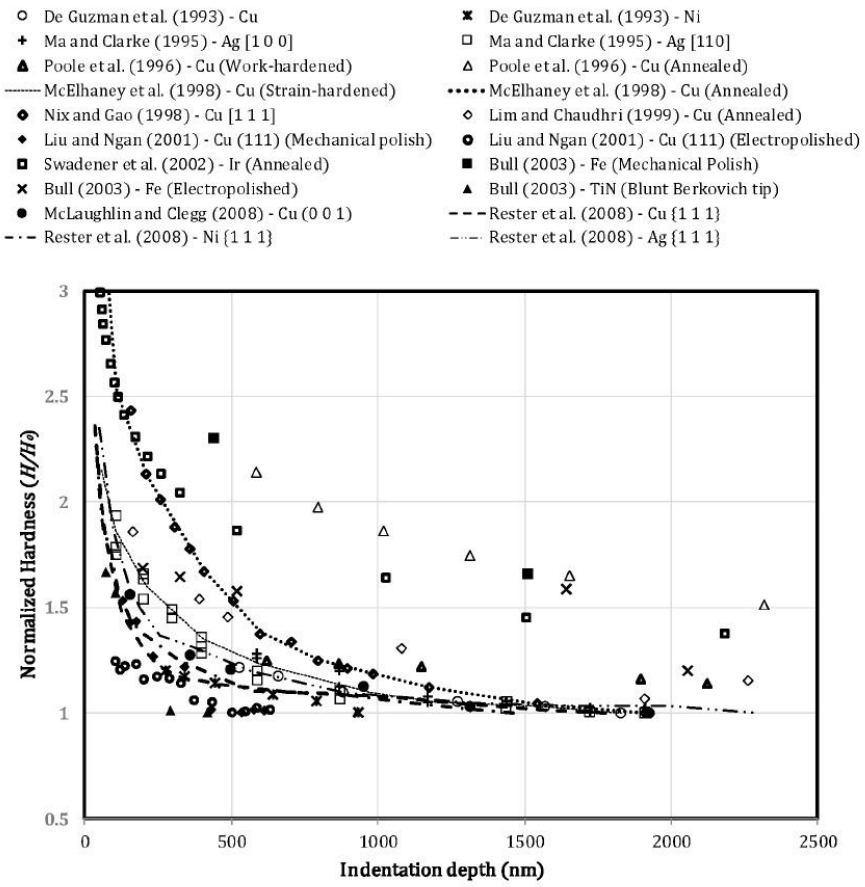

Fig. 8: Size effect during nanoindentation obtained from various experimental studies of FCC and BCC structured materials [40].

3-D and 2-D EBSD analysis of indentation testing performed on copper at various depth [41] has shown the inhomogeneous arrangement of the GNDs beneath the indent and reveals that the GND density in smaller depths is not the only factor to increase the hardness but decrease in dislocation segment length due to increase in dislocation density might account for hardness increase.

Three-dimensional Dislocation Dynamics (DDD) simulations were conducted on Cu single crystals subjected to indentation using both spherical and conical indenters [42]. In these simulations, the initially dislocation-free crystal was modified to include a distribution of Frank-Read (FR) sources beneath the indented surface to replicate the nucleation of dislocations in the region beneath the indenter. For the case of the spherical indenter, the observed trend of the hardness curve closely aligned with findings from previous spherical indentation experiments. However, the hardness values extracted from the DDD simulations were notably lower than the predictions of the Nix and Gao model. An interesting revelation from the simulations was the highly heterogeneous nature of the dislocation density. Additionally, it was discovered that the volume occupied by the dislocation structure beneath the indenter was larger than previously assumed. The influence of varying densities of dislocation sources on plastic behaviour has been examined [43] for characterizing nanoindentation

through discrete dislocations. An identical number of dislocations are randomly distributed across two distinct ranges. The investigation spans the dislocation behaviour from the initial stage of indentation to the maximum indentation depth and extends to the unloading phase. It is observed that the continuum value is attained at a smaller indentation depth when there is a higher density of dislocation sources. Furthermore, the simulation reveals the occurrence of an indentation size effect in the early stages of the process, where the discrete nature of plasticity is predominant. This emphasizes the importance of considering the discrete behaviour of dislocations in the early phases of simulated indentations before transitioning into the continuum plasticity regime.

Molecular dynamic (MD) Investigation of dislocation nucleation and evolution pattern during nanoindentation [44] could visualize loop formation and movement of partial dislocations and perfect dislocations along three directions of [-1 0 -1], [-1 -1 0] and [0 -1 -1]. Dislocation prismatic loops moving toward bottom of the sample should be considered as a measure of plastic zone size because plastic zone volume size becomes unreasonably large. Plastic zone size is determined based on the furthest dislocation attached to the main body of dislocation beneath the indenter. Boundary conditions may alter the plasticity initiation and defect nucleation pattern depending on the film thickness and indenter radius nanoindentation response of FCC crystalline metals [45]. Large scale MD simulation of Ni thin films [46] concludes that Similar to the compression and tension experiments on micropillars, forest hardening mechanism does not govern size effects and the source exhaustion hardening is the governing mechanism of size effects at shallow indentation depths. As the indentation depth is increased, there is a simultaneous increase in both dislocation length and density. This augmented dislocation length and density contribute to an increased availability of dislocation sources within the material. Additionally, the lengths of these dislocation sources also increase, leading to a reduction in the critical resolved shear stress. The influence of grain boundaries [47] on the dominant hardening mechanism is contingent upon the grain size. Specifically, the effect can result in either an increase or a decrease in indentation hardness, dependent on the grain size. In metallic samples with very fine grains, grain boundaries contribute to dislocation nucleation. This process generates more dislocations at shallow depths, leading to a decrease in indentation hardness. This effect aligns with the source exhaustion mechanism. Conversely, in the case of larger grain sizes, grain boundaries act as barriers impeding the movement of dislocations. This hindrance enhances hardness through the forest hardening mechanism. Therefore, the impact of grain boundaries on the governing hardening mechanism is intricate, with the grain size determining whether the contribution is towards decreasing or increasing indentation hardness.

Studies have been done to find out a relation between ISE and SFE. They do not reject the role of SFE in ISE, however, proposed that this contribution is relatively small relative to that of existing dislocation structures [48].

J.C. Huang et al [49] have studied the micro and nano compression on Aluminium single crystal and observed size effect. Their comparison with the other works done on Ag, Au, Cu and Ni, they could relate stacking fault energy to size effect and concluded that the material with higher stacking fault energy show lower size dependency due to higher dislocation mobility.

Stegall et al. [50] studied pure metals and alloys to find out if there is a relationship between indentation size effect (using Berkovich tip) and stacking fault energy. Activation volume V* for each metal with respect to the hardness normalized to the shear modulus appears to follow a trend based on SFE. This trend was observed for pure metals and not a similar trend was observed for alloys.

2.2 Different Plasticity Mechanisms at different Length Scales:

Observation of the size effect in various micromechanical testing techniques has risen attention to find a connection between experimental results and microstructural evolution. Nowadays, a wider range of length scales can be tested on specimens and various models propose concepts which can consist of materials behaviour in macro, micro and nano length scales.

Jorge Alcalá et al. [51] through molecular dynamic simulations have demonstrated that the current notion of nanocontact plasticity in FCC metals does not apply to BCC metals. They have found that plasticity is governed by dislocation nucleation followed by twin growth, twin annihilation, and dislocation emission.

Indentation of Nickel single crystal using Berkovich indenter [52] in the range of 100nm to 3µm in conjunction with a TEM technique called precession electron diffraction (PED-TEM) to overcome difficulties of EBSD and conventional TEM has been performed to give an insight into microstructural development in various sub-micron length scales. They have reached the conclusion that for depth below 100nm, dislocation source activation is dominating mechanism for ISE. In 100nm to 400nm, dislocation starvation and dislocation interaction are accountable effect and beyond that dislocation interaction hardening holds for indentation size effect.

Caizhi Zhou et al. [53] employed dislocation starvation and single arm dislocation models for simulation of plasticity of micropillars of FCC metals in nano- and microscales. They have shown that by increasing size, multiplication of dislocations and with decreasing size, dislocation starvation are dominant plastic deformation mechanisms. They have divided the effect of size on change in plasticity

mechanisms in three different zone which zine 1 is up to 0.5µm, zone 2 between 0.5µm and 1µm and zone 3 for above 1µm.

Lihua Wang et al. [54] through TEM investigation and review of other works performed in this field have come up with size dependant dislocation mechanisms as an explanation for different mechanisms governing plasticity of metals at different length scales. For sizes 200nm and above, Plasticity is carried out by slip of full dislocation. Below 100nm, the plasticity mechanism changes from normal full dislocation slip to partial dislocation plasticity which creates stacking faults. Further reducing the size to approximately 6nm, the in situ atomic-scale observation demonstrates that lattice slips become the dominant.

Javier Varillas et al. [55] have studied the deformation mechanisms at different scales in FCC, BCC and HCP metals from the onset of plasticity using molecular dynamic simulations and have concluded that in different indentation depths, different mechanisms prevail. For FCC samples, the plasticity begins with Emission of leading Shockley partial dislocation loops followed by twinning and dislocation loops. In BCC samples, early twin nucleation, twin growth, twin interlocking and eventually Emission of a dislocation loop through twin annihilation. They observed pop-in in the early stage as a sign for dislocation nucleation in both FCC and BCC.

Oliver Kraft et al. [56] have defined three regimes in which different mechanisms govern which led to size effect observation. They concluded that the transition occurs from the nucleation of individual partial dislocations to the nucleation of individual full dislocations, along with the subsequent interaction and multiplication of these dislocations.

Reiner Moenig et al. [28] have investigated pillar size effect and orientation effect of Tantalum single crystals by compression testing of pillars with different sizes. They observed size effect, however, while comparing their results with the results of other literature, they concluded that BCC shows a weaker size effect than FCC does. This is in contradiction with the results in our study. The reason might be due to the profound difference in testing methods. Since dislocation annihilation or dislocation starvation are the mechanisms which have been mentioned to play a significant role in small sizes in pillar compression testing, however, it does not seem to play a role in indentation testing due to the existence of enough bulk material in the direction of indentation which prevents exit of dislocation(s) from the surface.

Micro pillar compression of nickel single crystal with various diameters have shown a strong size effect. Reducing pillar size has shown a simultaneous increase in both strength and ductility. That research justifies the change in plasticity mechanisms at different length scales and finalized that size-

affected changes in dislocation mechanisms may be more important than gradient-induced storage of geometrically necessary dislocations [57].

Nanoscale pillar compression testing of FCC and BBC structure materials [30] has revealed different responses which have been related to different plasticity mechanisms in terms of dislocation nucleation and motion. Plasticity in Au (FCC) is likely controlled by nucleation of new dislocations rather than by interactions of the pre-existing ones. On the contrary, in Mo (BCC) plasticity is likely driven by the intricate motion and interactions of dislocations inside the pillar rather than by nucleation events.

Beam bending of Single crystalline copper beams [58] with thicknesses between 0.7 and 5 µm have brought the authors to the conclusion that one mechanism cannot be responsible for size-effect. limit is defined in terms of a microstructural correlation measure (characteristic dislocation bow-out length) below which the local availability of dislocation sources and not the density of GNDs dominates the mechanical size effect.

2.3 Strain Gradient Theory:

The strain gradient plasticity theory was proposed by Nix and Gao to explain size effect and its aim was to find a relationship between the square of the indentation hardness and the inverse of the indentation depth (Equation 2-1). The approach to formulate the theory in a way that can predict the hardness, bearing in mind the existence of size effect and non-linearity of hardness at different indentation depth, is to make a connection between flow stress and dislocation density using Taylor's relation and makes use of the concept of the evolving density of the so-called ''geometrically necessary'' dislocations as a contribution factor to total density of dislocations. The model assumes that the flow stress of crystalline materials originates from the two types of the dislocation density. Based on the terminology from Ashby [59], geometrically necessary dislocation (GND) is required for the compatible deformation (curvature) of the crystal lattice or to strain gradients, and random accumulation of statistically stored dislocation (SSD) that is created by homogeneous strain. The smaller the indentation depth, the more contribution from GNDs which results in enhanced hardening effect [3][7]. This model assumes that the indentation is accommodated by circular loops of GNDs with Burgers vectors normal to the plane surface [60].

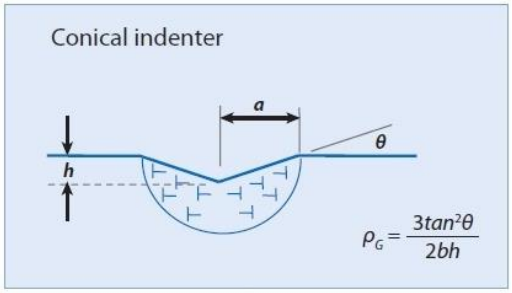

Fig. 9: The Nix-Gao model for conical indenters. The geometrically necessary dislocations (GNDs) are assumed to be localized in a hemispherical region beneath the indenter.

Equation 2-1 $$H = H_0\sqrt{1+\frac{h^*}{h}}$$

Equation 2-2 $$H_0 = 3\sqrt{3}\alpha G b\sqrt{\rho_s}$$

Equation 2-3 $$h^* = \frac{3\bar{r}\tan^2\theta}{2b\rho_s}$$

H_0 represents macroscopic hardness, h^* characteristic depth and H is the hardness for a given depth of indentation, h.

Strain gradient theory model breaks down at small depths of penetration [57][61][52]. Not only the prediction of hardness in low depth indentation is incorrect, but also prediction of size of plastic zone and dislocation density deviates from direct observation [52]. Also, size effect has been reported in compression testing of pillars in which mechanism to explain the size effect is not relied on geometry necessary dislocations contribution [53][25][62][63].

2.4 Hall-Petch effect and Slip distance theory:

Hall–Petch equation was proposed in 50s, represented as an equation that can estimate the magnitude of strengthening increase through refining of metals grain size. The empirical equation has been developed to describe strengthening of polycrystalline materials by grain size refinement. This can be explained by a model invoking a pile-up of dislocations against grain boundaries as depicted in figure 10. Since then, numerus researches have been done to prove validity of the proposed theory and support its applicability [64].

Equation 2-4 $$\sigma(\varepsilon) = \sigma_0(\varepsilon) + \left(\frac{K(\varepsilon)}{\sqrt{d}}\right)$$

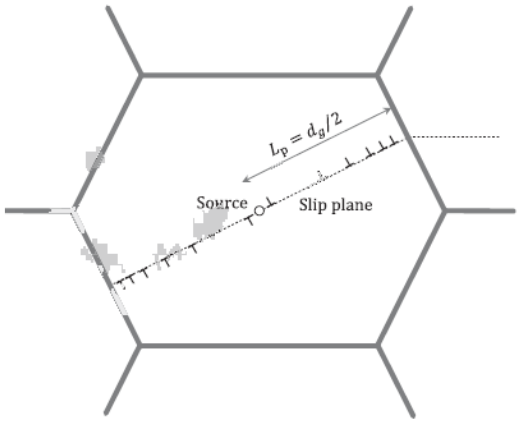

Fig. 10: Dislocation pile-up model to capture Hall-Petch effect [23]

It has been observed Hall-Petch effect cannot correctly predict the yield strength for polycrystalline samples with grain size smaller than some specific limit. Two trends have been observed when the grain sizes reach the limit and smaller grain sizes. Flow stress becomes a constant value in grain sizes below the limit or decreases as the grain size decreases, which is commonly known as the inverse Hall-Petch effect [23]. This effect is opposite to the traditional Hall-Petch effect, where the yield strength increases as the grain size decreases. The inverse Hall-Petch effect is attributed to grain boundary sliding, which is the movement of grains along the boundaries between them.

Another case is the effect of dislocation boundaries and high angle boundaries in deformed metals which requires modification in that equation [65]. As well as, a large body of evidence that questions the validity of that equation in nanocrystalline materials [66]. A thorough investigation of the experimental evidence have been done which indicates many other functions fit well to the data in micromechanics which seems valid owing to the general relationship to describe the inverse relationship between the stress required and the space available for dislocation sources to operate [67].

In a study of size effect, single crystal of copper and poly crystals of copper with various grain sizes were indented using Berkovich and spherical indenters. The data were analysed using a model generated based on Conrad's slip distance theory. The result demonstrated an interaction between size of indentation impression and grain size. When the grain size, d, is less than 6 times the radius of the projected contact area, α, a Hall–Petch-like behaviour is observed [68]. This might be an insight into the coupling effect of plastic zone size and grain size in hardness measurement.

The issues motivated the development of an alternative class of work-hardening models using the assumption of the influence of the dislocation density, ρ, which in turn affects the flow stress through the Taylor equation:

Equation 2-5 $$\sigma = \sigma_0 + \alpha G b \sqrt{\rho}$$

where G, b, and α are the shear modulus, magnitude of Burger's vector and empirical coefficient (crystal type dependant) respectively.

Conrad considered plastic flow as the movement of mobile dislocations which transfers plastic strain through a crystal dependent on the mean free path of dislocations. He introduced this ''slip-distance'' theory to explain the Hall-Petch effect [69]. The plastic strain obtained after the motion of dislocations depends on the density of dislocations (number of dislocation), their Burgers vector, and the distance these dislocations move [70]. The slip distance model describes the form of the size effect based on the geometry of the contact stress field to give an inverse dependence on the square root of contact size [71].

Plastic strain ε_{pl} is accommodated by the density of mobile dislocations. Summation of mobile and sessile dislocation is the total number of dislocations is the structure of the material. Therefore, mobile dislocation is considered to be some fraction of the total dislocation density, $\rho_m = \lambda\rho_{total}$. Having $\bar{x}$ as mean free path for the movement of mobile dislocations, plastic strain can be written as:

Equation 2-6 $$\varepsilon_{pl} = b\bar{x}\rho_m$$

where b is the effective Burger's vector, ρ_m is the density of mobile dislocation and ρ_s is the density of sessile dislocation.

Equation 2-7 $$\rho_{total} = \rho_m + \rho_s$$

Equation 2-8 $$\rho_m = \lambda\rho_{total}$$

Equation 2-9 $$\Delta\sigma = \alpha G b\sqrt{\rho_{total}}$$

Equation 2-10 $$\Delta\sigma = \alpha G b\sqrt{\rho_t}$$

Equation 2-11 $$\Delta\sigma = G b\sqrt{\rho_s}$$

Equation 2-12 $$\Delta\sigma = G b\sqrt{(\frac{1-\lambda}{\lambda})\rho_m}$$

Equation 2-13 $$\Delta\sigma = G b\sqrt{(\frac{1-\lambda}{\lambda})\frac{\varepsilon_{pl}}{b\bar{x}}}$$

where G is the shear modulus; α is the Taylor coefficient.

The indentation generates plastic strain in the material which is accommodated by generating dislocations and moving them an average slip distance, which is the reciprocal of the average frequency of obstacles to dislocation motion in the indentation plastic zone.

Equation 2-14 $$\varepsilon_{pl} = b\bar{x}\rho_m$$

Considering the analogy that total number of dislocations is sum of the mobile and sessile dislocation.

Equation 2-15 $$\rho_{total} = \rho_m + \rho_s$$

λ indicates the fraction of mobile dislocations to total dislocations in the plastic zone caused by indentation.

Equation 2-16 $$\rho_m = \lambda\rho_{total} \text{ or } \lambda = (\frac{\rho_m}{\rho_t})$$

The stress balance at the end of indentation is given by the equation [1][72]:

Equation 2-17 $$\left(P_m - P_y\right)^2 = \frac{K_1}{a} + \frac{K_2}{d} + K_3\sqrt{\rho_s}$$

Equation 2-18 $$K_i = k_i G^2 b\varepsilon_p \left[\frac{1-\lambda}{\lambda}\right]$$

Where: P_m is the mean indentation pressure, P_y is the yield pressure of a single crystal half-space, a is the equivalent contact radius of the indentation, d is the grain size and ρ_s is the line density of pinning dislocations, G is the shear modulus, b is the burgers vector, $(1-\lambda)/\lambda$ is the ratio of static to mobile dislocation density, ε_p is the total plastic strain generated, and the parameters k_i (i = 1 to 3) are used to scale the dimension that can be identified and measured (e.g. indent size or grain size) to the actual length scale relevant to a dislocation (e.g. size of plastic zone or active slip plane).

Indentation size effect depends on the inverse square root of the contact dimension. Therefore, there is a need to find a dimension (radius) which can be used for comparison of various type of indenters. Contact radius of the indentation ''a'' is calculated using $\sqrt{\frac{A_c}{\pi}}$ where A_c is the indented/contact area measured using AFM. As shown below, it is the equivalent to radius of a circle which has the same area as contact area A_c [72].

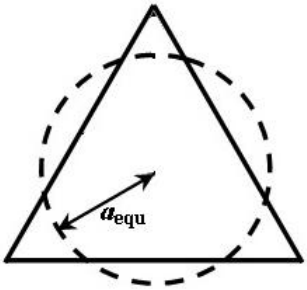

Fig. 11: Schematic view of a created contact area using Berkovich indenter and the equivalent circular area with radius of a [72]

A worked example: Nanoindentation delivers Ac = 266.99µm^2 as the area of indentation impression at 70mN applied force. However, the effect of pile-up and sink-in does not count in the measured value through nanoindentation. Indented surface was scanned using AFM and the scanned file was imported Gwyddion software for drift correction. Drift corrected image was imported to custom-made MatLab code which delivered the area of indentation impression to be 307.0385µm^2 (corrected Ac). Optical and SEM observations of the indented surfaces confirmed the existence of pile-up in all edges and as a result an increase in the area of indentation is seen. ''a'' is calculated to be $\sqrt{\frac{307.0385}{\pi}} = 9.8860\mu m$.

Indentation hardness P_m is the corrected hardness after measured hardness has been divided by AFM measured contact area. The yield pressure of a single crystals P_y have been collected from literatures, though its value in comparison to P_m is insignificant.

K_1/a, K_2/d and $K_3\sqrt{\rho_s}$ could be calculated which could be interpreted as the size of the plastic zone, Grain size effect and spacing of pinning dislocations respectively. The flow stress (mean pressure of indentation) required to move dislocations also depends on the curvature (and so size) of the dislocation source/loop being activated, whose average size is given by the average spacing of the obstacles. The inverse of area of indentation ''1/a'' is used against hardness square $(P_m - P_y)^2$ in order to draw a graph to find out the constants of the equation 2-16.

2.5 Dislocation density:

Plastic properties of metals particularly their yield stress, hardness, strain hardening coefficient and toughness, work hardening, and ductility are intrinsically linked to the content and type of microstructural defects, particularly dislocation density. Understanding the influence of these defects is essential to understanding the materials' mechanical response under different loading conditions. Strain hardening happened during plastic deformation through increase in dislocation density, dislocation movement and dislocation interaction. It is obvious that dislocations have the major

influence on the mechanical plastic response. However, determining dislocation density in metals has been a challenge for decades in materials science. Its importance has encouraged to put efforts into development of miscellaneous methods [73].

The Frank-Read (FR) source is a type of intragranular dislocation source that plays a significant role in the multiplication of dislocations in crystalline materials. The functioning of a Frank-Read source in the presence of voids that act as pinning obstacles is a complex process. Initially, a straight dislocation line is confined between two voids. Then, when subjected to a shear stress, the segment begins to bow out until it reaches the critical configuration, as depicted in Figure 12 (a-c). Both ends of the dislocation bow around the void periphery. When the applied shear stress surpasses the critical shear stress, the bowed-out dislocation continues to grow until two segments of the "kidney-shaped" structure collide, resulting in the formation of a dislocation loop. After the loop formation, a straight dislocation line is left pinned between the two voids, as shown in Figure 12 [74] [75].

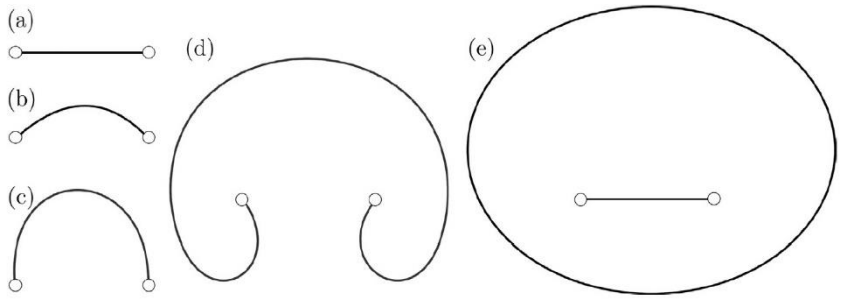

Fig. 12: Illustrations of the FR source process [75]

Geometry necessary dislocation (GND) vs Statistically stored dislocation (SSD):

The recent proposed theory cast dislocations into two categories: Geometry necessary dislocations and statistically stored dislocations. statistically stored dislocations, which are created by homogeneous strain, and geometrically necessary dislocations, which are related to the curvature of the crystal lattice or to strain gradients [59]. The movement of statistically stored dislocations (SSD) carries the strain applied to the material while Geometry necessary dislocations (GND) align in a way to cope with the change in the surface which cannot stand continuous anymore. This way GNDs can help to keep lattice continuity. Random generation and movement of SSDs is responsible for homogeneous deformation. Though the role of each type in dealing with stress is different, however, both contribute to the flow stress [76].

The contribution of geometrically necessary dislocations to strain gradient becomes more significant as the scale of deformation gets smaller since increasing the deformation, hence indentation depth, more volume is involved which increases the role of statistically stored dislocation [39]. These

geometrically necessary dislocations do not contribute to plastic strain, but they act as obstacles to the motion of other ‘‘statistically stored’’ dislocations and hence contribute to the work hardening of the material [22].

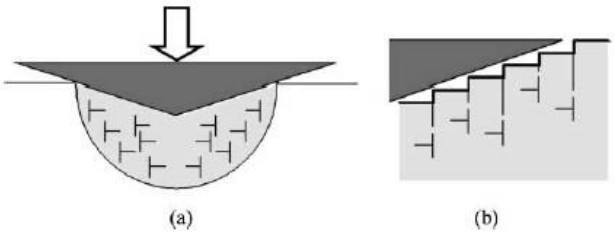

Fig. 13: Geometry necessary dislocation underneath an indenter [76]

Therefore, the combined effect of both types should be considered to estimate the deformation resistance and Taylor equation can be written as:

Equation 2-19 $$\sigma = \alpha G b \sqrt{\rho_S + \rho_G}$$

Dislocation density ρ is composed of the densities ρ_S for statistically stored dislocations (SSD) and ρ_G for geometrically necessary dislocations (GND).

A comprehensive understanding of work hardening process demands a better understanding of dislocation’s core structure and its mobility. Stacking fault energy is the main influential parameter on those factors. Based on dislocation density definition which the number of dislocations per cubic meter in the deformed zone, it is imaginable that different materials regarding having different properties such as SFE, slip systems, crystallographic structure etc. will have different plastic zone size and different number of dislocation and therefore, different dislocation densities. As a result, it will help to have a quantitative based perception of work hardening in different materials.

2.6 Indentation:

The technique was presented in 1992 for assessing hardness and elastic modulus through nanoindentation testing has garnered widespread adoption and application in the examination of mechanical properties at small scales. Since its initial inception, this approach has experienced numerous enhancements and modifications stemming from advancements in testing apparatus and methodologies, alongside progress in comprehending the mechanics of elastic-plastic interactions. [38].

Uniaxial testing is a well-known method for generating generic mechanical properties of materials. However, it cannot characterize plasticity deformation adequately because it is limited to local

volumes. The stress-strain curve which is aim of the tensile testing is an embody of the average value in terms of mechanical properties. The need to study the individual factors separately which deliver an average value for strength of materials has been the motivation to seek other testing methods and techniques. Instrumented indentation testing (IIT) has been employed as a tool to evaluate mechanical properties in smaller scale and more precise ways. Using IIT, different amount of strain, different shape of deformation into variety of materials can be applied which gives numerous opportunities to study materials' properties and looking further into microstructure-properties relationship. It has attracted attention for its capability to reveal and investigate size effect.

Variation of hardness in different length scales is not foreseen in conventional plasticity theory. In plasticity theory all material properties are length scale independent, the measured hardness values should be independent of the indentation size. However, there is a set of experimental data in the literatures showing alteration of the measured hardness when the size of the indentation is in the range of 0.1 to 10 μm. Unwanted features on the surface such as oxidation and roughness and insufficient instrument measurement ability had mentioned as the early justification for those experimental observations [39]. However, usage of new techniques like atomic force microscopy and scanning electron microscopy and electron backscatter diffraction along with Indentation testing affirm the existence of ISE. AFM can give a direct measurement of the indentation impression which can correct the measured hardness value as well as by using AFM one can measure the indenter surface to have a more reliable indenter area function. EBSD scans have been used to measure geometry necessary dislocations and their evolution.

Nanoindentation as an instrumented indentation method opened a new way for investigation of small-scale materials and found its application widely to determine the mechanical properties of bulk materials and thin films. The superiority of this technique is precise indent location, high-resolution load control and displacement measurement. The load–depth curves including loading and unloading process can be obtained by nanoindentation technology. Figure 14 shows a schematic loading-unloading curve for Nano indentation experimentation which includes loading, creep, unloading, holding and final unloading steps.

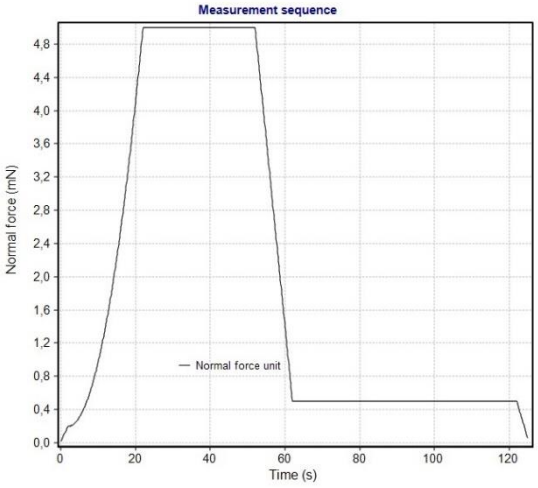

Fig. 14: Schematic process of a single cycle nano indentation test including loading curve, holding period, unloading curve, holding at 10% maximum force for sixty seconds for drift correction and final unloading.

It is known that the equations $S = 2aE_r$ and $H = {}^{F}/_{A}$ are the founding equations for nanoindentation testing and deliver the hardness and elastic modulus.

Instrumented indentation test consists of piercing a test piece by loading a diamond indenter in the direction parallel to the normal of the surface of the sample. There are two possibilities in terms of controlling the process of indentation. Indentation testing can be done either displacement controlled, or force controlled. Force control is the most common practice. As shown in Fig. 15, force increases from zero to a maximum value over a specified time interval, then it is held at constant value for a certain period, to compensate for creep, and load is gradually removed over a specified time, down to zero. The loading curve is typically modelled according to Kick's law, where the relationship is expressed as P = Ch^2. In this equation, 'P' represents the applied load, 'C' depends on various factors including the elastic and plastic properties of the material and the geometry of the indenter, and 'h' stands for the indentation depth. When the maximum depth of indentation is reached, denoted as 'h_m', or the maximum load applied is 'P_m', the average contact pressure, 'P_{ave}', can be calculated as the ratio of the maximum load to the true projected contact area measured at 'h_m', referred to as 'A_m'. This average contact pressure, 'P_{ave}', can be considered as the hardness ('H') of the material being indented [77]. The force, displacement and time are constantly recorded, and the test result will be presented in a graph of force-indentation depth. The main outcomes of IIT are instrumented hardness H_{IT}, and indentation modulus E_{IT}, an indication of elastic properties of material. Stiffness is evaluated at the maximum force and in conjunction with calculated area provides a measurement of the combined elastic modulus of the system [78].

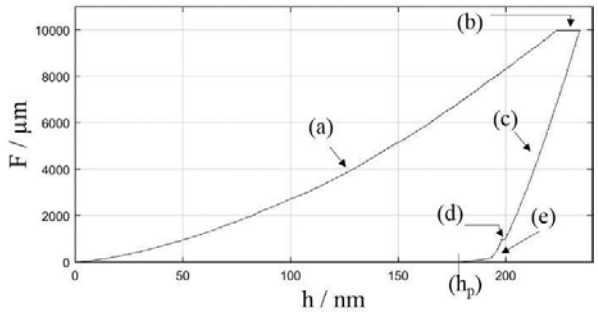

Fig. 15: Demonstration of force vs displacement curve in an indentation testing: (a) loading starts from the onset of contact of indentation with the surface and the force is gradually increased, (b) is the hold period at maximum force, (c) is the unloading curve which illustrated the elastic recovery after force removal (d) second held to compensate for drift, and (e) is the final unloading [79]

It has been studied that the measurement of stiffness by the linear extrapolation method defined by Doerner and Nix [80] and power law method introduced by Oliver and Pharr, both present shortcomings mainly related to the disregard of actual shape of unloading indentation curve [79]. A higher attention should be paid in case metallic materials since the elastic recovery is small. Thus, any minor change is the slope of stiffness curve, may create a big difference in hardness due to change in the measured indentation depth (h_c).

2.6.1 Berkovich indentation:

The Berkovich tip is a three-sided pyramid which is the most commonly used indenter in nanoindentation experiments [81]. The modified Berkovich indenter is designed to have the same projected area as the Vickers indenter at any given indentation depth [82]. The angle between the centreline and the three faces is 65.3°. The three-face design allows to grind the tip to a sharp point. Berkovich Nano indenter is used to conduct the indentation experiments using a Berkovich indenter in Air medium in this study. For different materials different indentation force should be used in order to keep the proper distance between indents to avoid interference as well as having an almost similar range for displacement. In contrast to spherical indentation, where each indent depth corresponds to a different strain point, Berkovich indenters which is a self-similar geometry indenter, indents at a constant strain defined by the facet angle of the indenter, regardless of indentation depth (size) [72]. When the indenter is self/similar geometry, a larger indentation can be regarded as an amplified representation of a minor indentation. This implies that the strains and consequently the stresses remain consistent across geometrically analogous areas. Therefore, the indentation yield pressure (denoted as "p"), representing the average pressure applied to the indenter, remains constant regardless of the indentation's size. Consequently, for a pyramidal (or conical) indenter, the hardness remains unaltered regardless of the indentation's dimensions [83]. Upon onset of indentation contact, both plastic and elastic deformation exerts over the contact region. The contact stresses are highly

concentrated beneath the tip and decrease significantly in magnitude with distance away from the contact region [84].

Another aspect which should be considered for indenting materials using Berkovich indenter is Orientation dependence of the single crystals which have been already studied and proved to cause a difference in results [85][86].

Figure 16 depicts a cross-section of the specimen surface profile under full load. The circle of contact lies beneath the free surface of the specimen. Even for totally elastic contact, a certain amount of sink-in of the surface is expected. Throughout applying the load, $h = h_c + h_s$ hold true for total displacement being h. At peak load, the load is P_{max} and displacement called h_{max}. After reaching the maximum load and holding on that for a specific period of time, unloading starts and the elastic displacement is recovered. Unloading continues till the indenter is fully withdrawn from the test material [87].

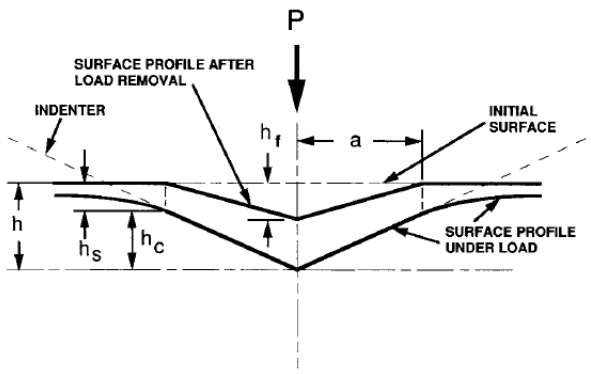

Fig. 16: A schematic representation of an indentation. Cross-section of profile of specimen surface at full load, and full unload for an elastic– plastic indentation [87]

W.C. Oliver and G.M. Pharr have established the method to extract and analyse the mechanical properties such as hardness and young's modulus of the tested materials from loading-displacement curve [87]. Since then, this method with slight improvements done by other researchers has been foundation of the instrument indentation testing technique.

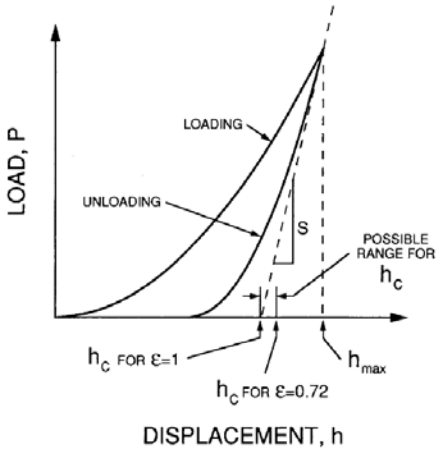

Fig. 17: A schematic representation of a loading-displacement curve [87]

Analysis of the indentation load-displacement curves was carried out using the well-known method proposed by Oliver and Pharr [88].

Equation 2-20 $$F = a(h - b)^m$$

where F is the load; h is the depth; a, b and m are fitting parameters.

The contact stiffness, S, is calculated at peak load as below:

Equation 2-21 $$S = \frac{dF}{dh} = am(h_{max} - b)^{m-1}$$

The intercept depth, hi, is given by:

Equation 2-22 $$h_i = h_{max} - \frac{F_{max}}{S}$$

The contact depth, h_c, is calculated using h_{max} and h_i:

Equation 2-23 $$h_c = h_{max} - \zeta(h_{max} - h_i)$$

where ζ is a constant depends on the geometry of the indenter. A standard value ζ = 0.75 is taken for analysis.

The contact area, A, is calculated using the appropriate area function:

Equation 2-24 $$A_c = f(h_c)$$

And the indentation modulus, E*, is:

Equation 2-25 $$E^* = \frac{\sqrt{\pi}}{2}\frac{S}{\sqrt{A_c}}$$

2.6.2 Area Function:

Nano indentation is an indirect measurement of hardness. It means that force or a range of different forces is selected by operator and since hardness is force divided by area, hardness value can be calculated. Indirectness of nano indentation comes from the latter part which is measuring the area. Area is measured indirectly using area function of the indenter. Each indenter, based on its shape, causes a certain type of deformation in the material which remains a certain type of surface area. Area function relates surface area to the distance from the tip of the indenter. A plot of the computed contact area as a function of contact depth can be described as [87]:

Equation 2-26 $$A = C_0h_c^2 + C_1h_c + C_2h_c^{1/2} + C_3h_c^{1/4} + C_4h_c^{1/8} + C_5h_c^{1/16}$$

Area function for Berkovich indenter has been theoretically calculated to be as mentioned below:

Equation 2-27 $$A = 24.5\ h_c^2$$

Area function is calculated based on h_c which is measured by equipment directly. Using the depth of indentation, the hardness can be measured.

2.6.3 The effect of Pile-up and Sink-in:

Figure 18 shows a schematic process of indentation using Berkovich and two phenomenon which take place during indentation: Pile-up and Sink-in which are characteristic of materials and are importance for finding contact area [89].

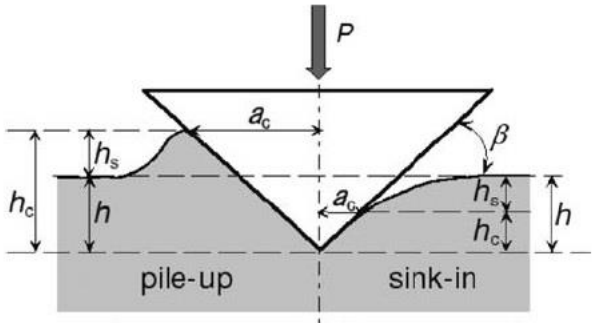

Fig. 18: Contact profiles (pile-up and sink-in). h, h_s, and h_c are, respectively, the total depth, surface depth, and the contact depth of penetration. The contact radius is denoted by a_c [84]

In an indentation experiment the indent is applied on the surface of material to deform the bulk toward inside of the material, however, the creation of deformation in the material around the contact area is an inevitable outcome of the mechanical interaction. This deformation can take the form of either "sinking-in" or "piling-up." Sinking-in refers to the downward plastic deformation of the material around the indentation, causing it to be lower than the surrounding indented surface plane. Piling-up involves upward plastic deformation around the indentation, causing a raised region around

the indented area. The occurrence of pile-ups and sink-ins in indentation tests is closely correlated with the material properties, particularly its strain hardening behaviour. Materials with strong strain hardening tendencies are more likely to exhibit sink-ins, whereas those with weaker or no strain hardening may display pile-ups [90]. Those features can have a significant effect on the measured hardness. In case of pile-up the measured hardness in higher than what is should be and in sink-in, the measured hardness shows a lower hardness because they will change the actual surface in contact with the indenter and eventually the contact impression after removing the indenter [89].

The symmetry of the indenter tip dictates the symmetry of pile-up formed around the indent; Berkovich is an axis-symmetric tip generates axis symmetrical pile-up. The material deformation in the vicinity of contact area depends on material properties and the pile-up pattern depends on surface plane orientation [91].

Kucharski et al. [90] have done a thorough research on copper single crystal using Berkovich tip in different forces to study dependence of nanoindentation pile-up patterns on the indentation load and crystallographic orientation. They found out that pile-up patterns on the surfaces of (001), (011), and (111) oriented single crystals have fourfold, twofold, and sixfold (or threefold) symmetry and the indentation impression can be a combination of both pile-up and sink-in. The MD simulation of indentation in Nickel with different surface orientations [92] gives different responses in terms of hardness and elastic modulus. Also, the pile-up pattern shapes are different in different orientations. Experimental and simulation study of Aluminium with different surface orientations [93] shows a different response in terms of hardness and elastic modulus as well as dependency of pile-up on crystallographic orientation of the indented sample.

One reason that there are not enough studies in this area is because of complicated nature of these non-uniform deformation around indented impression. Number, direction, height, and shape of them varies with load, indenter type, material, and crystallographic orientation.

2.6.4 Calibration:

It is common practice to perform two-reference sample calibration of the Nanoindentation equipment before testing. The reason for having two-reference sample calibration is because two factor needs to be treated carefully to achieve an accurate calibration: Instrument stiffness and area function. Calibration is done by using the data from both reference samples and figure out the best frame compliance and area function. The sample with high modulus is utilized to the sake of finding stiffness and the sample with low modulus for indenter area function determination.

The compliance C_f of the loading instrument is defined as the deflection of the instrument divided by the load. The measured unloading stiffness dP/dh during an indentation test has taken instrument response into account as well as specimen, meaning the measured stiffness is sum of two resources. The contribution from the instrument, C_f, encompasses the compliance of the loading frame, the indenter shaft, and the specimen mount [81]. It is one of the main factors for uncertainty because the measured displacements are the sum of the displacements in the specimen and the frame [87].

The consideration of machine compliance is crucial in indentation tests. During indentation testing, the applied force not only acts on the sample but also on various components of the testing machine. This results in an increase in the measured indentation depth, leading to the underestimation of both hardness and elastic modulus.

Using all the above-mentioned matters, a configuration file was created which includes force-dependant frame compliance correction function and area function for 200mN to 1mN force range.

There is an theoretical area function for each type of indenter [81], however, to be more precise, area function for the indenter used for frame compliance measurement has been found out. Instead of measuring the cross-sectional area of the indentation, indentation depth could be measured automatically with high accuracy. This could then be converted to an area if the shape of the indenter was known. In practice, there is a difference between theoretical and actual geometry of indenter [81][94][95].

Two reference materials of certified elastic modulus and Poisson's ratio or certified plane strain modulus is used as a test piece. A combined iterative procedure to determine the frame compliance as well as the area function is adopted [94]. Young's modulus and Poisson's ratio are assumed to be independent of the indentation depth. A fit to the force removal curve was used to determine the contact size and stiffness from which the contact compliance can be related to the indentation modulus of the test piece:

Equation 2-28
$$Cs = \frac{\sqrt{\pi}}{2}\frac{1}{Er\sqrt{Ap}}$$

and

Equation 2-29
$$\frac{1}{Er} = \frac{1-\nu s^2}{Es} + \frac{1-\nu i^2}{Ei}$$

C_s is the compliance of the contact, dh/dF, at maximum applied force (reciprocal of the contact stiffness) after correction for machine compliance, C_f; E_r is the reduced modulus; A_p is the projected

contact area, value of the indenter area function at the contact depth defined in the same way as for the calculation of hardness according to ISO 14577-1:2015, A.4; v_s is the Poisson's ratio for the test piece; v_i is the Poisson's ratio for the indenter (for diamond, it is equal to 0,07); E_s is the elastic modulus of the material; E_i is the elastic modulus of the indenter (for diamond, it is equal to $1{,}141 \times 10^6$ N/mm2) [96] [82].

A variable epsilon (ε = 0,75 for most metals) and radial displacement correction was used. ε describes the ratio between the elastic deformation above and below the contact area. The radial correction is very small for most metals (<0,5 %) [82].

One advantage of using a modulus as the reference property is that the elastic response of the test piece is not sensitive to work hardening or thermal treatment or to the exact amount of creep that has occurred. All that is required is that the creep rate during force removal be negligible with respect to the force removal rate of the indentation experiment. Another advantage is that Elastic modulus can be determined independently by non-indentation techniques.

The total measured compliance, C_T, is the sum of contact compliance, C_s, and the machine compliance, C_F, as given in Formula:

Equation 2-30 $$C_T = C_S + C_F$$

CT and CS are calculated as below:

Equation 2-31 $$C_T = [\frac{dF}{dh}]^{-1}$$

Equation 2-32 $$C_S = \frac{\sqrt{\pi}}{2} \cdot \frac{1}{Er\sqrt{Ap(hc)}}$$

Equation 2-33 $$\frac{1}{Er} = \frac{1-\nu s^2}{Es} + \frac{1-\nu i^2}{Ei}$$

Equation 2-34 $$h_c = h_{max} - \varepsilon F_{max} C_T$$

Therefore, gives the total compliance:

Equation 2-35 $$C_T = \frac{\sqrt{\pi}}{2E_r} \cdot \frac{1}{\sqrt{A_P.h_c}} + C_F$$

2.6.5 Atomic force microscopy:

Though nowadays Nano indentation equipment is capable of measuring of the indented area through contact mechanics, a direct measurement of the indent sizes exhibits a more accurate determination of the hardness of the test specimen. AFM is a suitable technique because of its ability to acquire

three-dimensional images at an excellent resolution for relatively small indents. a sharp tip at the end of a cantilever is used to scan the sample surface; the deflection of the cantilever is measured using a laser reflected off the top of the cantilever and onto split photodiode [72]. Another reason for reliability of AFM over continuum mechanics is that two major factors can be considered. The first involves a correction for material pile-up (or sink-in) and the second one involves correction for tip roundness or in the other words, blunting of the apex into a roughly spherical shape [97]. The effect that tip-roundness can have on the measurement has been demonstrated in picture 19.

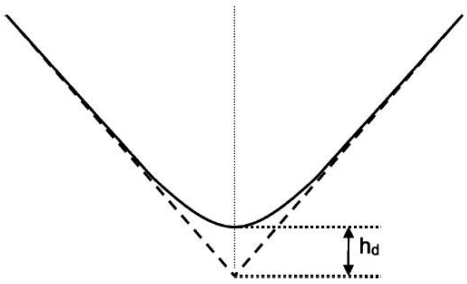

Fig. 19: Schematic picture of a tip with roundness which can affect the correct indentation depth [98]

Significant errors can be introduced into the measurement if the projected area of the indentation contact is not known with sufficient accuracy. The variation in area through pile-up, sink-in, tip roundness and residual stress will affect measured hardness directly and measured elastic modulus indirectly through miscalculation of contact depth.

Other efforts, rather than using AFM, have been made in order to find a way to compensate for pile-up or sink-in i.e. Oliver and Pharr [88] have developed a method for pile-up correction without involvement of indentation impression imaging. Below mentioned equation has been used for hardness correction. It has been derived from the work of indentation, which can be measured from the areas under loading and unloading curves of an indentation.

Equation 2-36 $H = 4 \times F \times E^2 / \pi \times S^2$

Where S is stiffness (µm/mN), a is area of contact from radius of indentation, E is Elastic moduli (GPa), H: hardness (GPa), F: applied force (mN) and they are related to hardness correction equation through those relation:

Equation 2-37 $S = 2 \times a \times E_r$

Equation 2-38 $H = F/A$

Equation 2-39 $A = \pi \times a^2$

Force (F) – hardness (H) and Force (F) - elastic modulus (E) graphs were drawn for each sample (crystallographic orientation) and each indentation orientation.

As examined by the test results of this work, the obtained elastic modulus and hardness values for different indentation orientations are different for each sample. This method cannot be a solution to avoid using direct indent impression measurement due to high uncertainty of stiffness especially in metallic materials since the elastic deformation is limited and therefore the slope of the unloading curve is steep.

2.7 Stacking Fault Energy:

Stacking fault is known to be a fundamental property of metals to influence various mechanical properties. Many investigations have been performed whether experimental or simulations to find out effect of alloying and their proportion on stacking fault energy. Those studies are utilized as one of the main factors in alloy designing. Fatigue properties, crack growth and fracture behaviour are some examples which are affected by stacking fault energy.

Crystals are made of lattices packed next to one another and each lattice is constructed by bonding of atoms. Regular sequence of construction of lattices and crystals can be described as a stack of atomic layers arranged. Any change which can alter that arrangement in crystal creates a defect. A stacking fault is a planar defect caused by irregularity in the planar stacking sequence of atoms and, as its name implies, it is a local region in the crystal where the regular stacking sequence of atomic layers is interrupted. They destroy the perfection of the host crystal, and the associated energy per unit area of fault is known as the stacking-fault energy [11][70]. When a dislocation splits into Shockley partials, because movement in the direction of burger's vector is difficult since each atom would need to climb over two atoms in the bottom plane, it is still able to glide on the same glide plane as the perfect dislocation. Also, the sum of strain energy of the burger's vectors of the two partial dislocations is less than the burger's vector of the full dislocation which makes the split a favourable mechanism. Those partial dislocation create stacking fault in the structure. Figure 20 shows the creation of partial dislocations. The spacing between partials is defined by the balance between repulsive forces due to stress field around partials and attractive force due to the stacking fault energy γ [99][100].

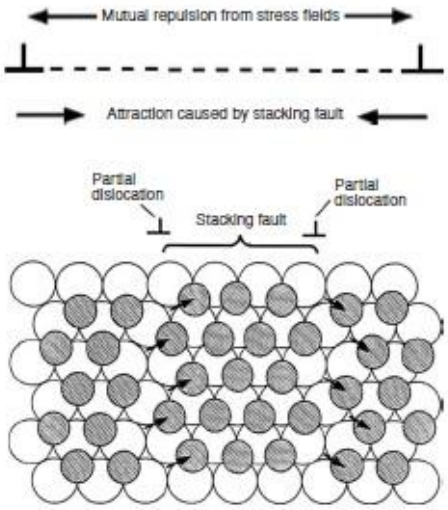

Fig. 20: Partial dislocation creation in a face-centred cubic lattice as viewed when looking down on the slip plane [101]

It was believed that different deformation mechanisms have different attributes which brings different contribution of different mechanisms to materials and give them different characteristics, however, recent literatures indicate that stacking fault energy might be the determinant factor which determines deformation mechanism which is the origin of mechanical properties characteristic of materials. For instance, it was for many years believed that twining is an autonomous deformation mechanism which happens when material undertakes load; however, recently, it has been pointed out that twining is formed from two stacking faults. Another assumption about the origin of the effectiveness of solid solution strengthening which affects mechanical properties of pure metals strongly by forming alloy can be explained by changing of energy in atomic interaction which affects stacking fault energy and eventually it gives different property to it.

As a matter of fact, both strength and ductility are affected by dislocation generation and dislocation movement respectively. On the other hand, stacking fault is defined as two partial dislocations. Therefore, a better explanation of its generation and its movement seems to be the key factor in mechanical properties enhancement. Among all parameters which should be considered to affect strength and ductility, the importance of stacking fault energy is studied during our research. To capture SFE effect the best, other strengthening parameters e.g. alloying, grain boundary, precipitates have been avoided and hence, pure single crystal have been chosen.

Conducting investigation about microstructural change and mechanisms happening in plastic deformation of face-centred cubic metals necessitates familiarizing with the term stacking-fault energy, γ, as an important parameter metals because it controls to a large extent the ability of screw and edge dislocations to cross-slip and climb respectively and the probability of the occurrence of these mechanisms is dependent on the degree of dislocation dissociation [102]. Consequently, this

determines the mobility and possibility of entanglement of dislocations. The combination of those represents work-hardening for single crystals and poly crystals affecting their deformation texture.

When considering cross slip, which is the movement of a (screw) dislocation onto a slip plane that overlaps the dislocation's original slip plane, the stacking fault energy is important. One mechanism given a dislocation when it comes into contact with a barrier is cross slip. A dislocation's ability to cross, slip around, and avoid an obstruction decreases the obstruction's power to prevent dislocation motion. The split dislocation must be combined back into the unit dislocation before an extended dislocation, which is a dislocation divided into partial dislocations, can cross slip. With widely spread partial dislocations this unification process is more challenging as opposed to narrowly spaced partial dislocations. Therefore, compared to materials with high stacking fault energies, low stacking fault energies are less likely to encourage cross slip. Additionally, it has been found that materials with low stacking fault energies are more likely than those with high stacking fault energies to deform by twinning [99].

As explained above, the general idea of stacking fault energy has been known for decades. However, since scientists and engineers have been trying to utilize stacking fault to enhance mechanical properties of metals e.g., Twinning induced plasticity (TWIP) steels, they came across different terms which are used for stacking fault and stacking fault energy which they have found through different methodologies. Variety of methodologies in one hand and intrinsic properties of materials on the other hand, has led to difference in measurement of stacking fault energy [103][104]. Therefore, there is a need to distinguish between different terms such as generalized and unstable stacking fault energy, intrinsic and extrinsic stacking faults which are used to address stacking fault. Even there is a possibility to have different stacking fault width in the same material due to dissociation of different types of full dislocation [105].

The perfect dislocation with Burgers vector b_1 therefore splits up or dissociates into two dislocations since it is energetically favourable to have two Burgers vectors of b_2 and b_3 [11]:

Equation 2-40 $$b_1 \rightarrow b_2 + b_3$$

Thompson tetrahedron as shown in figure 21 can display the plane and direction of full/perfect dislocation in different planes and directions for FCC metals and the possibilities for dissociation of them into partial dislocation in. It can be seen that a perfect dislocation can be dissociated into two partial dislocations [106]. Since dislocation energy is proportional to square of burger's vector, dislocations with the shortest possible Burgers vectors are stable [70].

Equation 2-41 $$\frac{a}{2}[\bar{1}10] \leftrightarrow \frac{a}{6}[\bar{1}2\bar{1}] + \frac{a}{6}[\bar{2}11]$$

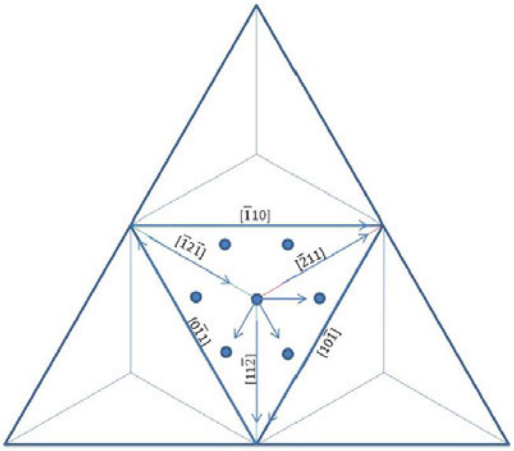

Fig. 21: the relationship between the perfect and partial dislocations [106].

Moreover, it is worth mentioning that the Burgers vectors [110], [121] and [211] are in the (111) plane. In addition, the same plane contains two perfect dislocations [101] and [011], which can be dissociated into [112], [211] and [121], [112], respectively.

The idea of stacking fault has been discovered in FCC metals and hence, the phenomena was named stacking fault energy. Since then, endeavours have been done to find out staking fault in BCC metals using different methods. It has been found out that stacking faults in BCC metals are unstable and therefore the term unstable stacking fault energy was applied to indicate the difference between the stacking fault energy in FCC and BCC metals [107].

Stacking fault has been observed frequently in FCC metals. In the beginning, stacking fault energy was measured experimentally by means of TEM. There are different experiments which can lead to the measurement of dissociation of partial dislocations that does not always give the same result for stacking fault energy. Additionally, there has been a relatively high uncertainty involved in the results and the reliability of methods such as using stacking fault tetrahedra has been questioned [108]. Another variable which can cause a difference in the measurement is whether the stacking fault is intrinsic or extrinsic and even co-existence of the both has been observed [109]. It has been brought into consideration that some measurement methods are more applicable for low stacking fault energy metals and some others are more suitable for high stacking fault energy ones [110][111].

Recently, simulations have shown a very good agreement with experimental results. FCC materials show one distinct minimum in the change of the total potential energy in perfect samples during rigid sliding unlike BCC materials which either do not show or have more than one minimum which indicates unstable stacking fault.

It was believed that stacking fault does not occur in body centred cubic metals. A reason could be that BCC metals are not closed packed structure. However, further experimental studies and later on with

the help of simulation practices, it was proved that stacking faults can happen though it is not a favourable deformation mechanism in body centred cubic metals and therefore, it is not common to be observed. The studies based on theoretical calculation and simulation has indicated the existence of unstable stacking faults [112][113][114][115][116][117].

Vitek [112] studied the generation of stacking faults (SFs) and multilayer twins on the {112} planes in perfect BCC crystals and concluded that intrinsic SFs are unstable, while extrinsic three- and four-layer SFs (3SF and 4SF), or multilayer twins may be stable in BCC. A. Machova et al found the same result in their work using molecular dynamics simulation in <111>{112} slip systems. Planes {010} and {211} planes do not possess any local minima and, therefore, no stable single layer stacking faults are likely to exist on these planes. Since mechanical twinning takes place on {211} planes in BCC metals, Stable n-layer faults on {112} planes in BCC metals can exist. When the number of layers is increased, fault converge towards becoming a micro twin [112][113]. development of a SF in the different directions of a crystallographic plane does not exhibit local minima in BCCs [118]. single layer SFs only form in FCCs where such minima are encountered. Twinning in BCCs involves growth of multiple layers of parallel {112} SFs. It appears that any stacking faults will most probably form either on {112} planes, where a fault could be considered as a monolayer twin, or on {110} planes. R.Pegel [119] has calculated maximum stacking fault energy for Va and VIa transition metals and iron by assuming a glissile type splitting of a pure screw dislocation on a {110} plane, however, in another study the author concluded that the existence of the stacking fault energy can neither be proved nor rejected [120].

Two methods have been used to find out SFE for different materials. Experimental methods including loop annealing, absence of tetrahedra, twin energy, extended nodes, faulted dipoles, extrapolated node data, separation of partial dislocation, creep data, rolling texture, isolated dislocation and double ribbon and calculation based on simulation including modified embedded atom method, density functional theory, thermodynamic modelling.

In the following paragraphs, various methods have been mentioned for calculation of stacking fault energy. A literature survey was done to find the stacking fault energies of different materials. Table 1 shows the stacking fault energy of different metallic materials which were found during literature survey:

Table 1: Stacking fault energy of the pure metallic materials

Specimen	SFE range (GSFE/USFE) [mJ/m2]	Methods of obtaining stacking fault energy
Al (FCC)	135 - 280	Density functional theory (DFT) as implemented in the Vienna Ab initio Simulation Package (VASP) [121], First-principles density functional theory DFT and the embedded-atom method EAM [122], Different experimental methods [123], second nearest-neighbour (2NN) MEAM [124]
Ni (FCC)	95 - 450	second nearest-neighbour (2NN) MEAM [124], Different experimental methods [123], Weak-beam technique: dissociated glide dislocations and faulted dipoles [104], Extended dislocation nodes [125]
Pt (FCC)	111	second nearest-neighbour (2NN) MEAM [124]
Cu (FCC)	24 - 165	Extended dislocation nodes [126][125], Different experimental methods [123], second nearest-neighbour (2NN) MEAM [124], Separation of partial dislocations - Weak beam technique [127], Two embedded atom method (EAM) [128]
Au (FCC)	10 - 61	First-principles method based on density functional theory (DFT) [129], Different experimental methods [123], second nearest-neighbour (2NN) MEAM [124]
Ag (FCC)	16 – 43	Different experimental methods [123], Separation of partial dislocations from Weak beam image [127], Extended dislocation nodes [125], second nearest-neighbour (2NN) MEAM [124], Two embedded atom method (EAM) [128]
Pb (FCC)	9	second nearest-neighbour (2NN) MEAM [124]
Si (face-centred diamond-cubic)	30 - 110	Width of the ribbon; Geometry of extended node [109], Different experimental methods [123]
Austenitic stainless steel (FCC)	18 – 35	Isolated dislocation method; First principle calculation method [106], Isolated dislocation method; Extended nodes [130]
Fe (BCC)	470-1860 150 (calculated)	First-principles method based on density functional theory (DFT) [131], Molecular dynamics (N-body GA potential) [116], DFT calculations and CI-NEB method [132], Theoretical calculations of splitting a dislocation [119]
Ta (BCC)	723-1000 220 (calculated)	DFT calculations and CI-NEB method [132], Molecular dynamics using LAMMPS [114] [117], Phase-field dislocation dynamics (PFDD) using DFT [133], Theoretical calculations of splitting a dislocation [119]
Mo (BCC)	3[110]00-1800 410 (calculated)	DFT calculations and CI-NEB method [132], ab initio electronic-structure calculations [115], Phase-field dislocation dynamics (PFDD) using DFT [133], Theoretical calculations of splitting a dislocation [119]

Table 1 continued: Stacking fault energy of the pure metallic materials

V (BCC)	308-815 160 (calculated)	Phase-field dislocation dynamics (PFDD) using DFT [133], Theoretical calculations of splitting a dislocation [119]
Nb (BCC)	190-768 190 (calculated)	Phase-field dislocation dynamics (PFDD) using DFT [133], Theoretical calculations of splitting a dislocation [119]

In small scales there are different factors which affect the stacking fault energy of materials such as elements, crystallographic orientation, and proximity to a grain boundary. In order to reduce the number of factors which affect SFE and eventually to eliminate uncertainties as much as possible, pure single crystal metallic materials with known orientation have been chosen. Hereby, the effect of elements and grain boundary effect have been removed and a better judgement can be given for dislocation generation and movement regarding crystallographic structure.

Higher SFE means separation of partial dislocations is more difficult, therefore, facilitates dislocation mobility and easier dislocation mobility assumed to facilitate dislocations movement to further distances. Low SFE materials display wider stacking faults and have more difficulties for cross-slip. The SFE describes the ability of a dislocation in a crystal to glide onto an intersecting slip plane. Lower SFE restricts the mobility of dislocations [49].

2.8 Elastic Modulus:

Elastic modulus is one of the test results that is directly obtained from measurement using stiffness, S, which is measured directly and contact radius, a, which is calculated through predefined area function that is function of indentation depth. There is a need to confirm the measurement of elastic modulus by comparing it with a reference elastic modulus which can be calculated for each specific material as explained thoroughly in this section of the thesis.

The values mentioned in the Table 2 were taken for calculations of the isotropic elastic modulus (Hill's average elastic modulus [134]) and shear modulus, stiffness constants of elasticity matrix, Poisson's ratio and Burger's vector of the samples has been obtained from various researches [135].

Table 2: Poisson's ratio and Burger's vector

Specimen	Crystal Structure	Poisson's ratio	Burger's vector [nm]
Al	FCC	0.3453	0.286
Ni	FCC	0.31	0.249
Pt	FCC	0.3952	0.277
Cu	FCC	0.3436	0.256
Ag	FCC	0.3641	0.288

Table 2 continued: Poisson's ratio and Burger's vector

Au	FCC	0.4236	0.288
Fe	BCC	0.2880	0.248
V	BCC	0.3614	0.262
Ta	BCC	0.3374	0.286
Mo	BCC	0.2926	0.272

Below equations have been used for calculation of Voigt-Reuss-Hill bulk elastic modulus average using C_{11}, C_{12}, C_{44} to create stiffness matrix. Density and Poisson's ratio have been obtained from previous research done in this area.

Voigt-Reuss-Hill approximation converts elastic constants of the single crystals into isotropic polycrystalline elastic moduli. Since elasticity in single crystals is not isotropic.

In fact, the general form of the Hooke's law for the 36 elastic constants is given by the following stiffness tensor [136]:

Equation 2-42

$$C = \begin{bmatrix} C_{11} & C_{12} & C_{13} & C_{14} & C_{15} & C_{16} \\ C_{21} & C_{22} & C_{23} & C_{24} & C_{25} & C_{26} \\ C_{31} & C_{32} & C_{33} & C_{34} & C_{35} & C_{36} \\ C_{41} & C_{42} & C_{43} & C_{44} & C_{45} & C_{46} \\ C_{51} & C_{52} & C_{53} & C_{54} & C_{55} & C_{56} \\ C_{61} & C_{62} & C_{63} & C_{64} & C_{65} & C_{66} \end{bmatrix}$$

In cubic crystal structures (including FCC and BCC), the elasticity matrix can be expressed in terms of three independent elastic stiffness constants due to the symmetry of the crystal lattice. This symmetry arises from the fact that the x-, y-, and z-axes are identical. Therefore, $C_{11} = C_{22} = C_{33}$, $C_{12} = C_{21} = C_{23} = C_{32} = C_{13} = C_{31}$, and $C_{44} = C_{55} = C_{66}$. In addition, the off-diagonal shear components are zero which means $C_{45} = C_{54} = C_{56} = C_{65} = C_{46} = C_{64} = 0$. So the stiffness tensor can be simplified into a three variable independent form as [134][137],

Equation 2-43

$$C = \begin{bmatrix} C_{11} & C_{12} & C_{13} & 0 & 0 & 0 \\ C_{21} & C_{22} & C_{23} & 0 & 0 & 0 \\ C_{31} & C_{32} & C_{33} & 0 & 0 & 0 \\ 0 & 0 & 0 & C_{44} & 0 & 0 \\ 0 & 0 & 0 & 0 & C_{55} & 0 \\ 0 & 0 & 0 & 0 & 0 & C_{66} \end{bmatrix}$$

Because of average effect of elastic constants, the indentation modulus of a crystal is believed to depend on the tip shape used in the test. Indentation of a Berkovich indenter into surface of the specimens creates a three-dimensional elastic field beneath the indenter which makes the Hill average elastic modulus a suitable measure between theoretical and experimental outcome.

Using C_{11}, C_{12} and C_{44} elastic constants [138][139], Voigt and Reuss elastic modulus can be calculated for each material. Voigt-Reuss-Hill elastic modulus is the average of Voigt and Reuss elastic modulus which are the upper and lower bound for elastic modulus [140][141].

Equation 2-44 $$B_{VRH} = \frac{C_{11} + 2C_{12}}{3}$$

Equation 2-45 $$G_V = \frac{C_{11} - C_{12} + 3C_{44}}{5}$$

Equation 2-46 $$G_R = \frac{5C_{44}\,(C_{11} - C_{12})}{4C_{44} + 3(C_{11} - C_{12})}$$

Equation 2-47 $$G_{VRH} = \frac{G_V + G_R}{2}$$

Equation 2-48 $$E_V = \frac{9\,G_V\,(B_{VRH})}{(3\,B_{VRH} + G_V)}$$

Equation 2-49 $$E_R = \frac{9\,G_R\,(B_{VRH})}{(3\,B_{VRH} + G_R)}$$

Equation 2-50 $$E_{VRH} = \frac{E_V + E_R}{2}$$

For anisotropic material, there will be a difference in properties based on the crystal orientation. Theoretical elastic modulus for different orientations have been calculated to be compared with experimental results [117].

Equation 2-51 $$E_{100} = \frac{(C_{11} + 2C_{12})(C_{11} - C_{12})}{(C_{11} + C_{12})}$$

Equation 2-52 $$E_{110} = \frac{4C_{44}(C_{11} + 2C_{12})(C_{11} - C_{12})}{4C_{44}(C_{11} + C_{12}) - 2C_{44}(C_{11} - 2C_{12}) + (C_{11} + 2C_{12})(C_{11} - C_{12})}$$

Equation 2-53 $$E_{111} = \frac{6C_{44}(C_{11} + 2C_{12})(C_{11} - C_{12})}{6C_{44}(C_{11} + C_{12}) - 4C_{44}(C_{11} - 2C_{12}) + (C_{11} + 2C_{12})(C_{11} - C_{12})}$$

The result of the calculations as per above-mentioned equations have been summarized in the Table 3.

Table 3: Calculated average Voigt-Reuss-Hill shear and elastic modulus and for each crystallographic orientation using elastic constants.

Specimen	C_{11}	C_{12}	C_{44}	G_{vrh} [GPa]	E_{vrh} [GPa]	E100 [GPa]	E110 [GPa]	E111 [GPa]
Cu	169.6	122.4	75.4	47.414	127.364	66.985	130.700	331.695
Fe	231.4	134.7	116.4	81.826	210.797	132.279	220.414	476.770
Ni	248.1	154.9	124.2	83.852	218.383	129.023	227.343	515.623
Pt	346.7	250.7	76.5	63.459	177.116	136.286	185.283	388.850
Al	106.75	60.41	28.34	26.144	70.352	63.086	72.031	136.133
Ag	122.2	90.7	45.4	29.719	81.098	44.919	84.065	209.687
Au	192.9	163.8	41.5	27.279	77.703	42.462	80.697	214.754
Nb	240.19	125.58	28.22	37.631	104.838	153.959	90.978	151.874
Ta	260.23	154.46	82.55	69.053	184.734	145.166	192.682	383.929
V	228.7	119	43.15	47.502	129.342	147.244	124.575	218.496
Mo	463.7	157.8	109.2	125.004	323.166	383.568	306.564	511.774

Summary:

In this chapter of my work, at first, the motive of the work, the phenomenon, called size effect and the observations and conclusions that were obtained by other researchers were discussed. Afterwards, the models designed to help understanding of the size effect were described and the reason why a model based on slip distance theory might be a better approach was explained. Eventually, the reference values calculated and/or collected, specifically elastic modulus and stacking fault energy, from other works of various body of research were demonstrated.

Size effect has been discovered in previous studies has been reviewed. Different test experiments have been used to study size effect and it has been repeatedly observed in Nanoindentation. Various models have been suggested to explain size effect in nanoindentation, however, the models fail in different scales or not compatible for other materials. There is still not an agreement among researcher in explanation of size effect phenomena. Several modifications have been done but each one has worked out for a specific material or a specific range of length scale.

In this study a new model is used along with a comprehensive set of single crystal metallic materials to be tested in micro- and nano length scales to give a new way of explanation about size effect.

Stacking fault energy was collected from previous studies to sort out the materials based on that and be able to compare them. In spite of difference in the measured or calculated stacking fault energy of the materials, the most reliable value which majority of the studies have agreed upon and used was chosen in this study.

In order to make sure about the validity of the experiments, elastic modulus was calculated for each material and since elastic modulus is an intrinsic properties and size effect does not have influence on it, it can be used as a reference to make sure about the authenticity of the collected data.

Strength and ductility are affected by dislocation generation and dislocation movement respectively. Dislocation generation and its movement seems to be the key factor in mechanical properties enhancement. A factor which has an influence on both elements is stacking fault energy. To capture SFE effect on size effect the best, other strengthening parameters i.e., alloying, grain boundary, precipitates have been avoided and pure single crystal have been chosen.

Size effect has shown that the strength of the material, for the sake of this research hardness, is not constant throughout the various length scales. Yet the explanation lies within dislocation generation and mobility. Therefore, stacking fault energy seems to be a key factor to affect the response of the materials in smaller scales and to explain where the rise of hardness happens and how it happens. Having a high or low stacking fault energy intensifies the rise in hardness?

2.9 Aim of the work:

Different strengthening mechanisms have been proposed throughout the years to explain the behavior of materials under loading. Being able to carry out investigation in smaller scales have brought cases which could not be completely explained by previous theories and has led to new theories or modifications to previous ones in order to clarify materials' response. Size effect which has been observed in torsional testing, compression testing, and indentation testing has opened up a new horizon in understanding of materials response under loading and its interpretation by seeking a new description of microstructure-mechanical properties relationship. In the size regime between several tens of nanometres and a few micrometres, continuum mechanics approaches without an intrinsic length scale may not be appropriate for describing plastic deformation.

I believe that by employing Indentation instrumented testing (Nano-indentation) and atomic force microscopy (AFM) along with Scanning electron microscopy (SEM) attached with electron backscatter diffraction (EBSD) and using Transmission Kikuchi diffraction technique (TKD) on the lamellas taken out of indented samples by Focused ion beam (FIB) on different metallic materials a superior statement can be given to describe strength of material through their hardness. For that purpose, Hardness is divided into different factors in which each plays a role, and they can be a combined effect of either intrinsic properties of a material or testing characteristics.

In this work, I am aiming to have a better understanding of relationship between microstructure and intrinsic properties of metallic materials in one hand and their influence on mechanical properties

(particularly hardness) on the other hand, by nano indentation testing based on slip-distance theory and using Hou and Jennett equation in order to study influence of different factors including plastic zone size and dislocation density and be able to separate the influence of each factor on the collective response of materials and to explain size effect.

This work provides some of the significant findings related to size-scale strengthening effects and its relation to microstructural evolution which have been brought about through the use of instrumented indentation testing experiments. The contribution should be as mentioned below:

- Measure length scales size effect of pure metallic materials at micro- and nano scales using Nano indentation testing
- Compare indentation size effect in BCC and FCC structure single crystal metallic materials
- Quantify how SFE affects intensity of the change/rise in the hardness that is observed in size effect phenomena?
- Verify the generated model based on slip distance theory to quantify contribution of plastic zone size and dislocation density to strength/hardness in different length scales.
- Are different plasticity mechanisms responsible at different length scales and can this be quantified using the verified model?
- Verify Stacking fault energy (SFE) as a major plasticity mechanism in any of the identified length scales?

3. Methodology:

3.1 Sample preparation:

In order to have a comprehensive understanding of length scale size effect, various metallic materials with different crystallographic structures, crystallographic orientation and stacking fault energies were collected.

The materials have been chosen for this project based on their stacking fault energy and crystallographic structure including face centred cubic and body centred cubic (Table 4). In this study, the samples consisted of single crystals (Goodfellow Ltd., Cambridge, UK), specimens with a purity of 99.98% and higher have been used.

Table 4: Provided samples for this project.

Sample	Orientation	SFE [mJ/m2]	Purity
Al	001	≈ 180	99.999%
Ni	001	≈ 135	99.999%
Pt	001	≈ 120	99.999%
Cu	001	≈ 42	99.999%
Cu	110	≈ 42	99.999%
Cu	111	≈ 42	99.999%
Ag	001	≈ 21	99.999%
Au	001	≈ 11	99.999%
Fe	110	≈ 150	99.98%
V	110	≈ 160	99.99%
Ta	001	≈ 220	99.999%
Mo	001	≈ 410	99.999%
Nb	110	≈ 190	99.999%

Specimens were cut from wire shaped with 25mm in diameter samples supplied by Goodfellows using wire cutting with the lowest cutting rate possible to prevent inducing work hardening to the samples as much as possible. Each sample comes in a disk shape and has 3-4mm thickness after cutting.

The surface of samples was grinded starting from grit size of 800 to 2400 using SiC papers and mechanically polished using water based colloidal silica suspension starting from 9µm to 1µm and alumina suspension down to 0.06µm. It should be noted that the duration of each step and the applied force is slightly different from one sample to another. Samples were put in ultrasonic bath right after each stage of preparation process and were immediately kept in a vacuum adjacent to desiccator to reduce forming of oxide on the surface. It was checked by analysing loading force on the sample that if a sudden change in the force curve can be observed as a result of oxide layer, however, there was

no sign of that. Regardless of various surface preparation parameters attempted, there are samples which tend to create a work-hardened layer on the surface. Therefore, the surfaces were electropolished using relevant electrolyte suitable for each metal.

The appendix I illustrates the best parameters which were figured out through literature survey and also using trial and error method. The appendix II illustrates a case study of how nanoindentation result can be affected by sample preparation.

3.2 Scanning Electron Microscopy/Electron Backscatter Diffraction:

The usage Electron backscatter diffraction (EBSD) coupled with scanning electron microscopy (SEM) has risen exponentially due to its magnification level and resolution to describe crystal misorientations, microstructure features and evaluating plastic deformation processes [142].

After sample preparation, SEM/EBSD was performed on samples to find out their crystallographic orientation and put a mark on the sample for its orientation for further Nano indentation experiments.

After sample preparation and before indentation, it is necessary to find out specimens' orientation since deformation is orientation dependant. For that purpose, the sample is tilted 70 degrees to detector using 20kV accelerating voltage to perform EBSD measurement. Using EBSD technique, not only crystallographic orientation of specimens is found out but also quality of preparation is evaluated since Kikuchi patterns needs to be revealed first. Figure 22 shows an example of the sample Cu 111 after rotating the specimen inside the SEM chamber. After rotation, sample was taken out and physically marked. Z direction is always crystallographic orientation and X direction was marked on the sample.

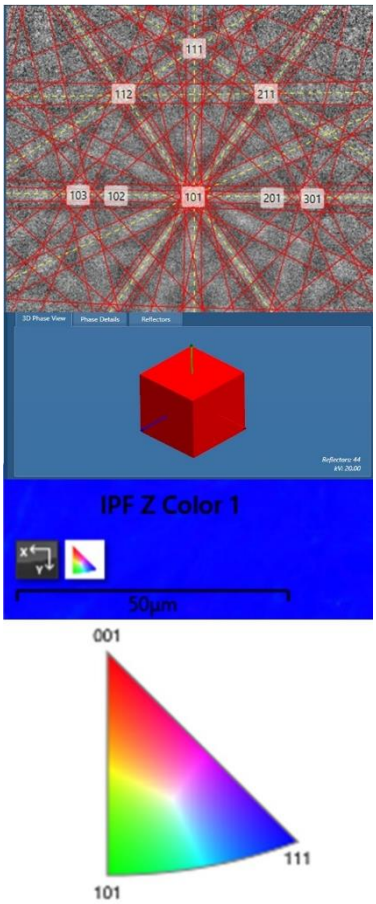

Fig. 22: Kikuchi patterns and crystallographic orientation of the Cu 111 specimen

SEM forms a magnified image by scanning the surface of a bulk specimen by a convergent electron beam using scanning coils. The interaction between electron beam and sample generates several kinds of signals which are detected by various detectors arranged near the specimen [143] [144] [145]. Commonly used signals are secondary electrons which are used for topography and morphology, X-ray for identifying chemical elements and Backscattered electrons.

Backscattered electrons (BSE) are electrons that are initially directed towards a target specimen but are then reflected back and captured for imaging within the scanning electron microscope (SEM). There are three discernible BSE signals. Atomic number or Z-contrast: This type of contrast is determined by the composition of the specimen, where variations in atomic numbers lead to differences in image contrast. Orientation contrast: In this case, the contrast in the image is dictated by the crystal structure of the specimen, resulting in variations based on different orientations within the crystal lattice. Electron channelling patterns (ECP): These patterns are distinctive for a specific crystal orientation and provide valuable information about the orientation of crystals within the specimen [145]. Figure 23 shows the schematic of the targeted area below the surface of the specimen and the scattered electrons coming from.

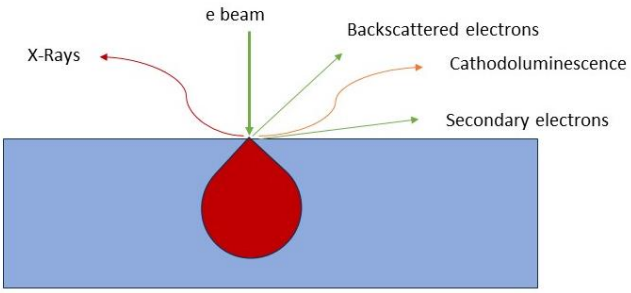

Fig. 23: schematic of the targeted area below the surface of the specimen and the scattered electrons coming from

The various emission signals observed in electron microscopy arise from electrostatic interactions between the incident or primary electrons and the target specimen. Secondary electrons are emitted due to inelastic interaction from the impact of primary electrons to the sample. Backscattered electrons are primary electrons that have been elastically scattered back from the target specimen and can be used to generate images based on composition and crystal structure [145].

EBSD is generally used for the orientation relationship determination, phase identification, plastic and elastic strain measurement and determination of grain boundary misorientation distribution. The grain orientation in a reference system attached to the sample is determined from the Kikuchi bands scattered from the crystal planes. Then, the misorientation between the neighbouring grains is calculated by suitable software [146]. The same way, Orientation differences between neighbouring points of a lattice curvature can be quantified and dislocation density can be calculated [147].

EBSD provides determination of crystallographic orientation and has the capability to link microstructure and crystallography and Crystallography is important in materials because in many cases the final properties of the material that make it useful are controlled or at least influenced by the crystallography of the sample.

Similar to most scientific techniques, electron backscatter diffraction (EBSD) also comes with its set of limitations. It can encounter challenges when dealing with heavily deformed materials, making it challenging to obtain meaningful results. Additionally, the minimum step size for bulk EBSD is approximately 50 nm, which is relatively large when compared to the minimum step size of about 2nm achievable with transmission Kikuchi diffraction (TKD).

3.3 Nano indentation:

A nanoindentation system is a precise instrument capable of measuring small displacements resulting from applied loads. It employs a well-established method in which an indenter tip with a known geometry is inserted into the surface of the material being tested. Once the indenter makes contact with the material's surface, the normal load steadily increases until it reaches a predetermined

maximum value. After reaching this maximum load, the normal load is gradually reduced until the force is completely removed. Throughout the experiment, the position of the indenter relative to the sample surface is meticulously tracked and recorded. Established mathematical model proposed by Oliver and Pharr [88] is then applied to this data in order to calculate quantitative values for hardness and modulus, providing valuable insights into the material's mechanical behaviour.

The collected materials were indented using universal Nanomechanical indenter ZHN (Zwick/Roell GmbH) as shown in figure 24.

Fig. 24: Universal Nanomechanical indenter ZHN used for indentation of the sample in this study.

The data went through filtration process to assure that each indentation is qualified to be among the collected data for further analysis;(a) the distance between curves of the same force is less than 2 standard deviations;(b) indented surfaces were checked; (c) Unloading curves were checked for fitting curve; (d) box and whisker plot was used for each force range to take out outliers.

The unloading curve is fitted between an upper (From) and a lower (To) force limit of the unloading curve by means of two different functions. These limits are expressed as a percentage of the maximum force. The upper was lie between 98% to 40% of the unloading curve data points. Stiffness is calculated using tangent of the unloading curve at maximum load, however, that adds inaccuracy in the slope of the tangent curve because of creep. Therefore, the start points to fit a curve to unloading curve was chosen slightly below maximum point (from 98%).

Figure 25 illustrates a part of the indentation array on Iron (left side) and Aluminium (right side) under optical microscopy which have been numbered for further examination using AFM.

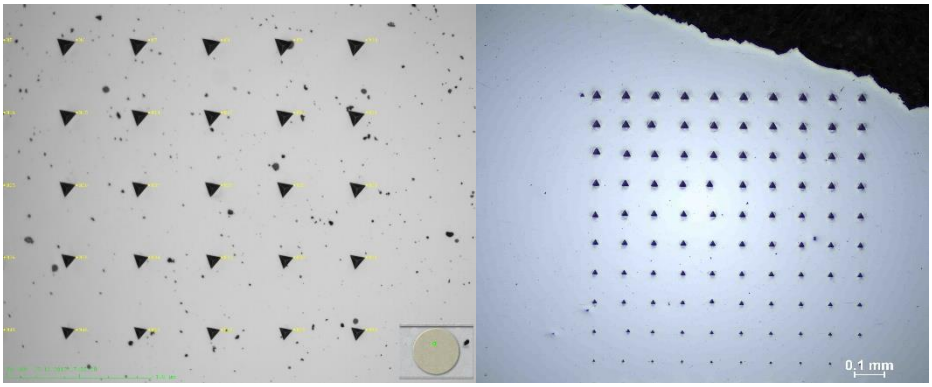

Fig. 25: Indentation arrays on Iron (left side) and Aluminium (right side)

3.3.1 Multi cycle Indentation:

There are different indentation methods such as multicycle, single cycle, QCSM and some methods which were tried during this study to find out a practical and accurate way of collecting the data. Each one has advantages and disadvantages.

Different force-displacement indentation methods were used to find out the best combination in order to have a low uncertainty in the collected data. To achieve that below mentioned parameters were considered:

- Elastic modulus response of materials given by indentation testing is used as a reference and compared with calculated hill average elastic modulus to check the amount of difference and the uncertainty.

- Since metallic materials have plastic characteristics, therefore, the elastic response in minor which means there will be a steep unloading curve which increases the uncertainty in stiffness (S). Hence, the chosen force-displacement indentation method must result in reliable and enough amount of stiffness measurement data to be averaged.

- On the other hand, to deal with contact mechanics drawbacks i.e., pile-up or sink-in and have an accurate measurement of contact area, atomic force microscopy (AFM) is employed to achieve a more precise hardness value. Therefore, the chosen force-displacement indentation method should be able to satisfy that as well.

Average, standard deviation and uncertainty of hardness, elastic modulus and stiffness were calculated after performing a series of measurement using various indentation methods.

Single cycle indentation gives an opportunity to measure every indented point using AFM, however, the collected data are going to be less than other methods i.e., multi cycle testing, which increases the level of uncertainty in our data.

Multi cycle indentation, with 10 increments, gives a large amount of data and a more continuous coverage of force range which satisfies the requirements of uncertainty reduction by having a large amount of data for averaging i.e., stiffness. A series of experiments were conducted using multi cycle indentation testing to assure the values for the same force obtained from different increments and they showed a very good agreement. The measured values for stiffness, hardness and elastic modulus were similar to single cycle testing. Tests gave reasonable measured elastic modulus which were of course slightly different from calculated hill average elastic modulus. The downside of using multi cycle indentation is though that only the highest force in the cycle (10^{th} increment) can be measured by AFM.

Strain rate is another factor which must be taken into consideration because it will affect the hardness and elastic modulus and can cause activation of thermally activated mechanisms [148].

The hardness and elastic modulus have been obtained using nanoindentation (ZHN) for metallic single crystals specimens from 1mN to 200mN force range using multicycle force-controlled method with the increment of 10% between forces. Due to the nature of multicycle indentation method, only the contact area of the last indentation can be measured.

Hardness was corrected using processed images achieved by atomic force microscopy (AFM) on test results to eliminate pile-up/sink-in and residual stress effects. Bearing in mind that there are several sources for residual stress, theoretical Hill's average elastic modulus was calculated and assumed as a reference value to ensure the correctness of the measurements, since elastic modulus is force independent and supposed to be an intrinsic property of materials. One should consider that elastic modulus from test results is not the right value to be used in the hardness correction equation since elastic modulus from test results have already been affected by pile-up or sink-in effect and residual stress on the surface of the samples.

3.3.2 Calibration:

In order to check the calibration of the Nanoindentation equipment, two reference sample called JGA and JGC with known elastic modulus were employed and indentation tests were performed on both using forces from 200mN to 1mN. Single crystal tungsten with the crystallographic orientation (100) and synthetic fused silica with the crystallographic orientation (311) serve specific purposes in the determination of frame compliance and establishing the indenter area function, respectively. Reduced elastic properties were assumed, for amorphous SiO_2: E=72.9±0.5 GPa and v=0.161, and for W: E=413.0±2.8 GPa and v=0.281 [149].

A complete frame compliance calibration has been performed using four reference samples with known elastic modulus and poison's ratio from 0.5mN to 200mN using ZHN nanoindentation machine. Multi cycle indentation has been used to collect enough points for each force. High and low ends of data acquisition frequency of 64Hz and 8Hz of the testing machine were examined for data collection. The data analysis of the test results indicates that scatter of the data is higher in higher frequency. However, operating at low frequency may not acquire enough data points for precise analysis. The collected data at each force have been analysed. A thorough analysis for the effectiveness of corrective frame compliance function in comparison with collected raw data and theoretical elastic modulus has been performed.

One aspect which should be taken into account when dealing with a wide range of the applied force is that in lower forces the importance of area function outweighs the frame compliance and in higher loads vice versa. Therefore, creating a configuration file for the calibration of the equipment remains a challenge.

Another fact regarding using reference materials is their limitation. fused silica has a tendency to crack is higher force as we observed for the forces above 90mN, and tungsten piles up. Figure 26 is optical microscopy images taken from reference materials which depicts the mentioned limitations.

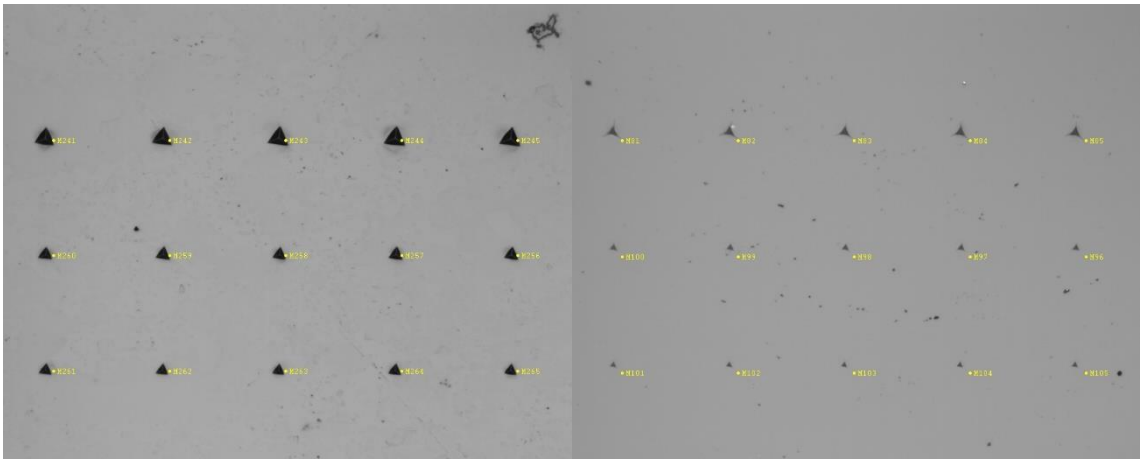

Fig. 26: Optical microscopy images of pile-up in Tungsten reference sample (left side) and crack in fused silica reference sample (right side) observed while using for equipment calibration.

3.4 Atomic force microscopy:

Due to the drawbacks of contact mechanics, direct measurement of indentation contact area (indentation impression) has become a common practice. Indented surfaces of the materials were scanned using atomic force microscopy NX20 from Park systems as shown in the figure 27.

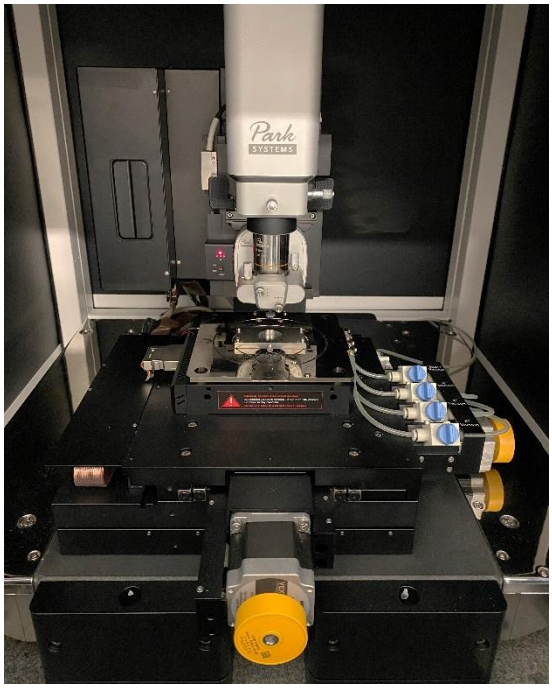

Fig. 27: Inside chamber of atomic force microscopy used for 3D scanning of the surfaces of indented materials.

Because of nature of contact mechanics which contains features like pile-up and sink-in, the hardness and elastic modulus values will be different from genuine values. When a material exhibits a pile-up effect during indentation, it undergoes deformation not only beneath the indenter but also experiences lateral movement or deformation around the indenter. This additional deformation leads to more material surface coming into contact with the indenter. However, because the contact area is typically calculated based on the depth from the surface, this extra surface involved in contact with the indenter (pile-up) is not included in the overall contact area measurement obtained by the nano-indentation equipment. Conversely, when a material displays a sink-in effect, the contact area between the material surface and the indenter is smaller than what is calculated by the equipment based on the indenter's depth from the material surface. Consequently, there exists a factor that introduces uncertainty into hardness measurements. One way to address this uncertainty is by employing atomic force microscopy (AFM) to directly measure and correct the contact area. This approach helps refine the accuracy of hardness results by accounting for the actual contact area between the material surface and the indenter, considering the effects of pile-up or sink-in.

Indented areas and surface roughness were measured using AFM. A contact mode tip was used. AFM enables us to have a 3D image of the impression. A colour scaling post processing is used to correlate the change in height of the scanning area. 256 x 256 pixels images were captured using AFM from the indentation impressions.

Since surface roughness is one of the sources of uncertainties and maximum surface roughness has been restricted to be 5% of the indentation depth [96], it was measured for all samples in three different location and the average value was recorded as surface roughness.

The images in figure 28 have been taken during AFM scanning from an indent. From this image, the depth and area are calculated. Also, indent characteristics such pile-up or sink-in behaviour is studied.

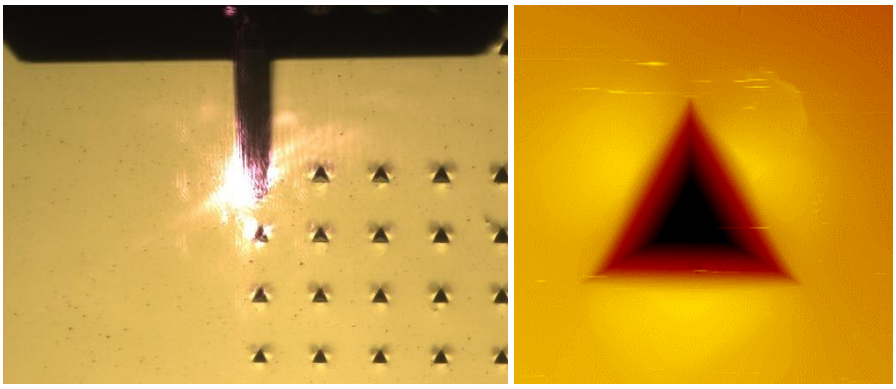

Fig. 28: AFM image taken from Al100 on a 100mN indent. Darker area indicates depth and lighter area indicates height of the measured area in comparison with the surface of the material.

Due to the complicated and non-uniform nature of pile-up and sink-in effects in one hand and the lack of an image processing software with good accuracy on the other hand, a custom-made MatLab program was employed [150] to process and calculate the contact area from the image created by AFM. A full description of how the code works has been explained in Appendix V.

Existence of pile-up and sink-in has been already proven in various literatures, however, what makes it complicated is the fact that the height and extension of them is different from material to material. Furthermore, it is seen that there is a possibility of having both pile-up and sink-in in an indentation impression. Though the highest height of pile-up usually happens in the middle of edge, for BCC material where there is four-folded pile-up, two pile-up has been observed on one edge and the middle of that edge is not the highest point. As a result, the corrected hardness graphs of different materials illustrate the different amount/percentage of change in hardness after correction.

Figure 29 shows the image generates using custom-made MatLab program [150] which identifies contact area and pile-up caused by indentation of single crystal of Aluminium.

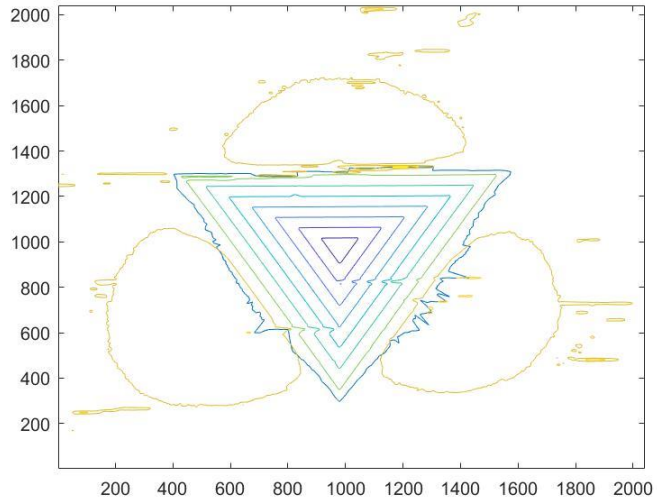

Fig. 29: Visualized indentation impression of Al100 using Custom-made MatLab program (at 90mN load). Indenter impression has been identified along with the pile-ups in the vicinity of each edge.

Four-folded image of pile-up in Molybdenum and Tantalum is seen clearly in images generated from AFM scans as shown in figure 30.

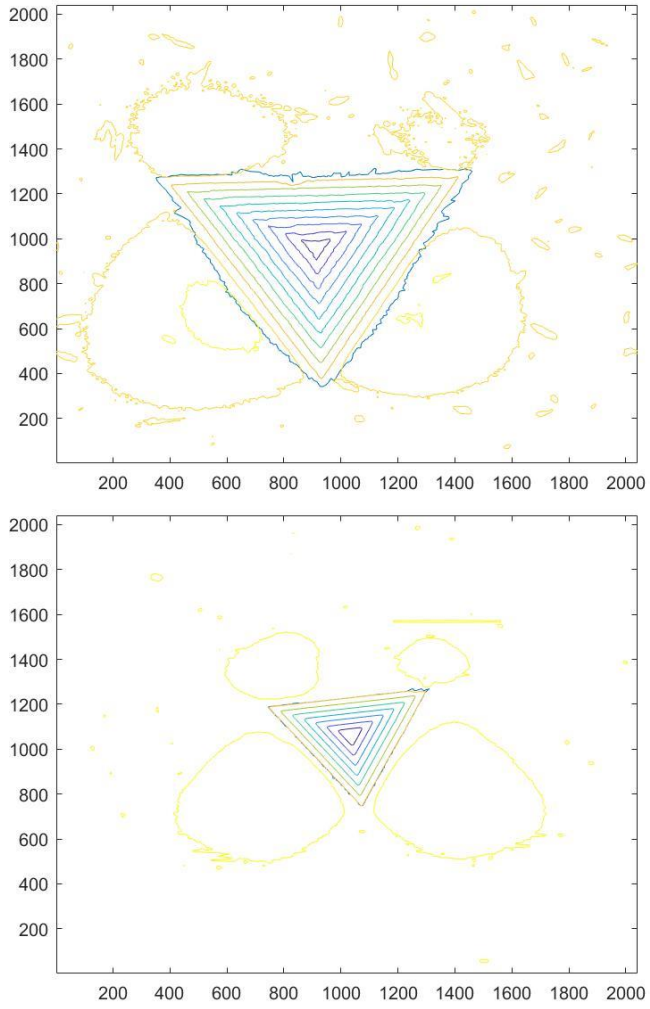

Fig. 30: Visualized indentation impression of Mo100 at 200mN load (image at the top) and Ta100 at 80mN load (image at the bottom) using Custom-made MatLab program. Indenter impression has been identified along with the pile-ups in the vicinity of each edge.

Another fact which can be clearly seen is the difference in pile-up/sink-in shape at different edge of indents.

As a matter fact, it is noticeable that all edges do not show the same type of deformation. For instance, as demonstrated in figure 31, in Mo100 there are pile-ups happening in the two upper edges and no phenomena in the middle of the lower edge.

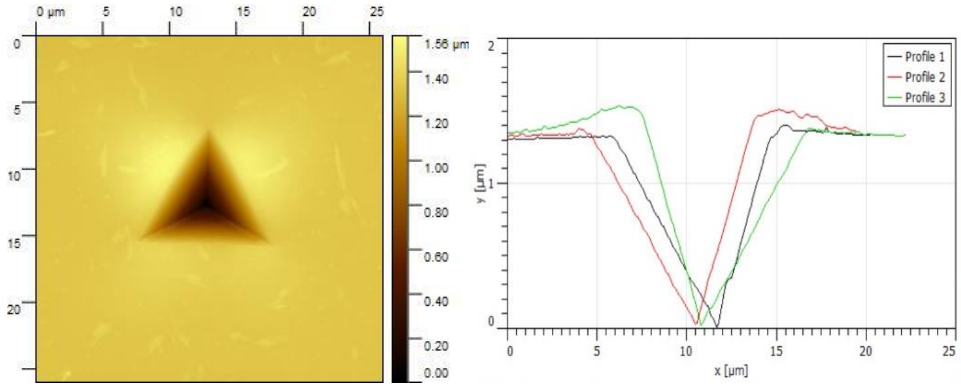

Fig. 31: Indented surface of Mo100 using Berkovich indenter by 100mN and the measured pile-up in the vicinity of each edge.

Further analysis of the contact area revealed the existence of four-folded pile-up in the lower edge as demonstrated in figure 30. In previous measurement, for the sake of comparison, all lines have been drawn through the middle of each edge, however, measurement of contact area, exposed the nature of pileups happening in the lower edge of Mo specimen.

Indented surface of Aluminium illustrates the same amount pile-up in all three edges (figure 32). A three-folded pile-up around the was observed. This finding does not agree with the finding of Mao Liu et al which observed a four-fold symmetry of the height profile for Aluminium in 100 orientation [93].

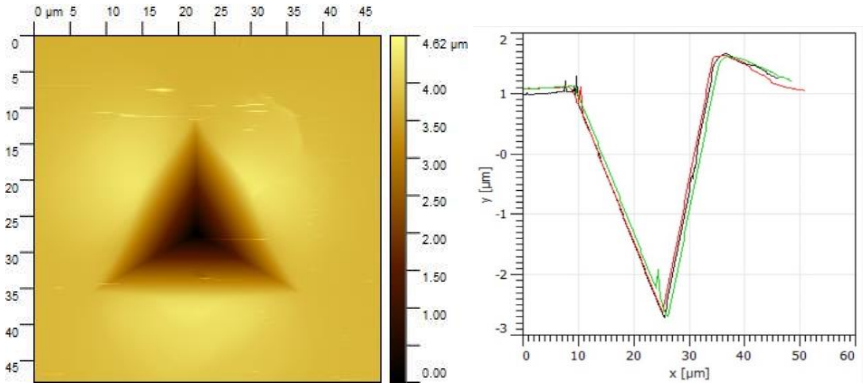

Fig. 32: Indented surface of Al100 using Berkovich indenter by 100mN in Perpendicular indenter orientation.

There is a difference between the extension of pile-up as well as their height between different samples.

3.4.1 Scanning of Indenter:

In practice, indenters are not perfectly sharp, and they typically have a finite tip radius. This tip radius is on the order of approximately 100nm [81]. Significant errors can be introduced into the measurement if the projected area of the indentation contact is not known with sufficient accuracy [151][152]. The rounding of the tip results in an initial elastic contact.

Indenter was scanned by means of AFM to capture an actual indenter area function entirely. The area function acquired by AFM was combined with frame compliance obtained from indentation on reference samples and the calibration configuration file of the ZHN Nanoindentation equipment was created. By using this method, a better area function considering indenter tip roundness can be met.

3.4.2 Drift correction:

Images went through drift correction process using Gwyddion software [153] before importing into Custom-made MatLab programme [150]. The drift causes a tilt/slope in the image during data acquisition while probing the surface which results in capturing a distinct image in comparison with genuine indentation impression.

3.5 Focused Ion Beam (FIB) and Transmission Kikuchi Diffraction (TKD):

Along with Nanoindentation, transmission Kikuchi diffraction (TKD) technique was employed to cross examine the interpretation of the analysed data and the conclusion that was achieved.

The increasing interest in quantitative measurement of plastic zone size and dislocation density was the motivation to use focused ion beam (FIB) to cut out a cross section of the indents from the bulk samples for cross section imaging using transmission Kikuchi diffraction (TKD).

The FIB is similar to the SEM as it is based on the same physics with the only difference being the usage of Ga ions instead of electrons [154][155].

At first, a protecting layer of platinum (Pt) is applied to the surface of interest and then milling process is done around it. A rectangular trench is cut out from both sides of the area of interest and then the bottom, left side, and a portion of the right side of the specimen is cut free. A needle is used to lift out the sample and place it on a grid where it may be used for further processing such as thinning. The method is done in a vacuum chamber the same as SEM which enables continuous monitoring of the process and progress of preparation [154][155]. After taking out the lamella, thinning process must be done to reach a thickness that the electrons hitting the surface of the lamella can transmit through it. Due to the nature of the thinning process, there is possibility of bending of the lamella because of the introduced strain due to indentation [156].

The lamellas taken out of the bulk samples using the above-mentioned technique were taken from the middle of the indents the way that the symmetry is contained on both sides of the lamella. On the

left-hand side the imprint is sectioned through the face of the indent, while on the right-hand side the cross-section proceeds right through the edge. Figure 33 illustrates performed trenching process and a schematic (and exaggerated) impression made by Berkovich indenter.

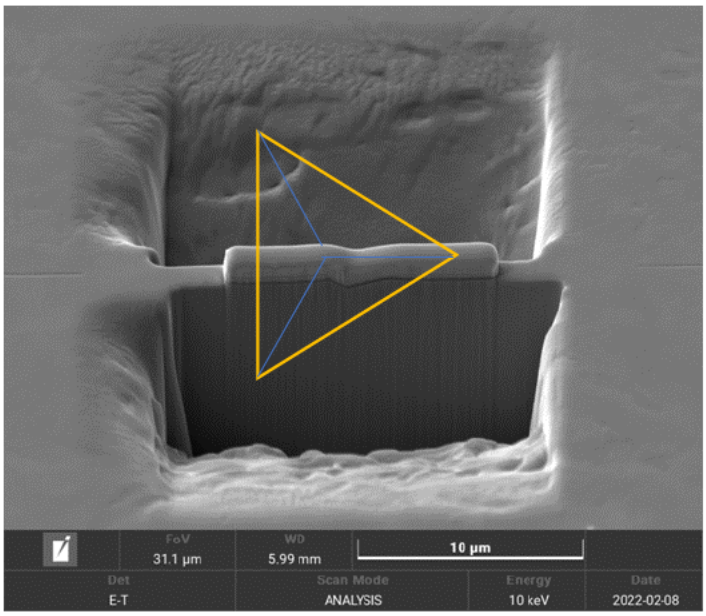

Fig. 33: An image taken during FIB to take out a lamella which shows the orientation of the lamella to correspondent indent. Please note that schematic picture of the indent is exaggerated.

Transmission Kikuchi diffraction (TKD) is used in a SEM chamber with a detector for Electron Backscatter Diffraction (EBSD). While EBSD studies diffracted electrons backscattered from the sample, TKD studies diffracted transmitted electrons. Unlike having 70° tilt to detector in EBSD, -20° is used. Sample thickness can be slightly thicker than TEM samples and a range of 80nm to 200nm has been suggested [157]. Figure 34 depicts the difference in those techniques.

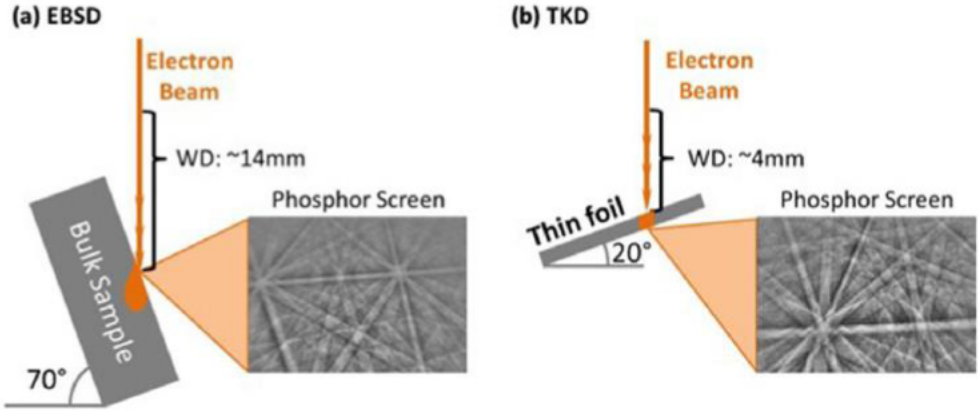

Fig. 34: Principle set-up of (a) EBSD and (b) TKD [158]

The benefit with TKD is the increased lateral resolution in comparison with EBSD which enables the investigation of dimensions down to 5nm compared with EBSD which has a lateral resolution of 25-

100 nm due to a larger excitation volume. This gives an advantage to have a better resolution to detect dislocation and misorientation [159]. EBSD has a good capability in showing overall lattice orientation change, however its weakness lies in revealing single dislocations in a discrete manner [52].

The studies have indicated that there is good agreement between the result of TKD and transmission electron microscopy (TEM) and TKD is has a good range of dislocation detection [158]. Also, technique is sufficiently sensitive to detect spatial and temporal distribution of the gliding dislocations activated in different slip systems which is utilized for quantitative measurement the local rotations [160]. That is attributed to the higher average energy and narrower energy spread [161]. Figure 35 represents the range and capability of TKD technique in comparison with other techniques.

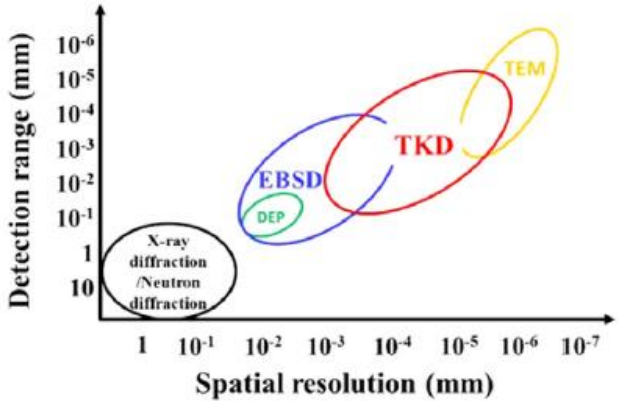

Fig. 35: Detection range and spatial resolution of different dislocation detection methods [158].

TESCAN AMBER FIB – SEM (Czech Republic) was employed to perform in-situ lift-out sample preparation. To begin with, a protective Pt using E-Beam 2kV 3nA was deposited on the indent surface followed by I-Beam 30kV 50pA and 30kV 150pA. Markers were made onto edge of Pt deposit using I-Beam 30kV 50pA to mark the centreline of the indent and area of interest. Trenches on both sides done using I-Beam 30kV 20nA followed by neater milling next to lamella 30kV 5nA.

Thinning process of the lamellas were done stepwise using FEI Helios 660 dual beam FIB. Thinning parameters of 30kV 0.79nA, 16kV 0.43nA, 8kV 0.21nA and 5kV 68pA were used to reach electron transparency. Then a final clean at 2kV 68pA.

For TKD investigation, the samples are mounted at 90 degrees to the stub and then tilted 70 degrees, so that makes the specimen tilt angle of 160 degrees. The sample is then moved very close to the electron source (working distance of less than 3mm), so that the EBSD pattern is recorded in transmission.

Post processing of TKD data was done using Aztec Crystal version 2.1 from Oxford Instruments.

Having TKD data and using Kernel Average misorientation (KAM), the change in misorientations, Specifically the change in crystal lattice orientation between different points in the material can be measured [162]. Misorientation over an area tend to increase with average plastic strain and this is the fundamental for quantification of plastic strain.

Summary:

In this chapter of my work, the techniques utilized to extract the required data for analysis were explained. The reasoning, pros and cons and importance of each one was clarified.

A careful consideration was devoted to choosing the most suitable indentation testing methodology. It was planned to collect high amount of data to be able to average them and reduce the uncertainty of the result and cover a large range in nano- and micro metre scales. Each section of load-displacement curve was set properly and after performing various tests to avoid collateral influence on the collected data. The indentation parameters were adjusted to result in a righteous unloading curve which gives stiffness and eventually elastic modulus and hardness.

There are limited ways of direct observation dislocation structure formation and quantification underneath the indent using conventional microscopy techniques. A proper way of microstructure investigation was employed aligned with the purpose of this research to study dislocation configuration and plastic zone size below the indents. TKD technique can combat the drawbacks of TEM and gives a better resolution compared to EBSD.

4. Nanoindentation of FCC and BCC Single Crystal Metallic Materials

4.1 Introduction

After establishing the definition of hardness obtained by various methods [83], attempts were made to perform the measurement in scales as small as possible. The early works in the 1970s found out the change in the measured hardness as depth of indenter decreases. Since then, a new field has opened up to perform the indentation testing in small scales on different materials and to comprehend the mechanisms for increasing the hardness. Invention of instrument indentation testing in 1992 was a breakthrough since it made it possible to control applied load and indentation depth accurately. IIT has become ubiquitous research tool and found its way in across variety of engineering and scientific disciplines.

Various studies have been done and are still being done to address the size effect in FCC metallic materials and try to explain this phenomenon through a mechanism-based model. By advancing testing equipment and improvement of their sensitivity in one hand and increase in interest in this field of study on the other hand, the models are being overruled or modified since there is no model which can explain this effect thoroughly in the macro – micro and nanometre length scales. The early works are mainly experimental. Recent simulation works have tried to overcome the barriers of continuum mechanics and have been able to some extend help to give a better understanding.

An early work of Gane and Cox [37] to study the hardness of Gold in annealed and work-hardened conditions in micrometre range showed the existence of the size effect. They could conclude that the work hardening process in small volumes is different than in the bulk. Another pioneering work on silver single crystal revealed the existence of size effect [39].

Works on gold with different crystallographic orientation [8] showed the effect of crystal orientation on yield point and elastic modulus. Additional to effect of crystallographic orientation, indenter shape is another factor which causes a difference in material response in terms of hardness [163].

In comparison with FCC materials, less attention has been paid to BCC materials. Restricted number of slip systems, sample preparation i.e., surface oxidation and thermally activated plasticity are among the reason for limited number of publications in study of size effect in BCC materials.

4.2 Experimental

Specimen were polished mechanically and electropolished to prepare a suitable surface for indentation. Before indentation, the surfaces were checked for acquiring Kikuchi pattern using EBSD and the surface roughness was checked by AFM.

Multi cycle force-controlled loading was employed with a range of applied forces between 1mN to 200mN using Berkovich indenter. The same procedure will be followed for all samples.

Multicycle indentation testing using Berkovich indenter was used which includes applying ten forces at each indentation point on the sample. The force increases by 10% and unloading is done to 50% of previous force. Figures 36 and 37 shows the force vs. time multicycle indentation test performed on copper and vanadium.

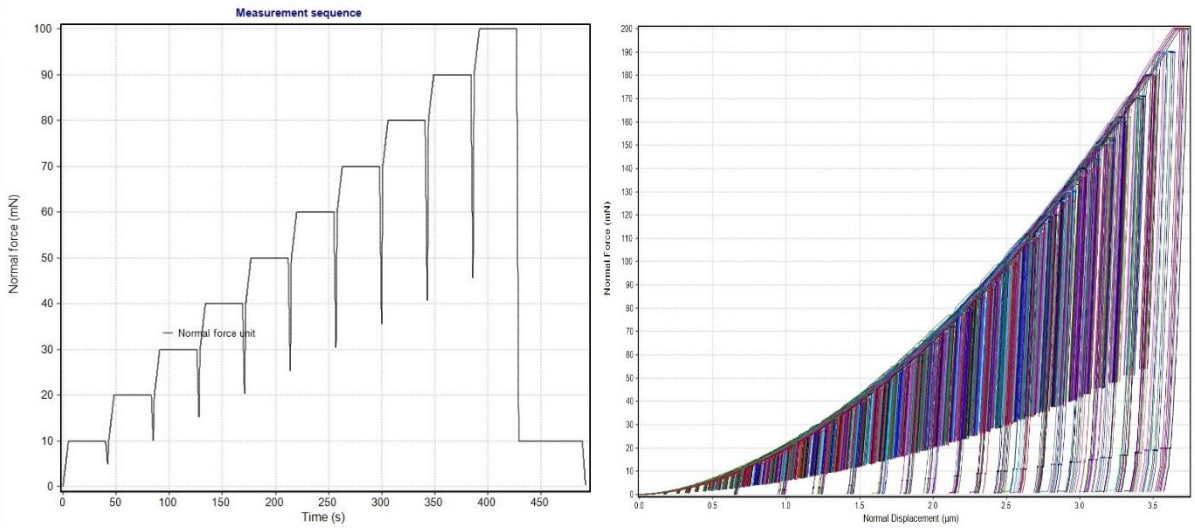

Fig. 36: Measurement sequence and the correspondent load-displacement curve for Cu001. Force-controlled multicycle method with maximum load from 10mN up to 200mN was applied. Force and time are set before testing and the displacement is measured which delivers a Force-displacement (indentation depth) curve as result.

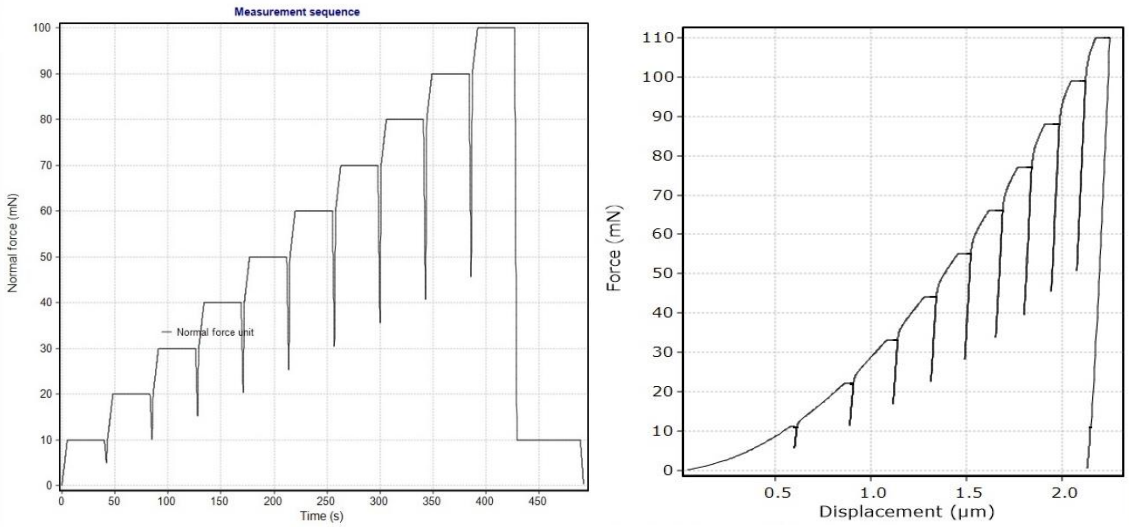

Fig. 37: Measurement sequence and the correspondent load-displacement curve of Vanadium with the maximum applied load of 110mN. Force and time are set before testing and the displacement is measured which delivers a Force-displacement (indentation depth) curve as result.

Tests were performed using 16Hz frequency for data acquisition. In order to keep the force increase rate, the same for all samples, loading curve includes 1 seconds to reach to previous applied force and then 5 seconds to reach the next force step. Holding time is different for different sample regarding their creep behaviour.

A Molecular dynamic study fcc and bcc metals has indicated the relaxation of the dislocation network beneath the indenter when it is held for a while which affects dislocation length and plastic zone size [164]. A specific holding time (creep time) in the measurement sequence was allocated to each sample. Creep rate was measured for specimens, and the point where creep rate becomes linear was chosen as holding time (creep time). Figure 38 shows an example creep rate measurement of FCC (Nickel) and Aluminium materials. Unloading was done in 2 seconds. Final cycle was followed by unloading to 10% of final loading and was kept there for 60 seconds for drift correction. The holding time (creep time) for all the samples has been summarized in Table 5.

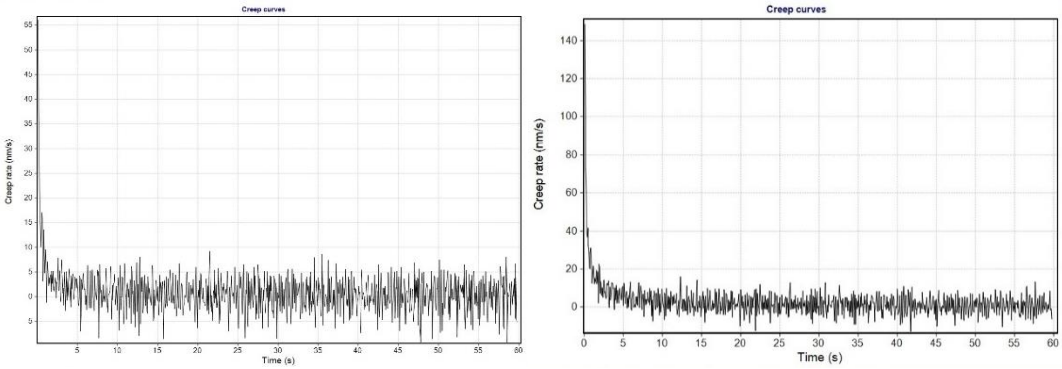

Fig. 38: Holding time based on their creep rate curves for Nickel (left side) and Molybdenum (right side)

Table 5: Holding period of each specimen based on its creep rate.

Sample	Holding time (s)
Al	20
Ni	15
Pt	17
Cu	15
Ag	25
Mo	40
Fe	35
Ta	45
V	35

Multi cycle force-controlled loading was employed with a range of applied forces between 200mN to 1mN using Berkovich indenter. The same procedure will be followed for all samples.

Tests were performed using 16Hz frequency for data acquisition. In order to keep the force increase rate, the same for all samples, loading curve includes 1 seconds to reach to previous applied force and then 5 seconds to reach the next force step. Holding time is different for different sample regarding their creep behaviour.

4.3 Results

4.3.1 Indentation Size Effect Study in FCC Materials:

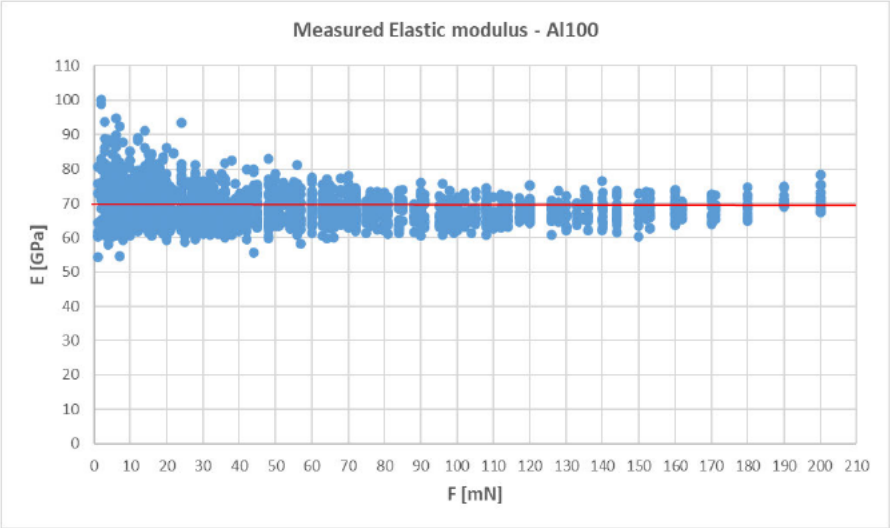

Fig. 39: Elastic modulus obtained from indentation on Al100 using Berkovich indenter.

To begin with analysis of the data, a graph of variation of elastic modulus by force variation has been drawn as shown in figure 39.

It should be noted that regardless of all the efforts to have a fine calibration of the equipment, there is a profound characteristic in every Nanoindentation equipment which does not allow to achieve a perfect linear elastic modulus, specially while trying to cover a long range of depth or force. Because in low range depth/forces, area function and in higher depth/forces frame compliance are precedence factor influencing the data. In spite of that, the measured elastic modulus of the tested materials shows a relatively good linear relationship with force in the collected contact mechanics data without applying any correction.

Afterwards, hardness test results have been drawn for different forces and for indentation depths in order to describe the material response. As it has been illustrated in the graph 40 for aluminium, all materials have shown indentation size effect. It means that unlike continuum mechanics theory, the measured hardness value is not the same in different length scales.

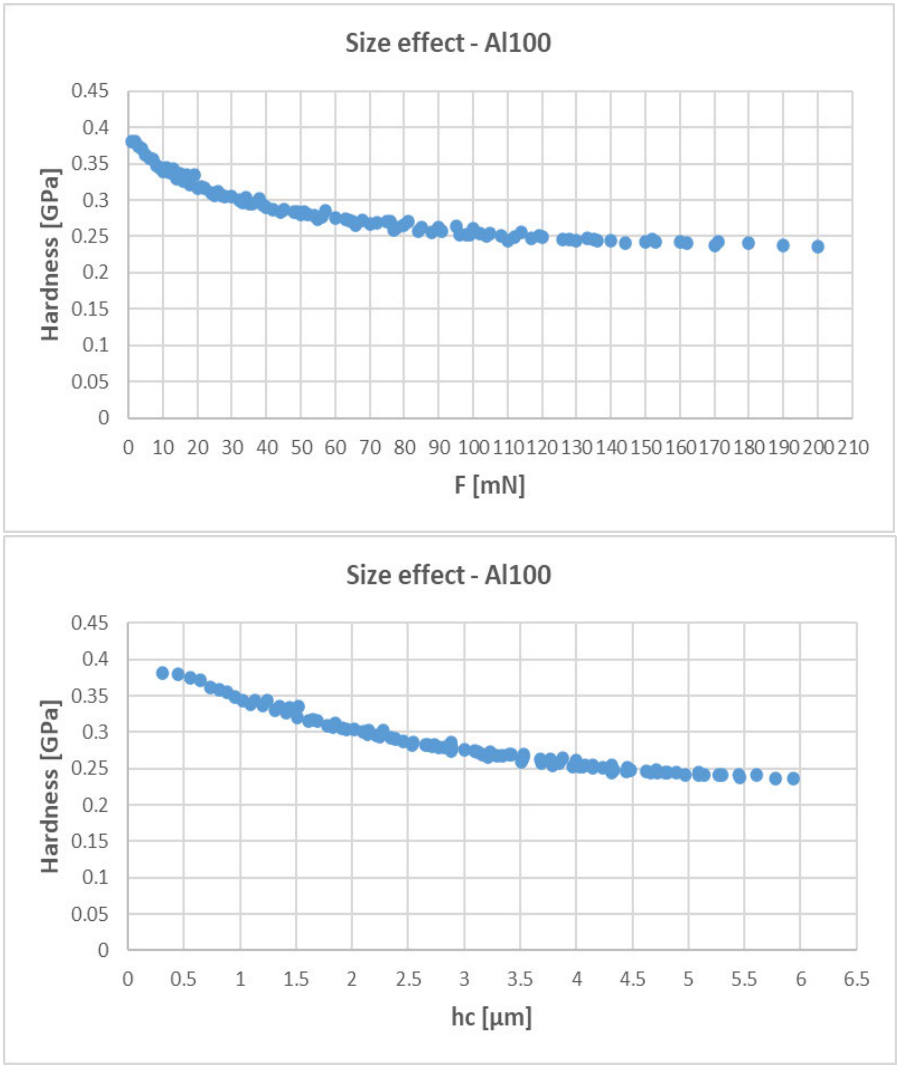

Fig. 40: Indentation size effect illustrates increase of hardness by decreasing force obtained from indentation on Al100 using Berkovich indenter (Image on top), Hardness variation with indentation depth (Image at the bottom)

Similar analysis was done for Nickel100 single crystal as depicted in figure 41 and 42. Elastic modulus is relatively linear though the measured elastic modulus is higher in low depth. The average of all measured points is 219.11 GPa which is in agreement with calculated elastic modulus for Nickel. Size effect is clearly observed by reducing force or indentation depth as per figure 42.

One fact which might have caused the variation in the measured elastic modulus in different depth is the influence of sample preparation, most probably through creating tensile or compressive residual stresses on the surface. The shallow layer of residual stress on the surface is naturally has higher impact on the low depth indents. Also, the depth of created residual stress might be different from sample to sample.

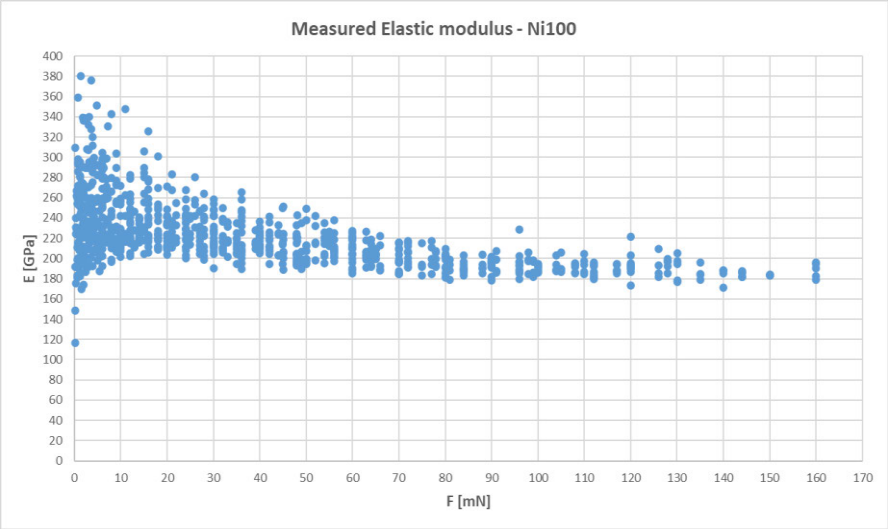

Fig. 41: Elastic modulus obtained from indentation on Ni100 using Berkovich indenter

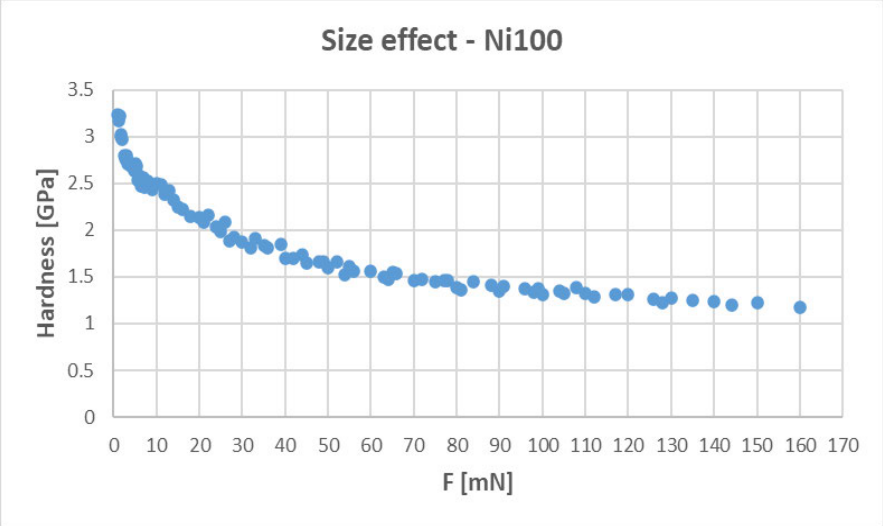

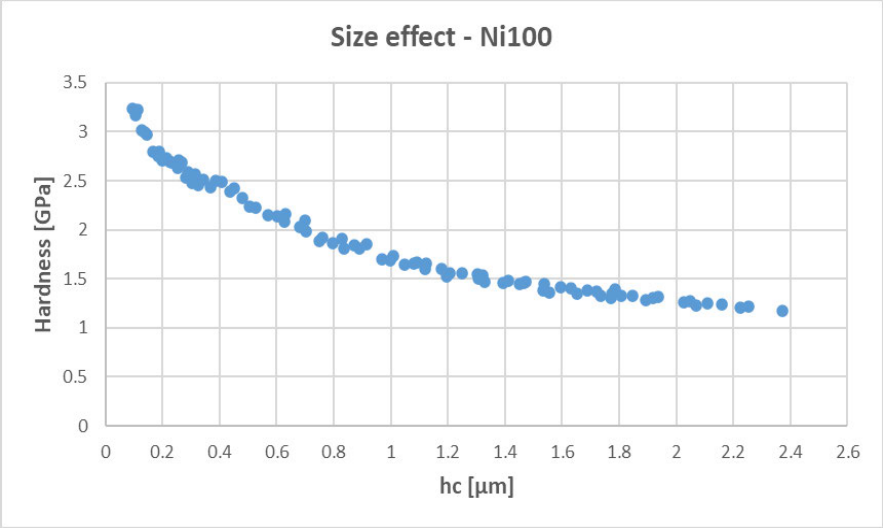

Fig. 42: Indentation size effect illustrates increase of hardness by decreasing force on Ni100 using Berkovich indenter (Image on top), Hardness variation with indentation depth (Image at the bottom)

Nickel has the second highest stacking fault energy in FCC materials among the samples collected for the purpose of this research. Nickel has the highest measured hardness among FCC materials of this research. The result demonstrates a good agreement with other study [52], though the measured hardness is slightly higher for depth below 500µm and this might be due to higher dislocation density to begin with because of sample preparation as well as difference in indentation method since in that work continuous stiffness measurement (CSM) has been used for data collection. Also, pop-in was observed in that study around depth of 20nm, but it was not observed in our work because 20µm is less than the lowest depth in our work.

Cu100, Cu110 and Cu111 were chosen to investigate the influence of crystallographic orientation on material response. Figure 43 to figure 48 indicate the highest values for elastic modulus and hardness obtained from Cu100, Cu110 and Cu111 respectively. Copper has FCC microstructure and planes 111, 110 and 100 have the highest atomic density respectively which explains why the results exhibit highest values for elastic modulus in planes 111, 110 and 100 in order of magnitude.

A slight difference between measured elastic modulus can be seen which comes from the contributions of the various slip systems around the indent gives different responses in properties. Also, the shape and amount of pile-up/sink-in created around indents varies in different orientation [85].

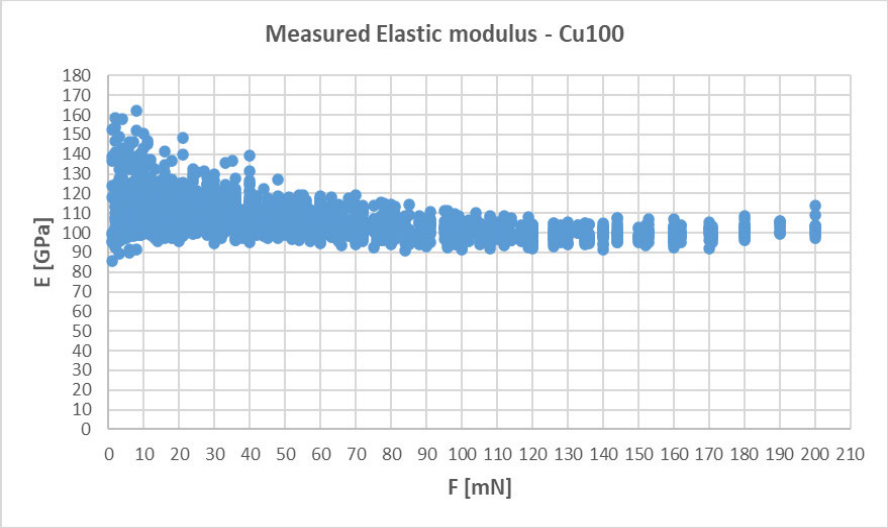

Fig. 43: Elastic modulus obtained from indentation on Cu100 using Berkovich indenter.

Figure 43 shows the test results for indentation on copper 100. Though the tests have been performed in force-controlled mode, the variation in hardness versus change in indentation depth can be drawn as well. Since different materials have a different response at each applied load, a hardness graph regarding indentation depth will help to have a better comparison.

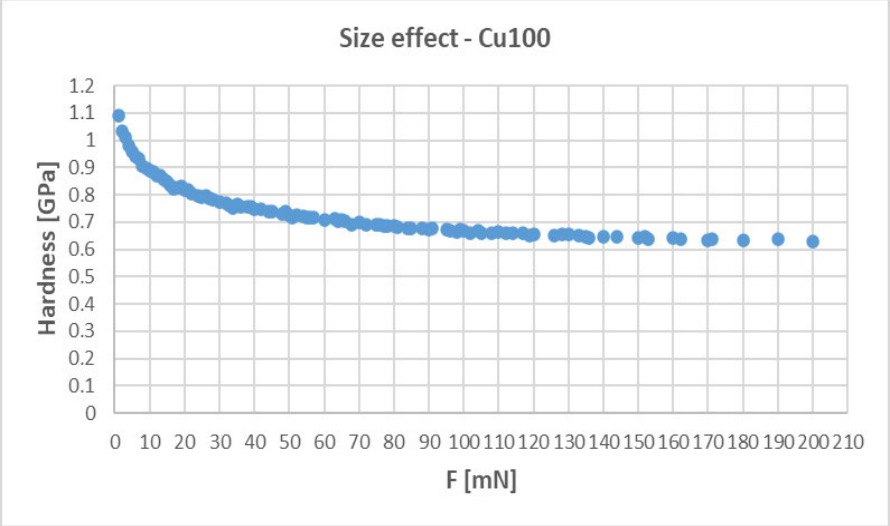

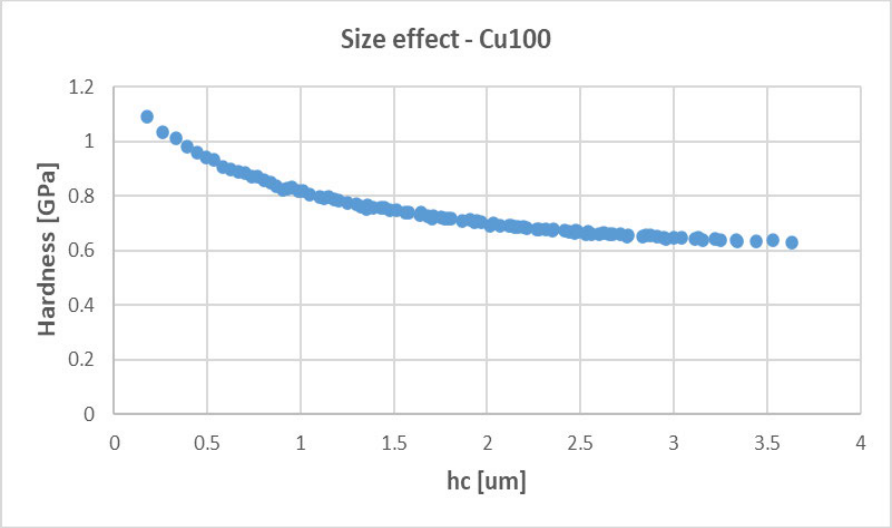

Fig. 44: Indentation size effect illustrates increase of hardness by decreasing force obtained from indentation on Cu100 using Berkovich indenter (Image on top), Hardness variation with indentation depth (Image at the bottom)

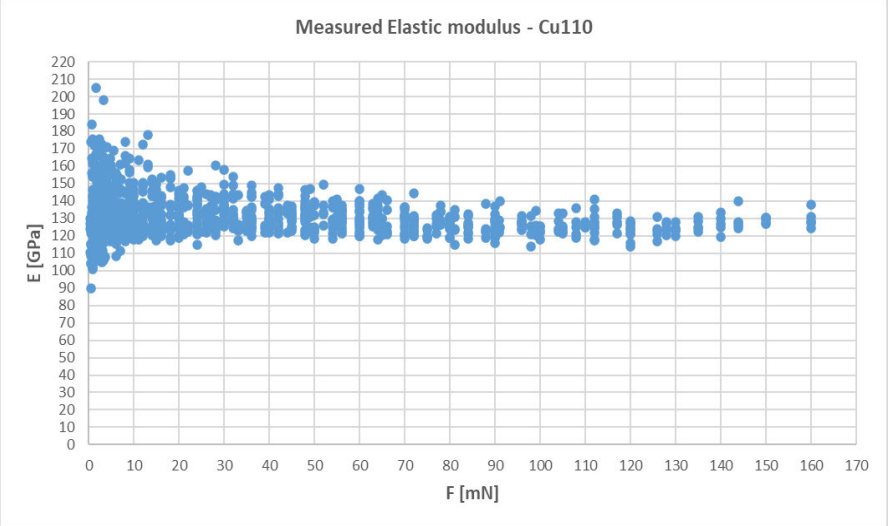

Fig. 45: Elastic modulus obtained from indentation on Cu110 using Berkovich indenter.

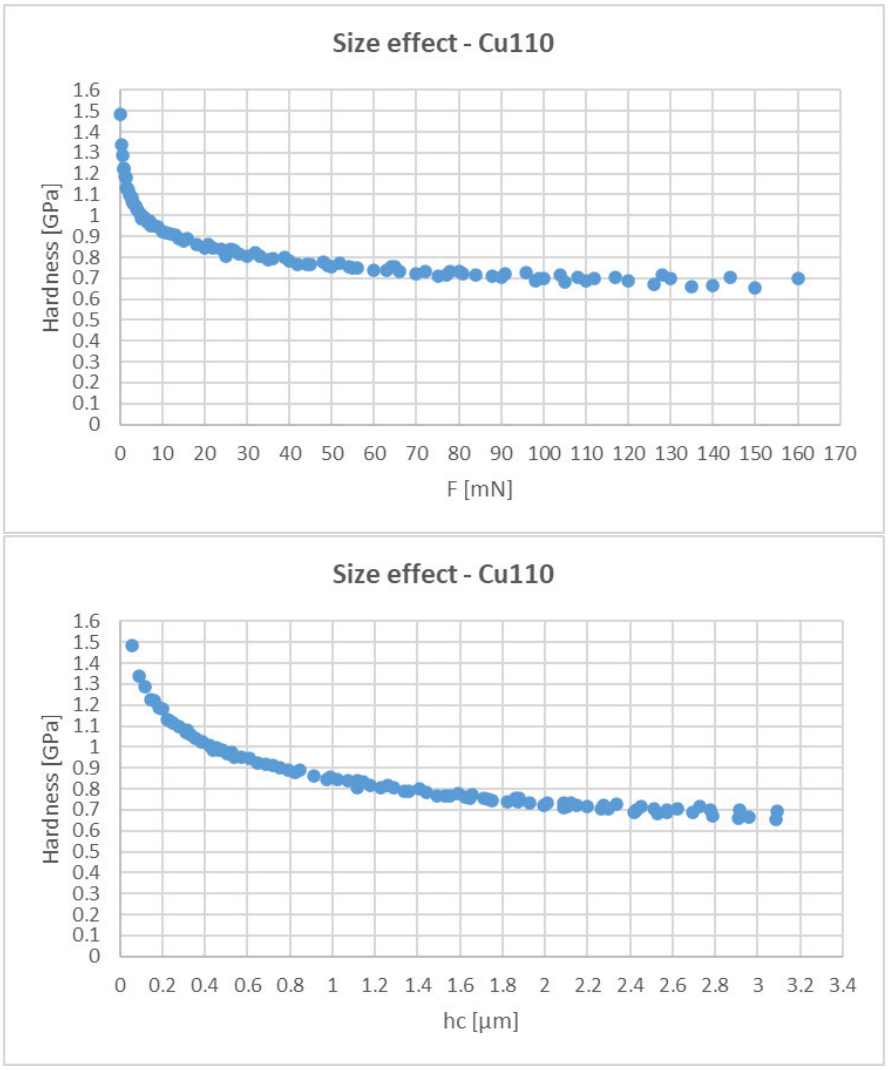

Fig. 46: Indentation size effect illustrates increase of hardness by decreasing force obtained from indentation on Cu110 using Berkovich indenter (Image on top), Hardness variation with indentation depth (Image at the bottom)

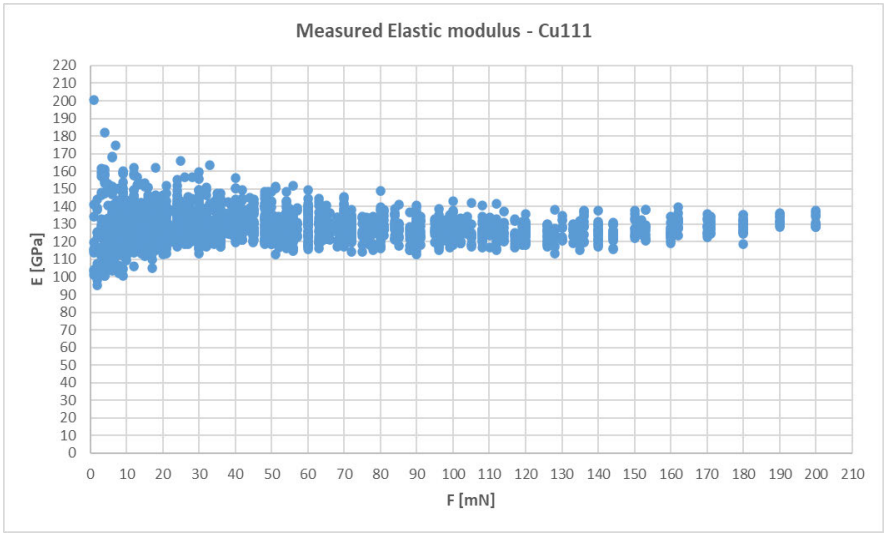

Fig. 47: Elastic modulus obtained from indentation on Cu111 using Berkovich indenter.

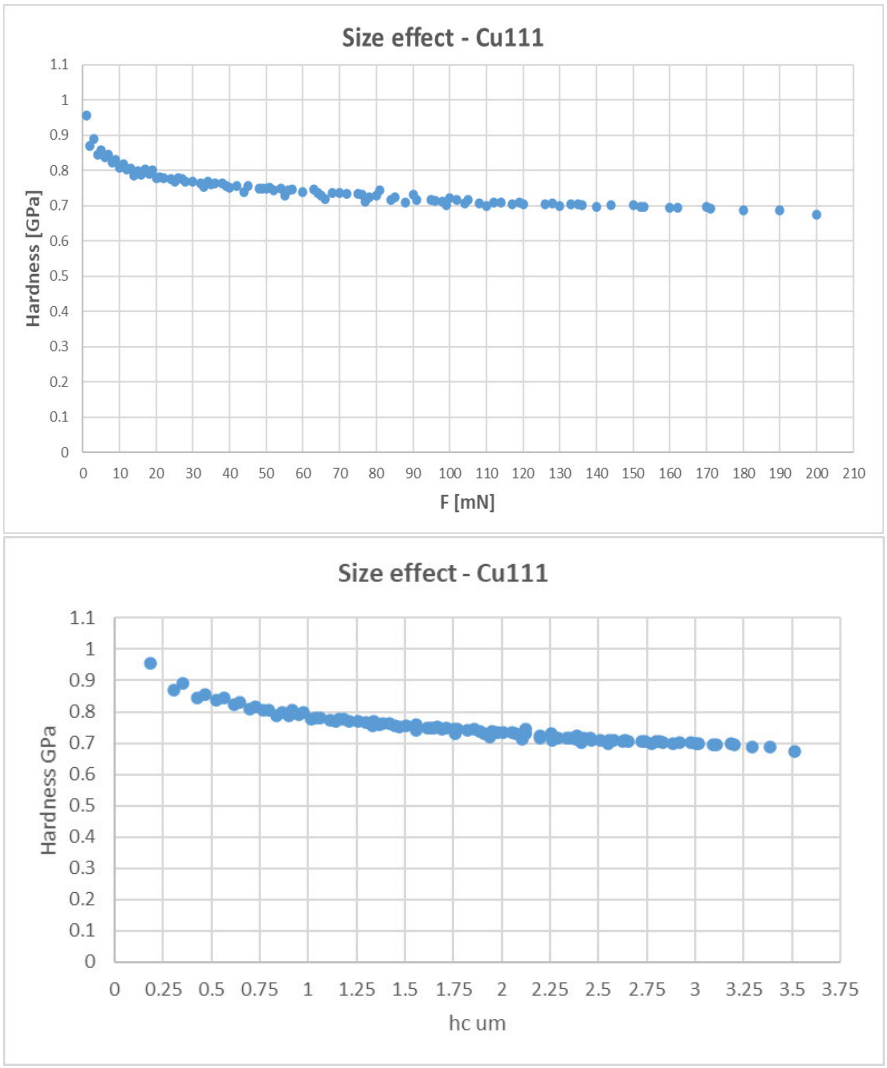

Fig. 48: Indentation size effect illustrates increase of hardness by decreasing force on Cu111 using Berkovich indenter (Image on top), Hardness variation with indentation depth (Image at the bottom)

The highest hardness achieved through indentation on 111 planes are lower than other two planes. On the other hand, the average of hardness in forces above 50mN exhibit slightly higher amount for Cu111.

The average elastic modulus measured for Cu100, Cu110 and Cu111 are 107.4 GPa, 124.9 GPa and 128.5 GPa respectively which indicates the highest elastic modulus obtained in the highest dense surface. The same trend of having different measured elastic modulus has been observed in different surface orientations in other studies for Au, Cu and Al as well [8][165][166].

It is already well known from uniaxial studies that activities of slip systems strongly depend on the orientation with respect to the loading direction [167] [93] as it is expected from copper to exhibit different response for different slip systems to be activated based on crystallographic orientation.

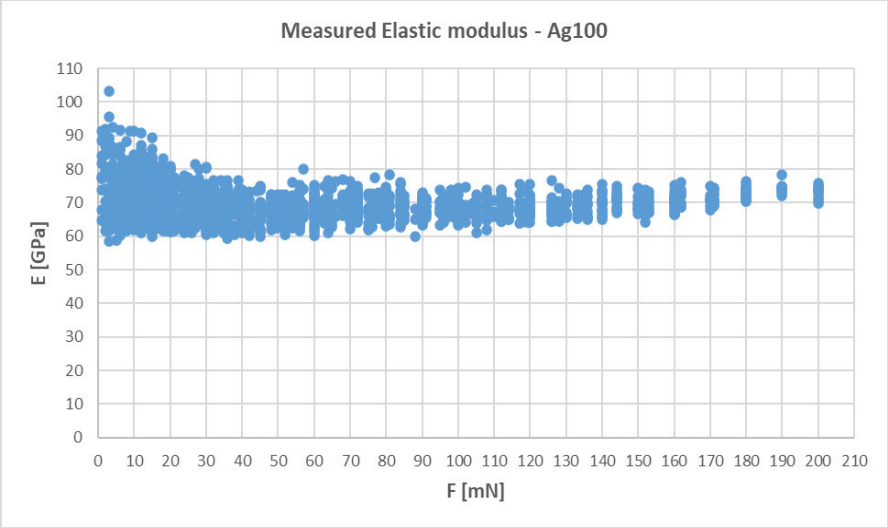

Fig. 49: Elastic modulus obtained from indentation on Ag100 using Berkovich indenter

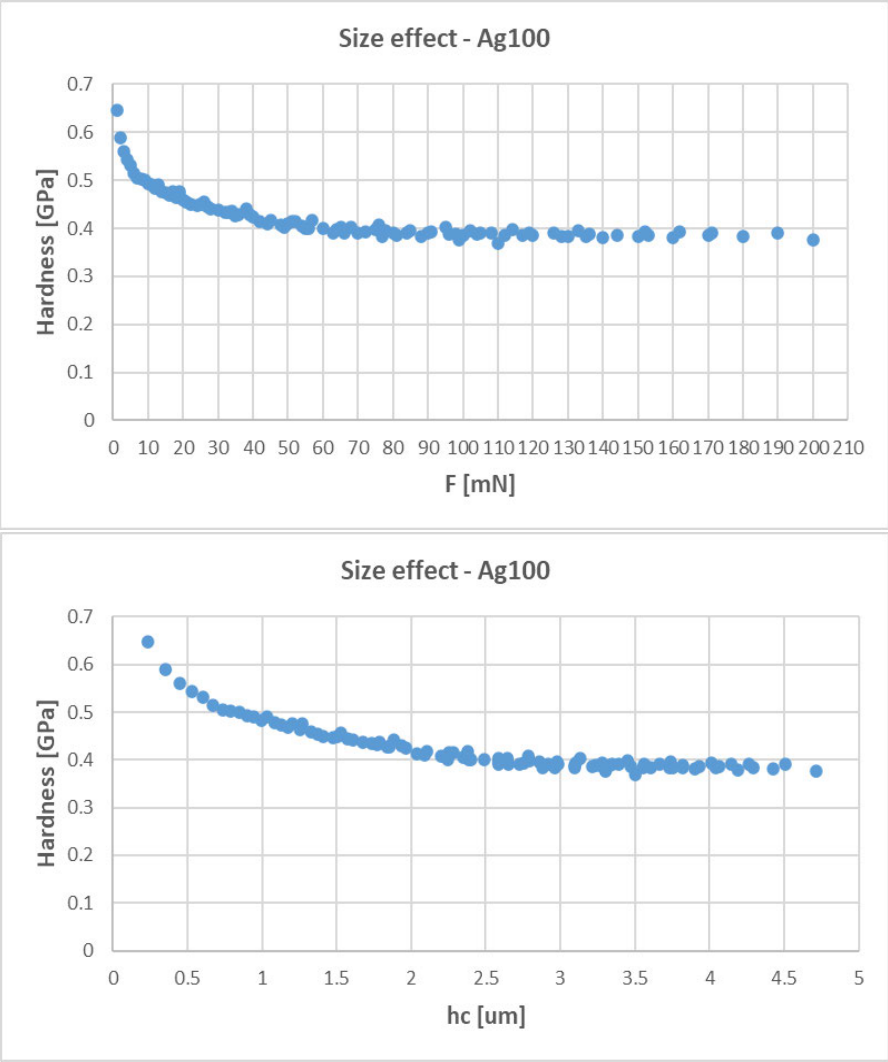

Fig. 50: Indentation size effect illustrates increase of hardness by decreasing force obtained from indentation on Ag100 using Berkovich indenter (Image on top), Hardness variation with indentation depth (Image at the bottom)

Table 6: Far field hardness and elastic modulus for fcc materials

Materials and measured parameters	Cu001	Cu110	Cu111	Al001	Ni001	Ag001
Far field Hardness [GPa]	0.6361	0.6760	0.6573	0.2395	1.1972	0.3852
Standard deviation	0.0074	0.0096	0.0142	0.0044	0.0259	0.0065
Far field Elastic modulus [GPa]	100.8206	129.26	127.815	69.330	185.7366	72.078
Standard deviation	3.3384	4.280	4.712	2.549	3.5551	1.9581

Table 6 represents the far field measured hardness and elastic modulus values for fcc materials.

Compared to other tested FCC materials in this study, the rise in hardness begins from a lower depth (lower force) in Silver as indicated in figure 50. Other FCC materials show a tendency to hardness increase almost from the highest applied force, though the increase is very small.

The measured hardness values for Ag001 are consistent with the work of Clarke and Ma [39]. In another study [168], size effect has been observed in silver with a softening region between 100nm and 50nm and then followed by a sharp increase in hardness. The softening region was not observed in this study.

Graph 51 shows the summary of indentation size effect and a comparison between different FCC samples.

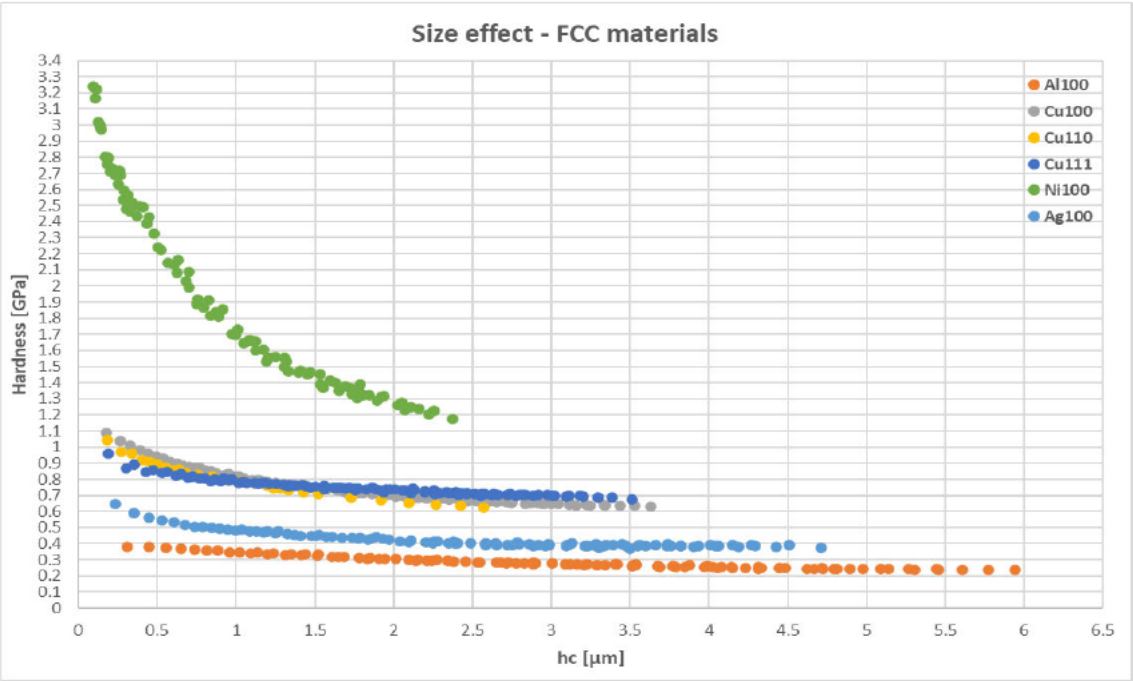

Fig. 51: Indentation size effect obtained from indentation using Berkovich indenter on FCC samples.

It is observed that Ni100 has the highest hardness among tested FCC materials and shows a high size effect tendency. Al100 shows the lowest hardness with a smooth tendency to hardness increase. The same behaviour has been observed in other investigation [169]. Above 1µm, Cu111, Cu100 and Cu110 have the highest to lowest hardness, however, in micrometre range this trend changes and Cu100, Cu110 and Cu111 show the highest to lowest hardness respectively.

Experimental indentation testing on Copper and Aluminium shows displacement bursts or so called pop-in behaviour which is linked to collective dislocation nucleation [166]. This phenomenon was not observed in the indentation of FCC materials in this study. The reason might be due to the difference in indentation depth since the bursts are observed around 20nm indentation depth.

In another comparison, all measured hardness of the materials were divided by far field hardness values where the measured hardness does not show size effect as shown in figure 52. That way of comparison changes the narrative for the FCC materials since they indicate a very similar behaviour and very close hardness values except for Ni which shows a sharp rise. Al100 has a continuous hardness increase by reducing indentation depth instead of a sharp increase in hardness.

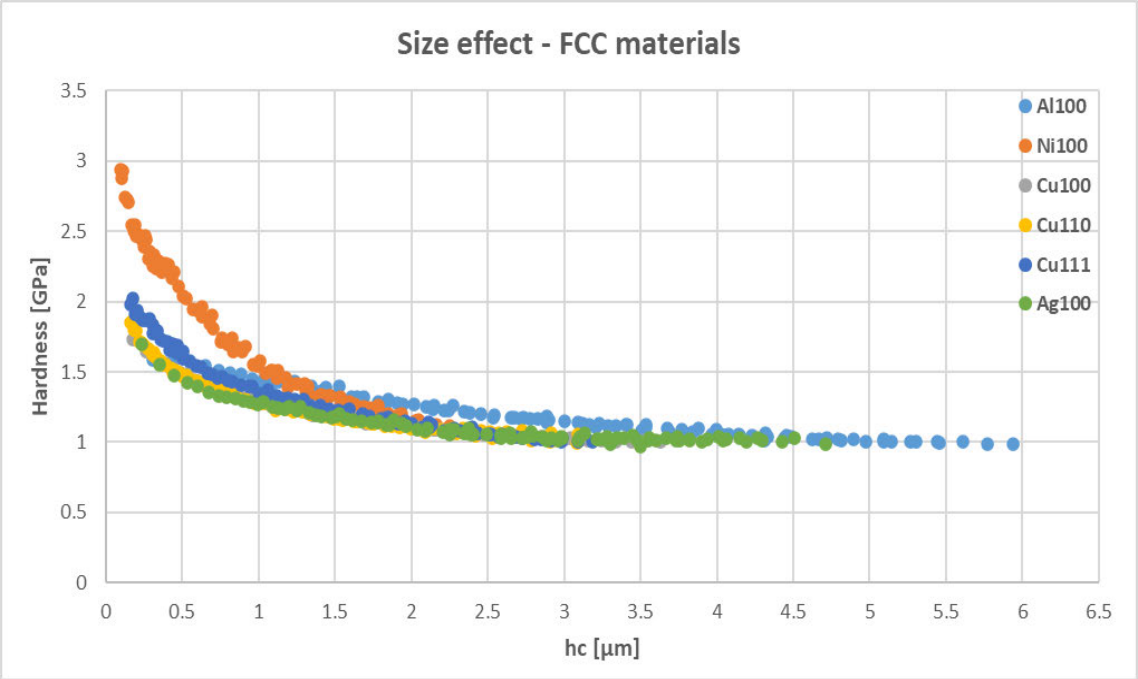

Fig. 52: Indentation size effect obtained from indentation on FCC samples after normalizing by far field hardness value for each sample.

4.3.2 Indentation Size Effect Study in BCC Materials:

To begin with analysis of the data, a graph of variation of elastic modulus by force variation has been drawn.

It should be noted that regardless of all the efforts to have a fine calibration of the equipment, there is a profound characteristic in every Nanoindentation equipment which does not allow to achieve a perfect linear elastic modulus, specially while trying to cover a long range of depth or force. Because in low range depth/forces, area function and in higher depth/forces frame compliance are precedence factor influencing the data. In spite of that, the measured elastic modulus of the tested materials shows a relatively good linear relationship with force in the collected contact mechanics data without applying any correction.

Afterwards, hardness test results have been drawn for different forces and for indentation depths in order to describe the material response. As it has been illustrated in the graphs, all BCC materials have shown indentation size effect. It means that unlike continuum mechanics theory, the hardness is not the same in different length scales.

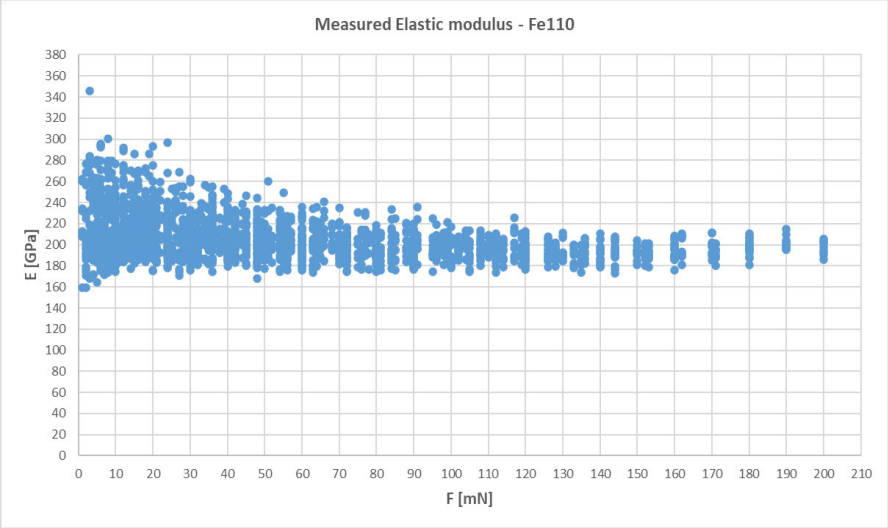

Fig. 53: Elastic modulus obtained from indentation on Fe110 using Berkovich indenter.

As illustrated in figure 53, elastic modulus is relatively linear though the measured elastic modulus is slightly higher in low depth. The average of all measured points is 205.6 GPa which is in good agreement with calculated elastic modulus for Iron. Having a linear response for elastic modulus throughout the measurement is a sign of proper calibration in terms of area function and frame compliance as well as quality of sample preparation.

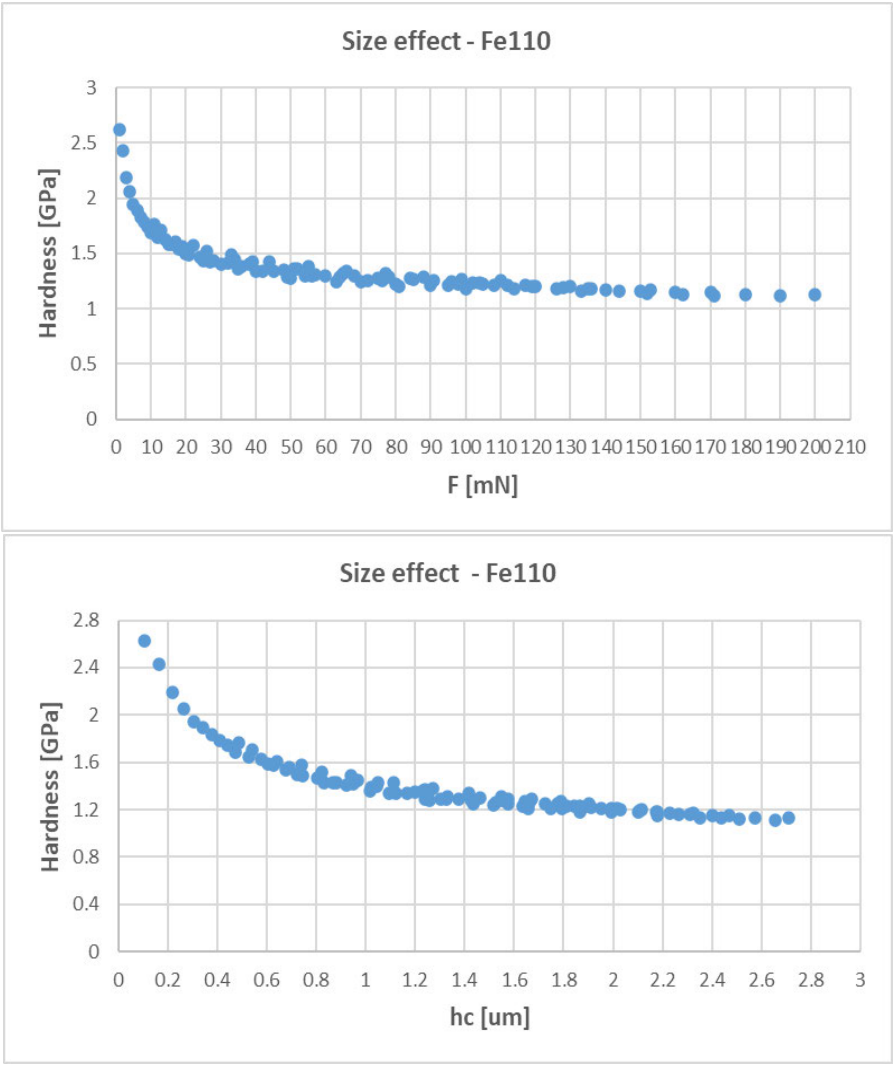

Fig. 54: Indentation size effect illustrates increase of hardness by decreasing force obtained from indentation on Fe110 using Berkovich indenter (Image on top), Hardness variation with indentation depth (Image at the bottom)

The rise in the hardness by reducing force or indentation depth as illustrated in figure 54, appears from the very beginning. The slope of the hardness increases by reducing the force, especially around 500µm and lower depth, a sharp rise in hardness is observed.

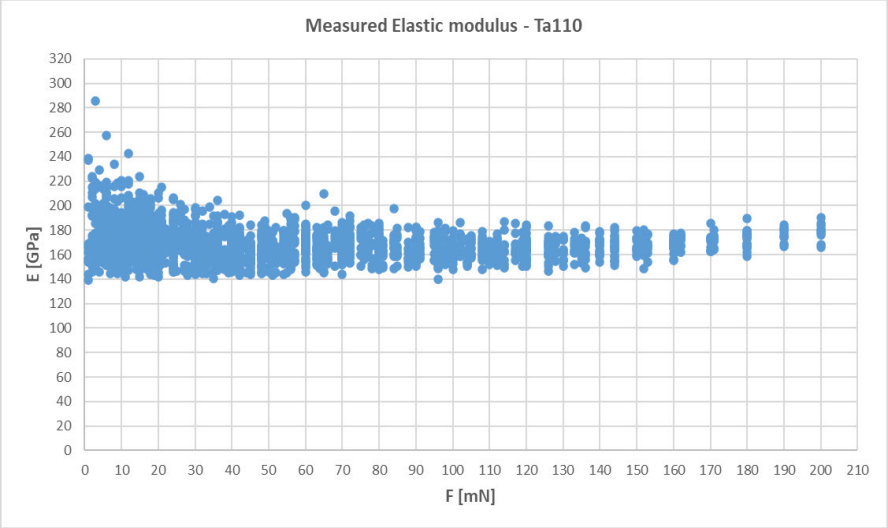

Fig. 55: Elastic modulus obtained from indentation on Ta100 using Berkovich indenter.

A linear trend in the measured elastic modulus of Tantalum is observed as shown in figure 55. Measure hardness shows a continuous increase in hardness by decreasing the force. Hardness rises faster in force less than 50mN and followed by a sharper rise in hardness for forces 10mN and smaller as the data in figure 56 indicates.

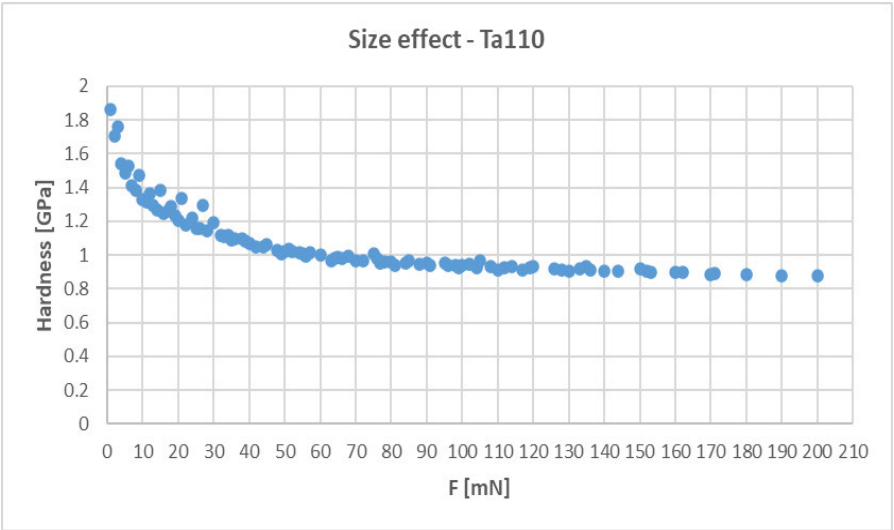

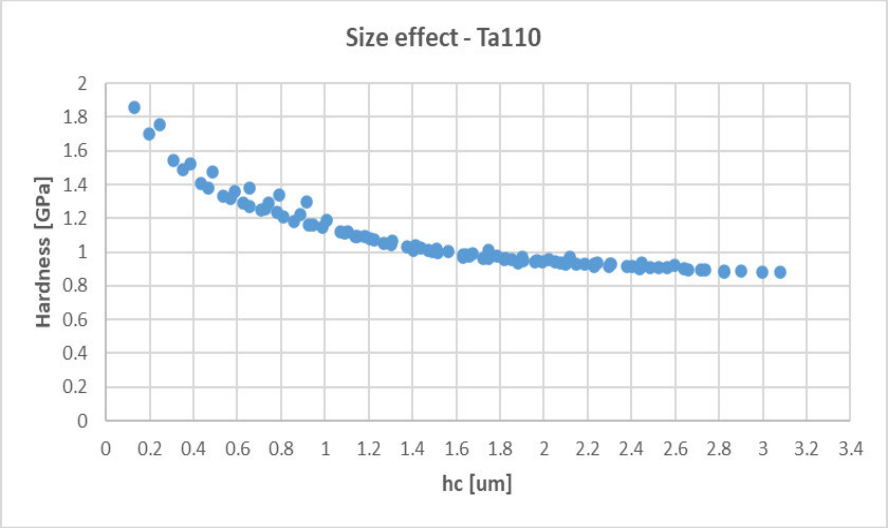

Fig. 56: Indentation size effect illustrates increase of hardness by decreasing force obtained from indentation on Ta100 using Berkovich indenter (Image on top), Hardness variation with indentation depth (Image at the bottom)

As shown in figure 57, measured elastic modulus of Molybdenum has a linear trend though the slight change in the measured elastic modulus due to the competitive effects of frame compliance and area function and surface residual stress might be accountable for that. Observation of the measured hardness shown in figure 58 displays a near linear hardness for the indents between 200mN and 80mN in Molybdenum. From 80mN hardness starts to rise and this trend is intensifying by force reduction.

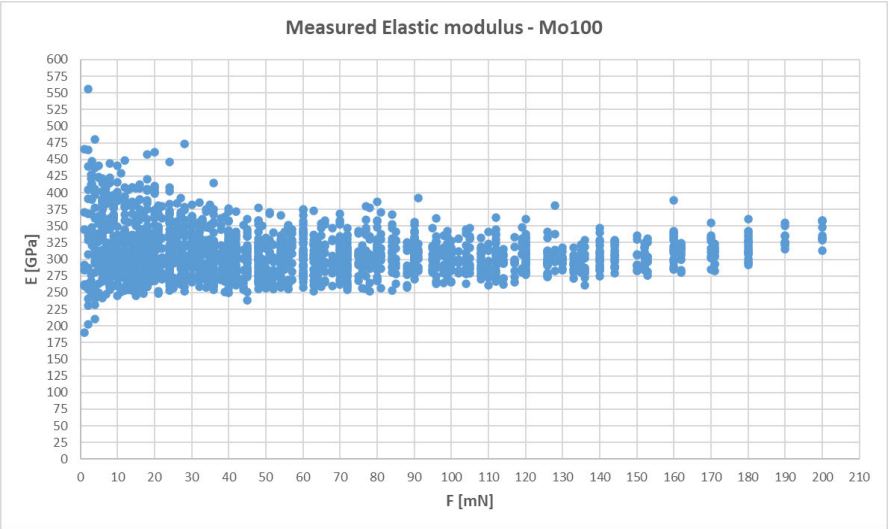

Fig. 57: Elastic modulus obtained from indentation on Mo100 using Berkovich indenter

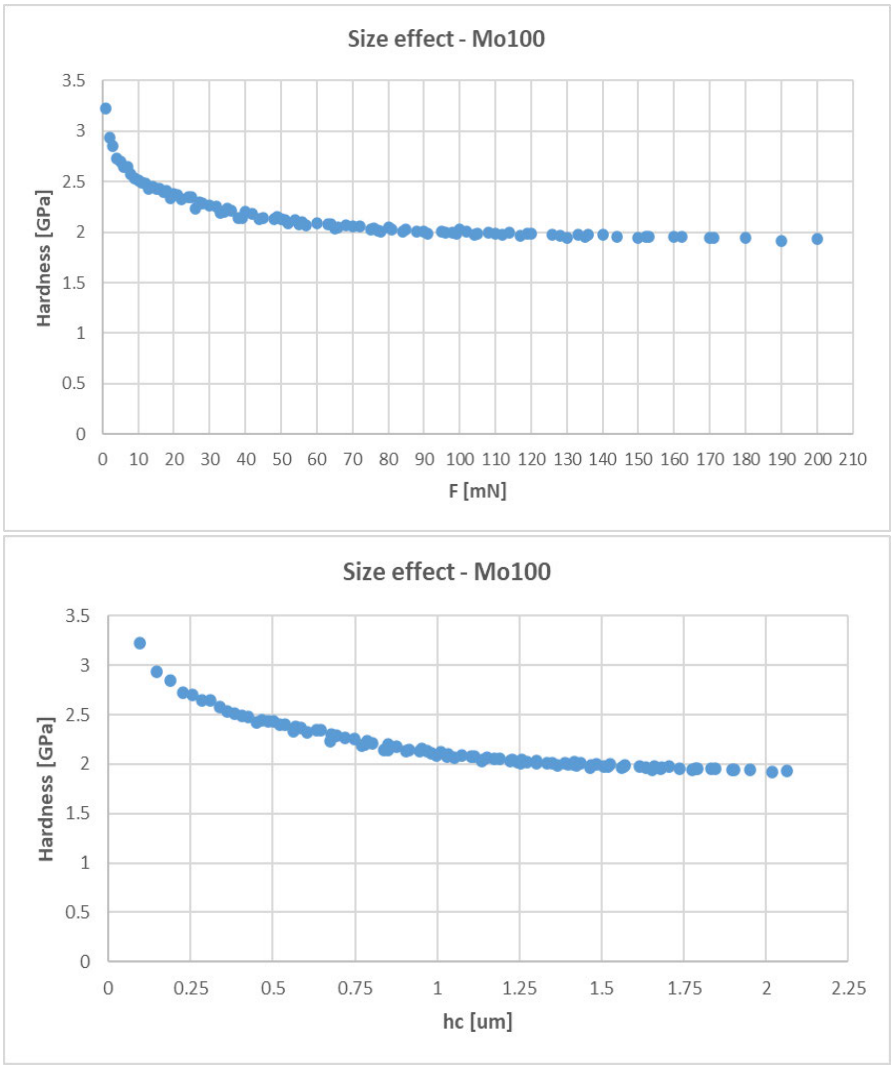

Fig. 58: Indentation size effect illustrates increase of hardness by decreasing force obtained from indentation on Mo100 using Berkovich indenter (Image on top), Hardness variation with indentation depth (Image at the bottom)

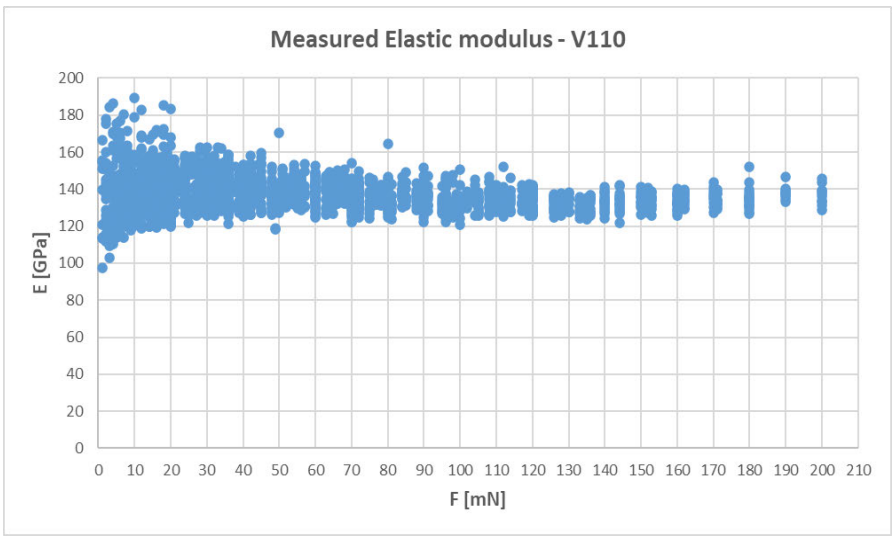

Fig. 59: Elastic modulus obtained from indentation on V110 using Berkovich indenter

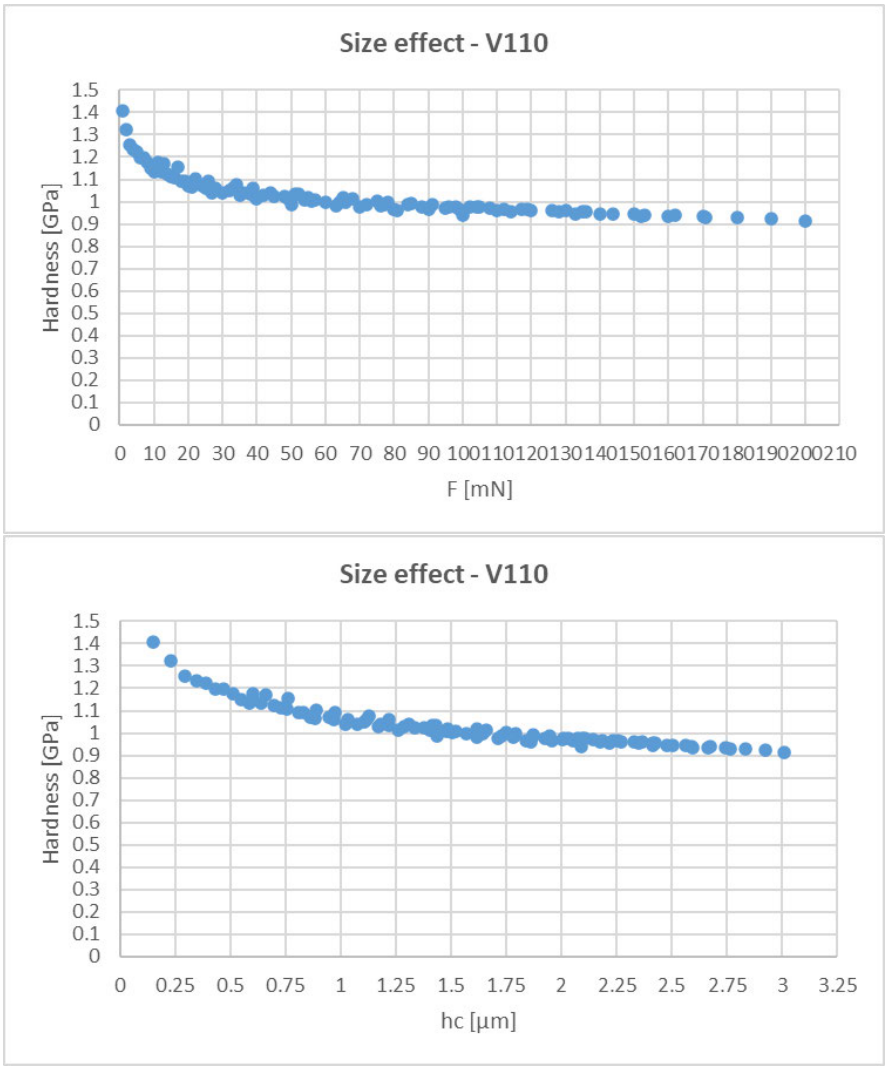

Fig. 60: Indentation size effect illustrates increase of hardness by decreasing force obtained from indentation on V110 using Berkovich indenter (Image on top), Hardness variation with indentation depth (Image at the bottom)

Measured elastic modulus of Vanadium has a linear characteristic at different indentation depth as per depicted data in figure 59 and size effect characteristic in the measured hardness the same as other materials is observed as well as illustrated in figure 60.

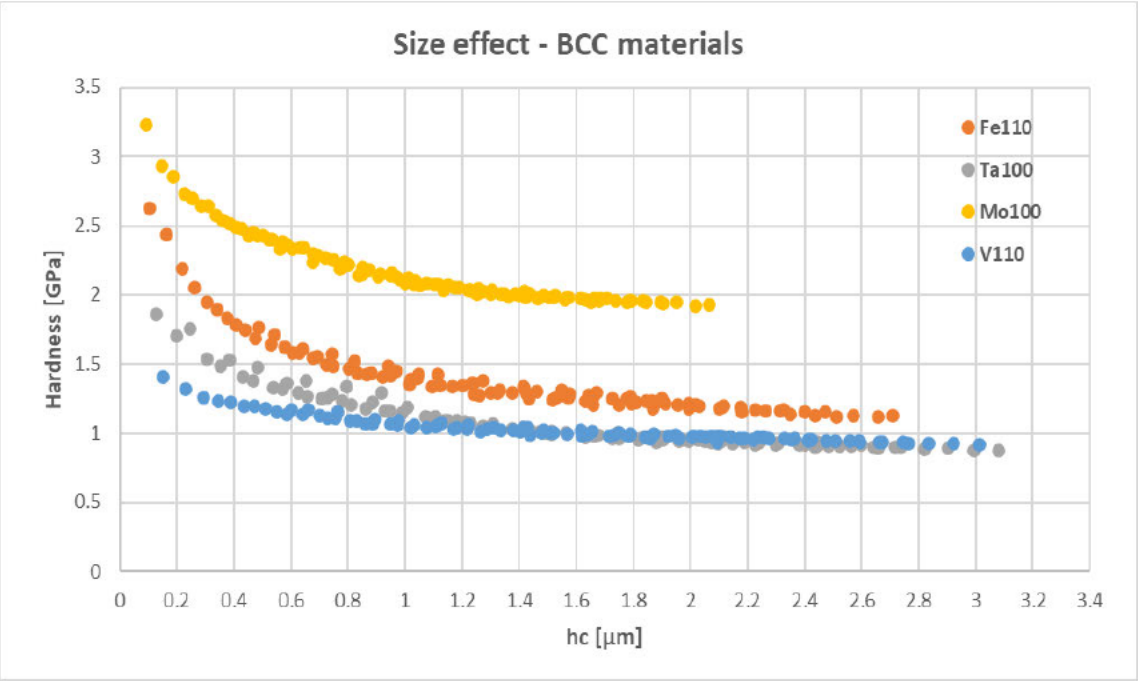

Fig. 61: Indentation size effect obtained from indentation on BCC samples.

Vanadium and Tantalum show similar hardness values in micro region. Tantalum and Vanadium hardness start rising around 1.25µm and 1 µm respectively, with Tantalum showing a steeper increase in hardness. In contrast, Hardness of Iron indicates a hardness increase throughout the measurement with a sharp hardness increase for the depth below 500nm.

Voyiadjis et al [170] have found three regions of hardness in their study. They indented four BCC metals using Berkovich indenter with continuous stiffness measurement (CSM) procedure in micro and nano regions and found a region (region II) which showed softening behaviour. That phenomenon is not observed in this work, as shown in picture 61. They relate this effect to grain boundaries since their samples are polycrystals unlike the sample used in this study.

Nanoindentation testing of BCC material of Nb, W and Mo [171] shows the same ISE behaviour as in this study. The measured hardness values for Mo are in a good agreement with our results.

Table 7: Far field hardness and elastic modulus for bcc materials

Materials and measured parameters	Fe110	Ta100	Mo100	V110
Far field Hardness [GPa]	1.1323	0.8872	1.9406	0.9289
Standard deviation	0.0321	0.0050	0.0235	0.0125
Far field Elastic modulus [GPa]	196.90	172.7757	320.3486	135.2743
Standard deviation	7.730	6.1757	16.9743	4.3229

All measured hardness of the materials were divided by far field hardness values where the measured hardness does not show size effect as shown in figure 62. That way of comparison changes the narrative for the BCC materials since the Mo is not hardest anymore and Fe shows the highest rise in hardness and Mo and V are almost identical. Fe and Ta are very similar as well.

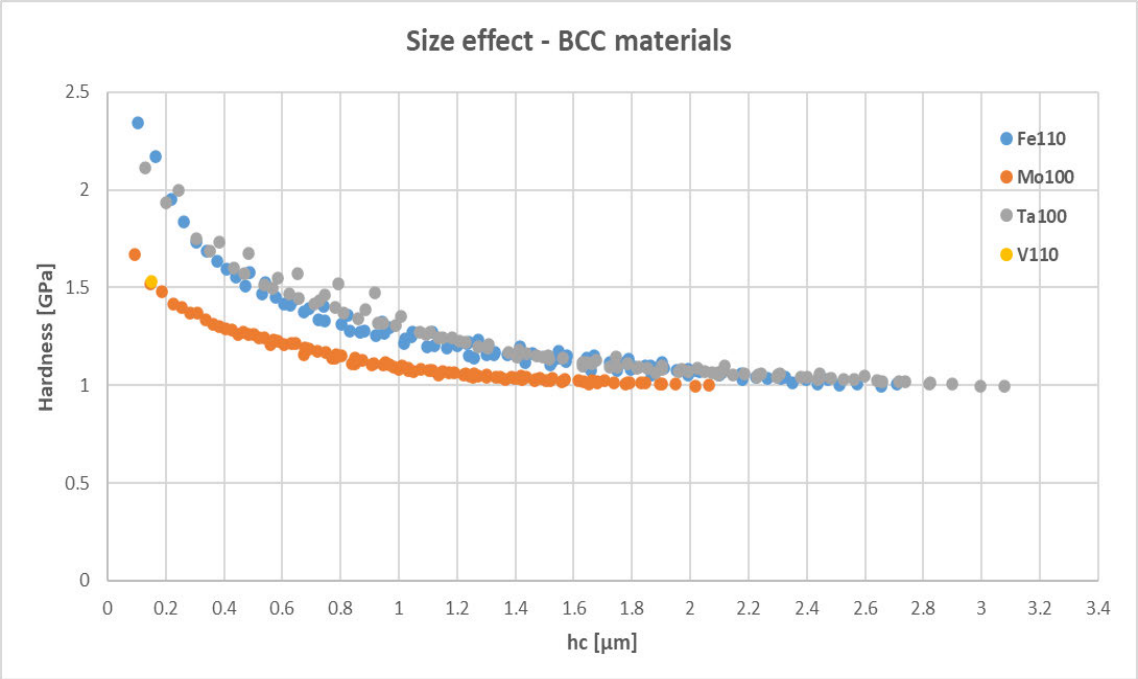

Fig. 62: Indentation size effect obtained from indentation on FCC samples after normalizing by far field hardness value for each sample.

4.4 Discussion

4.4.1 Plasticity Mechanisms and Length Scale Size effect in FCC Materials:

Based on Hou and Jennett equation [1], the graph was drawn for each sample in order to obtain K_1 and $K_3\sqrt{\rho_s}$ parameter from test results for FCC samples.

Since the samples are single crystals, there is no grain boundary which can contribute to hardness whether as a blockage to dislocation movement or as a source for dislocation generation, the d parameter in the equation is going to be infinity which makes $\frac{K_2}{d}$ to be zero and can be eliminated from the equation. Therefore, from each graph, K_1 and $K_3\sqrt{\rho_s}$, which are first and third terms in equation that contribute to hardness, can be found using a least square fit function.

Equation 3-1

$$\left(P_m - P_y\right)^2 = \frac{K_1}{a} + \frac{K_2}{d} + K_3\sqrt{\rho_s}$$

$(P_m - P_y)^2$ is plotted against $\frac{1}{a}$ for all samples. K_1 will be the gradient of the fitting function and $K_3\sqrt{\rho_s}$ will be interception of the fitting function. Larger K_1 indicates a smaller plastic zone under indent and larger $K_3\sqrt{\rho_s}$ states higher dislocation density inside the deformation-induced zone.

The averaged data was used to find K_1 by obtaining the gradient of the linear regression $(P_m - P_y)^2$ vs 1/a.

Tabor has devised a basic equation for all indentation measurement by reasoning that that nearly two-thirds of the mean pressure of contact manifests as a hydrostatic pressure. This hydrostatic pressure doesn't actively contribute to inducing plastic flow in the material; the remained one-third acts effectively for initiating plastic flow. Consequently, if P is the mean pressure between the indenter and the indentation $P_y /3 \approx \sigma_y$. Therefore, Yield strength was used to calculate P_y by using the Tabor equation [83]:

Equation 3-2 $$P_y \approx 3 \times \sigma_y$$

Obtaining K_1 and $K_3\sqrt{\rho_s}$ from the graphs and based on slip-distance theory and using Hou & Jennett model, plastic zone size and average dislocation spacing have been calculated.

As it can be seen, the graph is not linear unlike what was expected based on the data and the results presented by Hou and Jennett [1]. The reason found to be the difference in the range which was chosen for the applied forces which results in difference in depth and consequently difference in length scales. The data in this study has been collected in a wider range in comparison with the mentioned study which was covering 3mN to 80mN force. By the way, a change in the slope of the graph is visible in the figure 3 of that study for the higher depth/forces.

Due to non-linear behaviour of the curve, the obtained K_1 and $K_3\sqrt{\rho_s}$ by fitting a curve to all data cannot accurately represent the material response. Non-linear behaviour of graph is attributed to change in governing mechanisms in different depth ranges. Therefore, it was decided to divide the graph into the regions which show linear behaviour, and a linear function can be fitted to the data with a good R-squared.

Each graph shows three regions in which the slope of the curve changes which figured out to be the characteristic response of FCC materials. Therefore, the curve was divided in three zones, and obtain K_1 and $K_3\sqrt{\rho_s}$ parameters were obtained in each zone.

Figure 63 clearly indicates the change in the slope of the curve and three linear functions which have been tried to be fitted to the curve for indentation test result of Cu100.

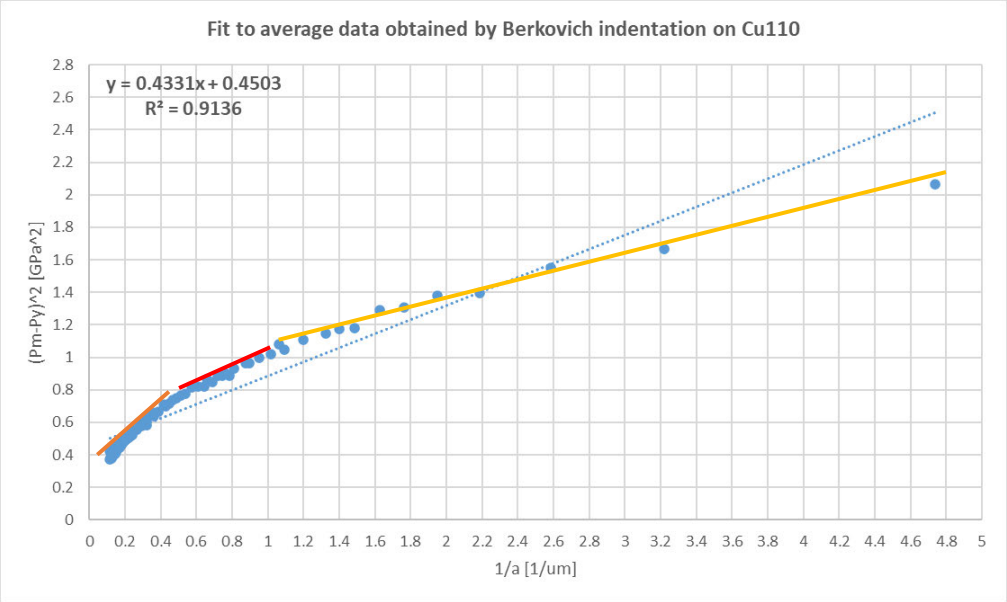

Fig. 63: Fitting function to data from indentation on Cu110 using Berkovich indenter.

To enable precise investigation of each section of the above curve, the fitted linear function to data of each section are presented as below:

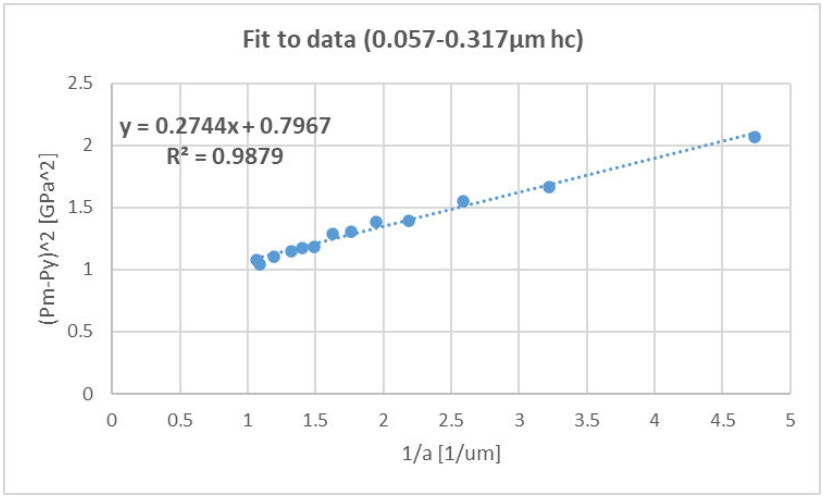

Fig. 64: Fitted liner function to data with indentation depth between

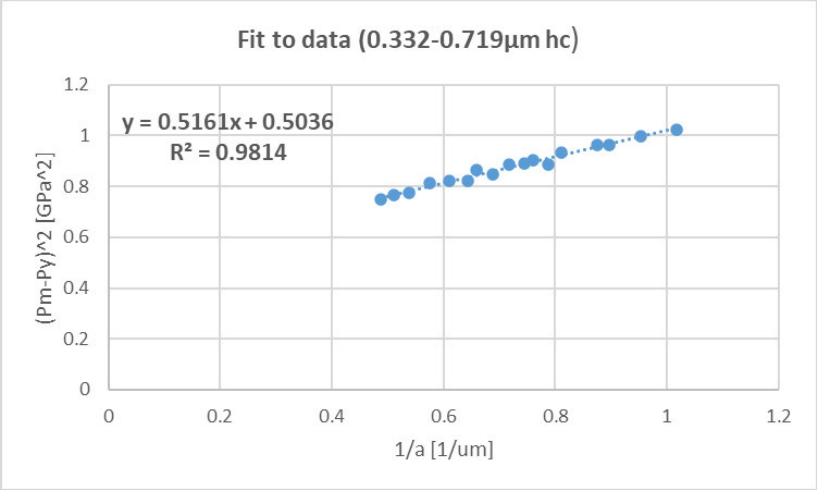

Fig. 65: Fitted liner function to data with indentation depth between

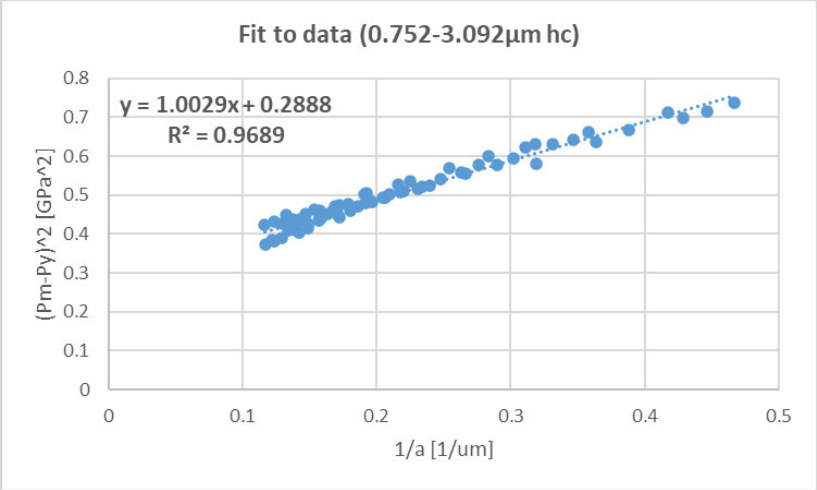

Fig. 66: Fitted liner function to data with indentation depth between

The regions were divided in a way to preserve the linearity of each region as much as possible and achieve a high R-squared. For Copper with 110 orientation, the first change in the slope of the curve is seen in 0.3µm and followed by another change in the slope in 0.7µm. Figures 64 to 66 show the exact amount of each constant and R-squared for the fitted functions. A comparison between the constants of the fitted function to each slope shows a trend. By increasing indentation depth, slope of the curve decreases and intersection constant increases. Those constants are indication for change in the plastic zone size and pinning effect which in this case since the specimens are pure single crystals, that constant can be representative of dislocation density.

For all FCC materials, the same approach has been taken and three fitting curves have been fitted to the data and marked on the graph.

Additional to K_1 and $K_3\sqrt{\rho_s}$ which have been written next to linear fitting function of each region, K_1 and $K_3\sqrt{\rho_s}$ of the linear function fitted to the whole data has been extracted and written next to it

since fitting a linear function to the whole data was the first approach to analyse the collected data. The R-squared has been added for each fitting function as well which is interpretation of how well the regression model fits the observed data.

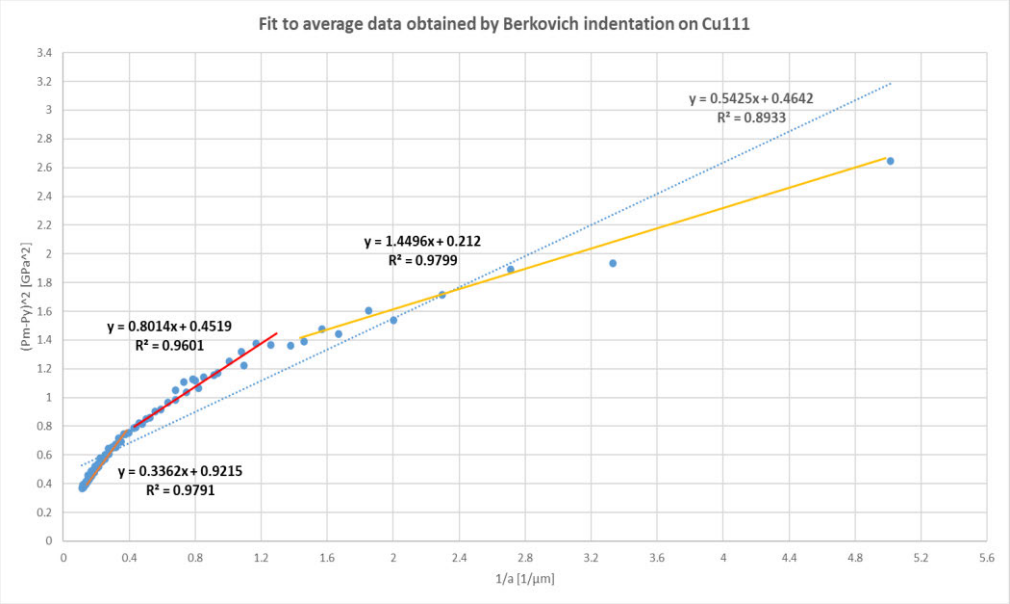

Fig. 67: Fit function to data from indentation on Cu111 using Berkovich indenter.

Copper111 undergoes the first change in the slope of the curve in 0.5µm and followed by another change in the slope in 1.6µm as illustrated in figure 67.

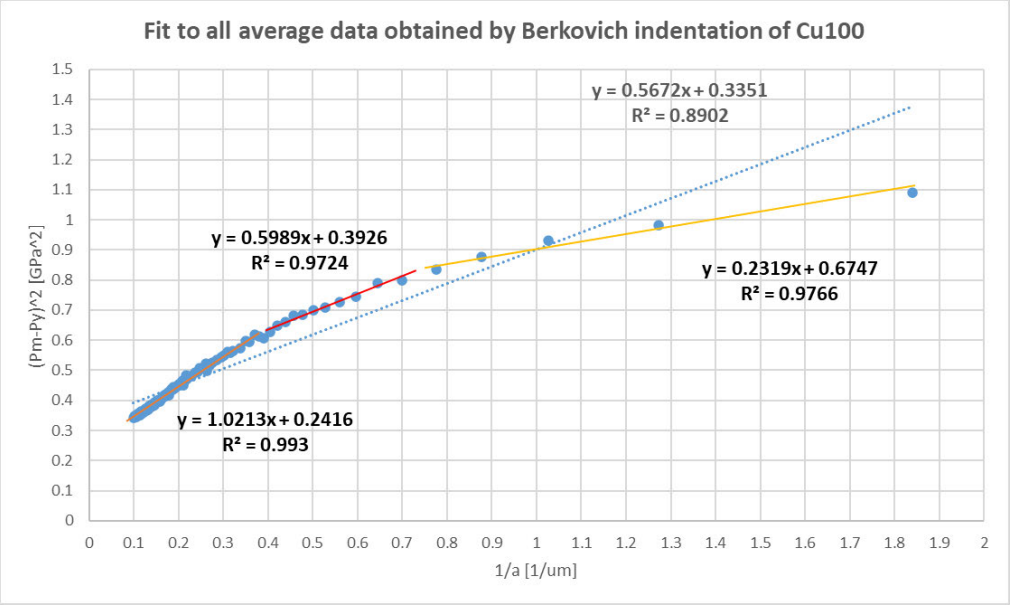

Fig. 68: Fit function to data from indentation on Cu100 using Berkovich indenter.

Two changes in the slope of the H^2 – 1/a curve can be seen in figure 68 which shows decrease in slope and increase in intersection constant by increasing indentation depth.

The calculated K_1 parameters for both indentation orientations are from highest to lowest in Cu100, Cu110 and Cu111 in order of magnitude. For $K_3\sqrt{\rho_s}$ parameters, an opposite trend can be seen.

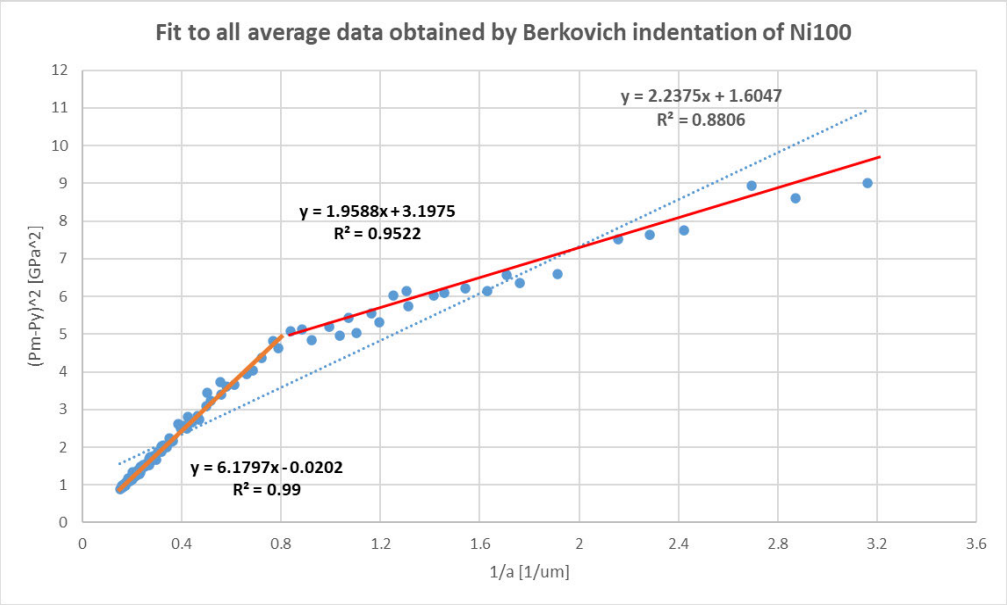

Fig. 69: Fit function to data from indentation on Ni100 using Berkovich indenter.

Two curves could be fitted to Ni100 unlike other FCC materials as shown in figure 69. This might be due to generated dislocations because of sample preparation which has diminished the sensitivity of material response or the change in slope might happen at some point with lower indentation depth.

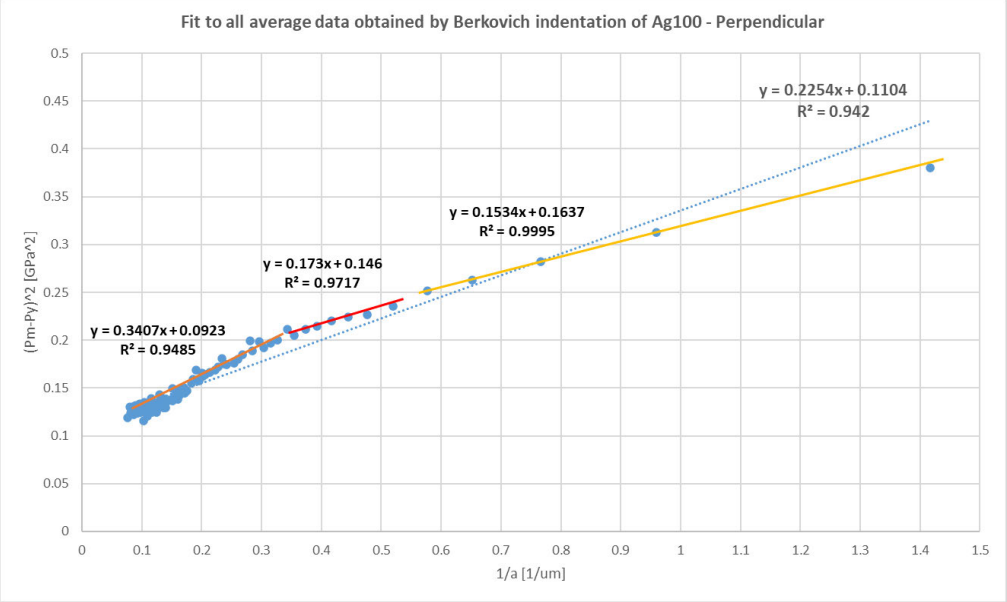

Fig. 70: Fit function to data from indentation on Ag100 using Berkovich indenter.

The model for silver is shown in figure 70 along with the fitted function to each regime of the complete curve.

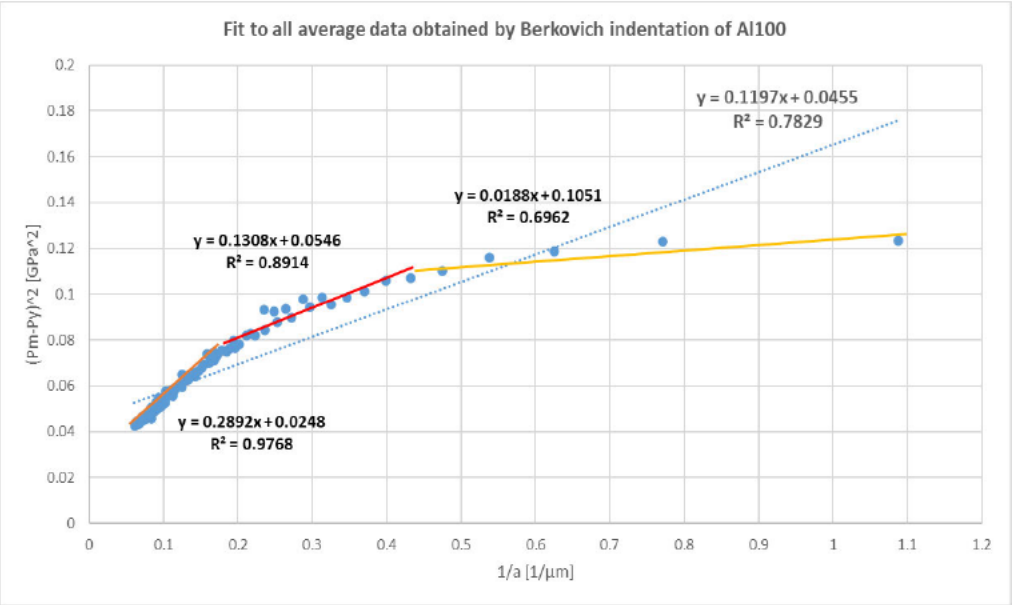

Fig. 71: Fit function to data from indentation on Al100 using Berkovich indenter.

The three sections divided the curve of aluminium has been depicted in figure 71. By increasing the indentation depth, the effect of dislocation density diminishes and plastic zone contribution to hardness increases. Table 8 is the summary of the extracted parameters from fitting linear function to each section of the shown analysis of the indentation data and the uncertainty of the fitted linear function for FCC materials.

Table 8: K_1 and $K_3\sqrt{\rho_s}$ parameters obtained from linear function fitted to the data.

Materials and extracted parameters	Cu001	Cu110	Cu111	Al001	Ni001	Ag001
Sec. 1: h_c [µm]	0.17-0.44	0.06-0.32	0.05-0.31	0.31-0.74	0.09-0.41	0.23-0.60
K_1 [GPa² µm]	0.2319	0.2744	0.3362	0.0188	1.9588	0.1534
Uncertainty	0.0207	0.0092	0.0142	0.0072	0.0992	0.0019
$K_3\sqrt{\rho_s}$ [GPa²]	0.6747	0.7967	0.9215	0.1051	3.1975	0.1637
Uncertainty	0.0253	0.0202	0.0319	0.0052	0.1554	0.0018
Sec. 2: h_c [µm]	0.48-0.91	0.33-0.72	0.34-0.82	0.82-1.94	-	0.67-0.99
K_1 [GPa² µm]	0.5989	0.5161	0.8014	0.1308	-	0.1730
Uncertainty	0.0319	0.0184	0.0385	0.0102	-	0.0131
$K_3\sqrt{\rho_s}$ [GPa²]	0.3926	0.5036	0.4519	0.0546	-	0.1460

Table 8 continued: K_1 and $K_3\sqrt{\rho_s}$ parameters obtained from linear function fitted to the data.

Uncertainty	0.0165	0.0135	0.0270	0.0028	-	0.0057
Sec. 3: h_c [µm]	0.93-3.63	0.75-3.09	0.88-3.18	2.02-5.94	0.43-2.37	1.03-4.71
K_1 [GPa² µm]	1.0213	1.0029	1.4496	0.2892	6.1797	0.3407
Uncertainty	0.0095	0.0226	0.0270	0.0053	0.0778	0.0086
$K_3\sqrt{\rho_s}$ [GPa²]	0.2416	0.2888	0.2120	0.0248	-0.0202	0.0923
Uncertainty	0.0019	0.0054	0.0060	0.0006	0.0288	0.0014

In this study, I have taken another approach by using a model based on slip distance theory. Similar studies [60][169] have used strain gradient plasticity to study length scale size effect of FCC materials of Nickel, Gold, Silver and Aluminium and found out a linear relationship for data at both micro- and nanoscales, but with different slopes for microhardness and nano-hardness data as shown below in figure 72.

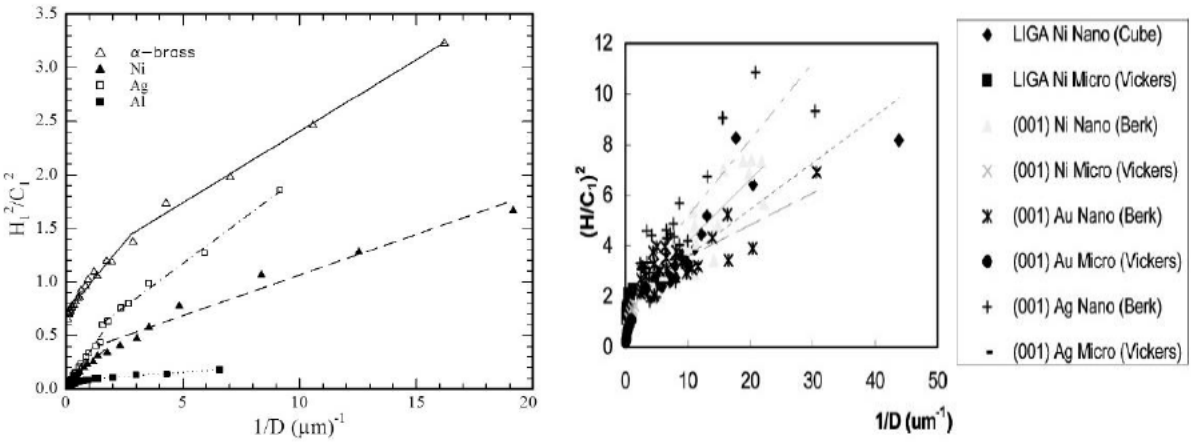

Fig. 72: Studies of FCC materials which covers micro- and nanoscales illustrates a non-linear behaviour [60][169]

The trend of change in the slope is observed not only in FCC materials but also in BCC ones. Hence, the sensitivity of this model can give a quantitative measurement of microstructure evolution in the spectrum of length scales.

The trend of change of K_1 and $K_3\sqrt{\rho_s}$ in different length scales were drawn for each material as shown in figure 73 which illustrates increase in K_1 by increasing the depth of indentation and decrease in $K_3\sqrt{\rho_s}$. The figures below indicates that trend. An important aspect which can be seen in the figures, is the depth, or length scale in the other words, for the change in the trend is different in different

samples which means a specific length scale cannot be allocated to all materials. There is change from nano scale to micro scale, however, this change does not happen exactly at 1µm depth.

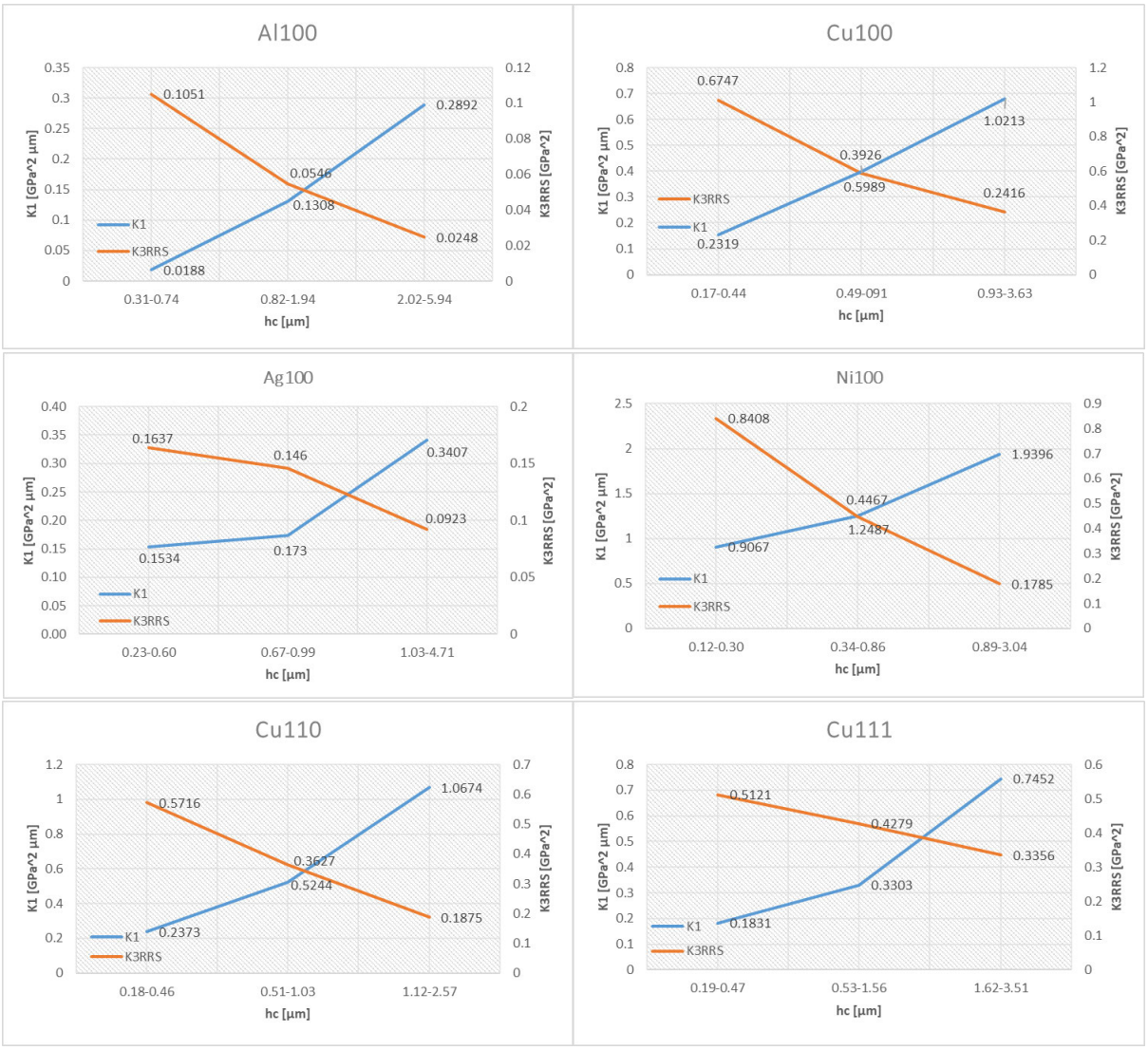

Fig. 73: Change of K_1 and $K_3\sqrt{\rho_s}$ of FCC materials in different length scales

As it has been pictured above for FCC materials, there are three distinct regions which have distinguished K_1 and $K_3\sqrt{\rho_s}$ values obtained from them. It is observed that by increasing the depth and moving from one region to the next one, K_1 increases while $K_3\sqrt{\rho_s}$ follows an opposite trend. It can find out that the contribution of K_1 and $K_3\sqrt{\rho_s}$ to hardness of the materials changes progressively.

K_1 is the constant in the equation which indicates the contribution of plastic zone and $K_3\sqrt{\rho_s}$ stands for the contribution of dislocation density (or any microstructural defect). The above figures clearly show rise in the K_1 and fall for $K_3\sqrt{\rho_s}$ by increase in the depth of indentation. The change in the slope is slightly higher around transition point from nano to micro size.

In the beginning of the indentation due to scarceness of dislocation and dislocation sources, a combination effect of geometry necessary dislocation (GNDs), decrease in dislocation segment length due to increase in dislocation density and source limitation [41] and lack of sufficient sources [34] play the role of accumulating load in plastic deformation in response to the imposed shape change at the surface creating a high dislocation density zone. This happens in the first stage of indentation shown in the graph where the depth of the indentation is still relatively shallow. By increasing indentation depth, dislocations move further into the microstructure and more slip systems are activated due to the applied force. Further increase in indentation depth activates more slip systems and moves more dislocations in different slip planes and slip direction and eventually decreases the effect of GNDs. Those are the mechanisms which causes the change in K_1 and $\mathrm{K}_3\sqrt{\rho_s}$ in the second stage. In those stages no plastic zone has been fully developed and there are scattered deformation-induced zones. Therefore, as it is indicated by K_1, the contribution of plastic zone size is going to be very small compared to depth of indentation. With each subsequent increment of plastic deformation due to increasing penetration, pre-existing dislocations are moved, and potentially multiplied. As deformation progresses, the number of dislocations participating increases dramatically. Hence, their movement and interaction carry the deformation and expands the size of the plastic zone until the third stage of size effect is reached. In the third stage, the plastic zone size has been fully developed and the change in K_1 indicates that as well. A fully developed plastic zone at this stage is a space which is manifestation of several slip planes and slip direction and the dislocations which have been nucleating, moving, and pinning in the numerus possible directions.

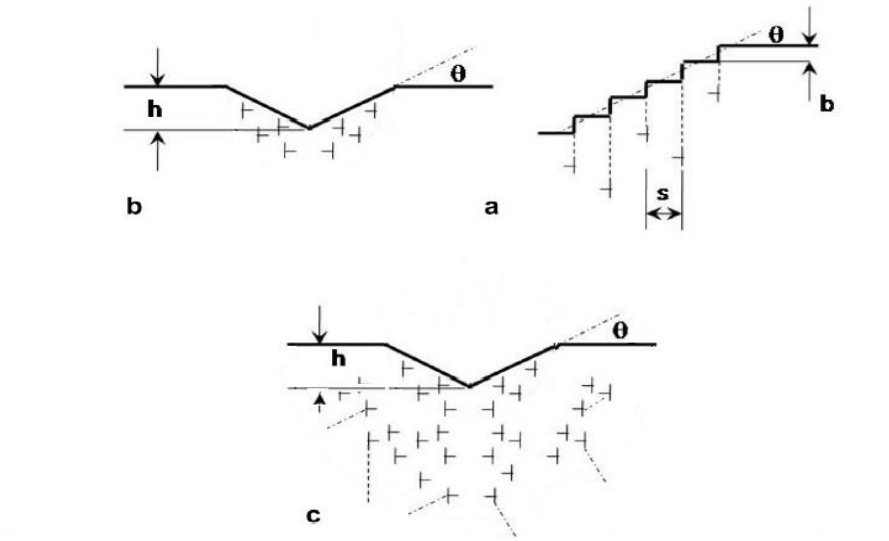

Fig. 74: Schematic explanation of dislocation nucleation, movement, and interaction through indentation by increasing depth of indentation from (a) creating geometry necessary dislocations (b) increase in number of dislocations to (c) movement of dislocation in arbitrary directions.

External length-scale effects may be observed at multiple stages over this wide range of sizes, because the mechanisms associated with dislocation storage, multiplication, motion, pinning, and nucleation are generally active over different length scales [63]. What we can see in FCC material, there is all of the associated mechanisms are happening at the same time, however, there is a mechanism which plays the main role in each region of the graph or in the other words, in each length scale.

It is common that as the test scale decreases, the influence of the microstructure and microstructural features diminishes because of interaction with less volume from the whole bulk of the material and all its defects. As less volume as is affected by the tip of the indenter means eliminating crystals defects and their share in plasticity. Therefore, the strength tends to approach the theoretical strength of the crystal. The difference in plastic deformation between FCC and BCC metallic materials in macro scale (bulk size) has already been known through various testing and comparison between those two microstructures. The measured hardness at the small-scale was entirely determined by the availability of dislocation sources and was unlikely to be affected by microstructural features. The crystal lattice must generate dislocations to allow for deformation during indentation. The material and its orientation, the indenter tip size, and the tip's displacement into the surface all affect the density and distribution of these dislocations. The effect of impurities no matter how small should not be ignored [156].

Various quantitative calculation including finding a trend in ratio of K_1/a and $K_3\sqrt{\rho_s}$ attempted. Another attempt was made to break down the equation 2.17 $K_i = k_i G^2 b \varepsilon_p \left[\frac{1-\lambda}{\lambda}\right]$. By knowing b: burger's vector, G: shear modulus, ε_p: 7% for Berkovich indenter and calculating $K_1$and $K_3\sqrt{\rho_s}$ for each, (1-λ)/λ which is the ratio of static to mobile dislocation density can be calculated. However, the result did not show any trend and (1-λ)/λ is not a constant value from the moment that indenter touches up to reaching the maximum indentation depth.

4.4.2 Plasticity Mechanisms and Length Scale Size effect in BCC Materials:

The same approach as done for FCC materials was taken for BCC materials to find out K_1 and $K_3\sqrt{\rho_s}$. The parameters have been extracted from test results for BCC samples. However, it is observed that unlike FCC materials, the graph shows a different characteristic. The graph for BCC materials can be divided into two regions instead of three regions that was the case for FCC materials.

Additional to K_1 and $K_3\sqrt{\rho_s}$ which have been written next to linear fitting function of each region, K_1 and $K_3\sqrt{\rho_s}$ of the linear function fitted to the whole data has been extracted and written next to it since fitting a linear function to the whole data was the first approach to analyse the collected data.

The R-squared has been added for each fitting function as well which is interpretation of r-squared is how well the regression model fits the observed data.

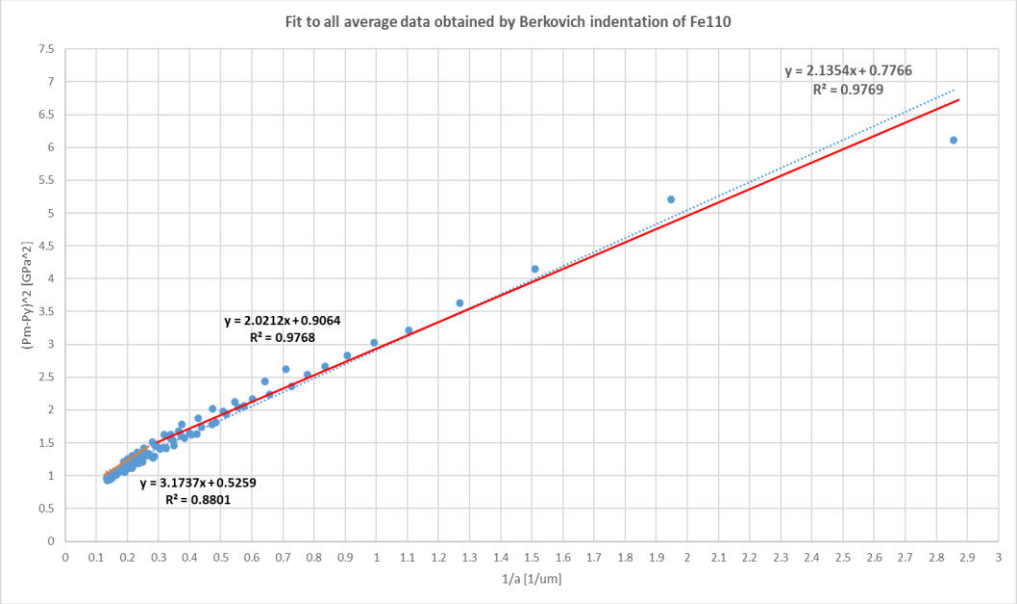

Fig. 75: Fit function to the data from indentation on Fe110 using Berkovich indenter.

Iron with 110 orientation shows a kink in the curve where the slope of the curve change. The change in the slope of the curve happens in 1.2µm. The slope of the fitted linear function to the data illustrated in figure 75. A comparison between the constants of the fitted function to each slope shows a trend. By increasing indentation depth, slope of the curve decreases and intersection constant increases. Those constants are indication for change in the plastic zone size and pinning effect which in this case since we have pure single crystals, that constant can be representative of dislocation density. Iron shows the smallest change in the slope between two regions in comparison with other BCC materials.

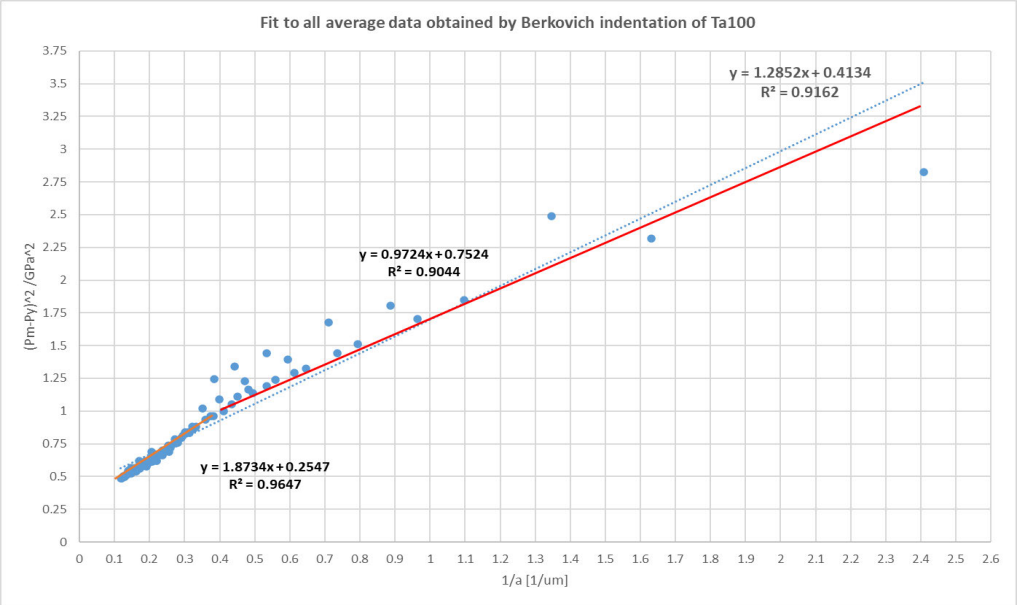

Fig. 76: Fit function to data from indentation on Ta100 using Berkovich indenter.

A kink in the curve of Tantalum100 is visible in depth of 0.7µm (Fig. 76). After that point, the slope increases and intersection point decreases. As indicated in table 7, K_1 increases and $K_3\sqrt{\rho_s}$ decreases by increasing indentation depth. Plastic zone size has almost ten times influence in hardness compared to dislocation density in high depth indents while in low depth indent, they have almost the portion.

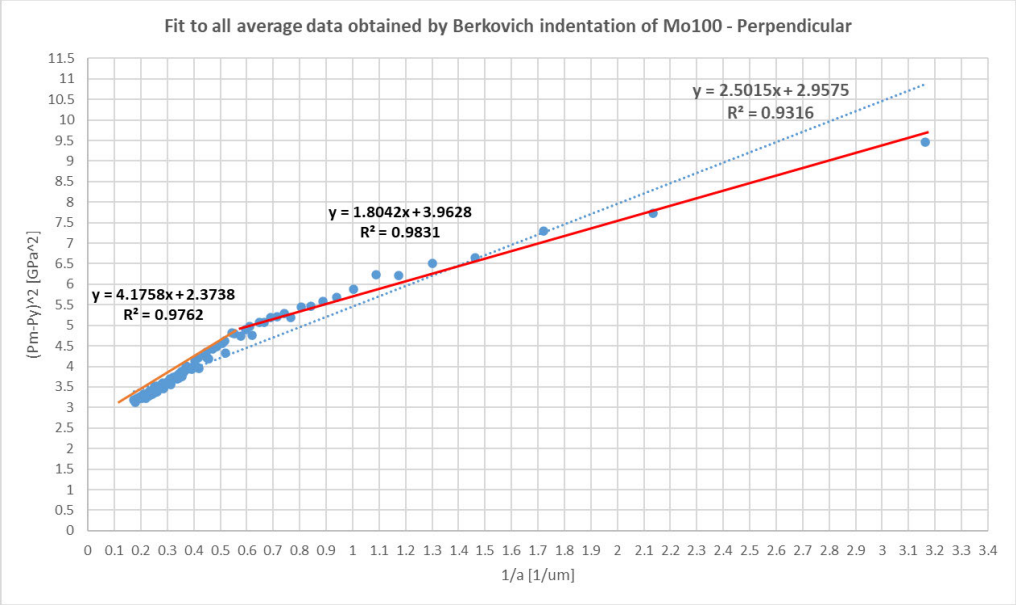

Fig. 77: Fit function to data from indentation on Mo100 using Berkovich indenter.

Molybdenum linear response changes at depth of 0.57µm and beyond that depth the material response follows another slope as shown in figure 77.

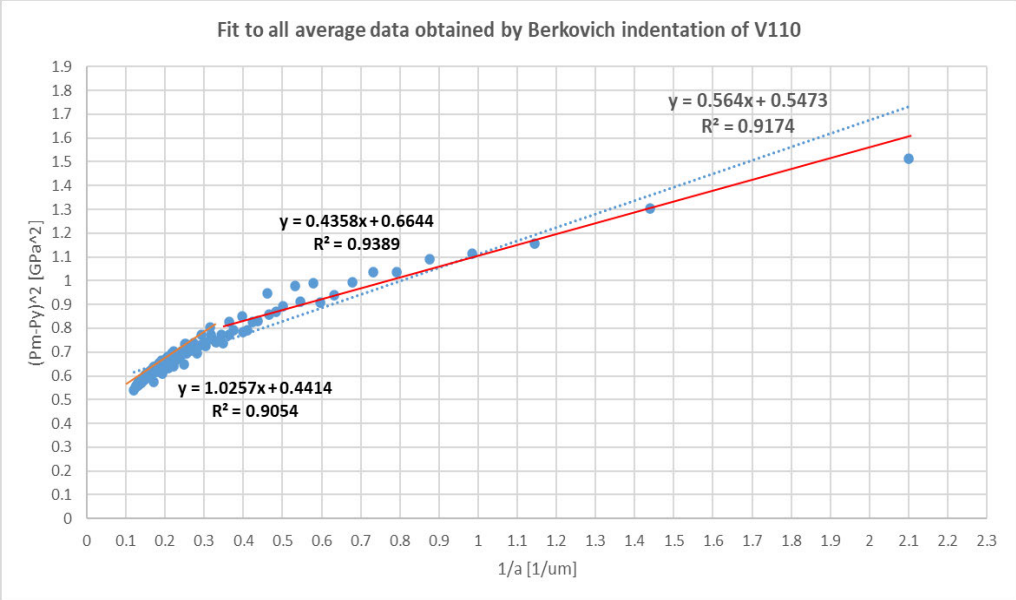

Fig. 78: Fit function to data from indentation on V110 using Berkovich indenter.

The same analysis of the hardness measurement performed on V110, as illustrated in figure 78 which indicates similar characteristic observed in other BCC materials. A transition in the slope of the curve happens for Vanadium110 at 1.03µm indentation depth. One linear function was fitted to lower depth indents and another linear function was fitted to indentation depth higher that that point. It appears that there is an exchange between contribution of plastic zone size and dislocation density in hardness after the transition point.

Table 9 is the summary of the extracted parameters from fitting linear function to each section of the shown analysis of the indentation data and the uncertainty of the fitted linear function for BCC materials.

Table 9: K_1 and $K_3\sqrt{\rho_s}$ parameters obtained from linear function fitted to the data.

Materials and extracted parameters	Fe110	Ta100	Mo100	V110
Sec. 1: h_c [µm]	0.11-1.26	0.13-0.65	0.09-0.57	0.15-1.03
K_1 [GPa² µm]	2.0212	0.8963	1.8042	0.4358
Uncertainty	0.0493	0.0860	0.0557	0.0222
$K_3\sqrt{\rho_s}$ [GPa²]	0.9064	0.8605	3.9628	0.6644
Uncertainty	0.0396	0.0913	0.0701	0.0167
Sec. 2: h_c [µm]	1.23-2.71	0.71-3.08	0.59-2.06	1.08-3.01
K_1 [GPa² µm]	3.1737	2.0185	4.1785	1.0257
Uncertainty	0.1565	0.0510	0.0738	0.0393
$K_3\sqrt{\rho_s}$ [GPa²]	0.5259	0.2283	2.3738	0.4414
Uncertainty	0.0322	0.0128	0.0244	0.0082

According to above mentioned graph, two linear functions with different slopes can be fitted to the collected data. The depth at which the change in the slope takes place is different for different BCC materials starting from the lowest to highest depth in the Molybdenum, Tantalum, Vanadium, and Iron.

For each fitting function a pair of K_1 and $K_3\sqrt{\rho_s}$ were extracted which represent the plastic zone size and dislocation spacing. K_1 and $K_3\sqrt{\rho_s}$ indicates the opposite trend of variation the way that by

increasing depth of indentation, the dislocation density is increasing whereas plastic zone size becomes bigger. The trend, as shown in figure 79, illustrates the change in contribution of each factor in hardness or in the other words strength of the materials.

Iron has the biggest plastic zone size in nano scale region followed by Molybdenum, Tantalum and Vanadium. The Molybdenum shows the sharpest increase in the plastic zone size by increasing indentation depth while Iron has the least tendency to plastic zone size growth.

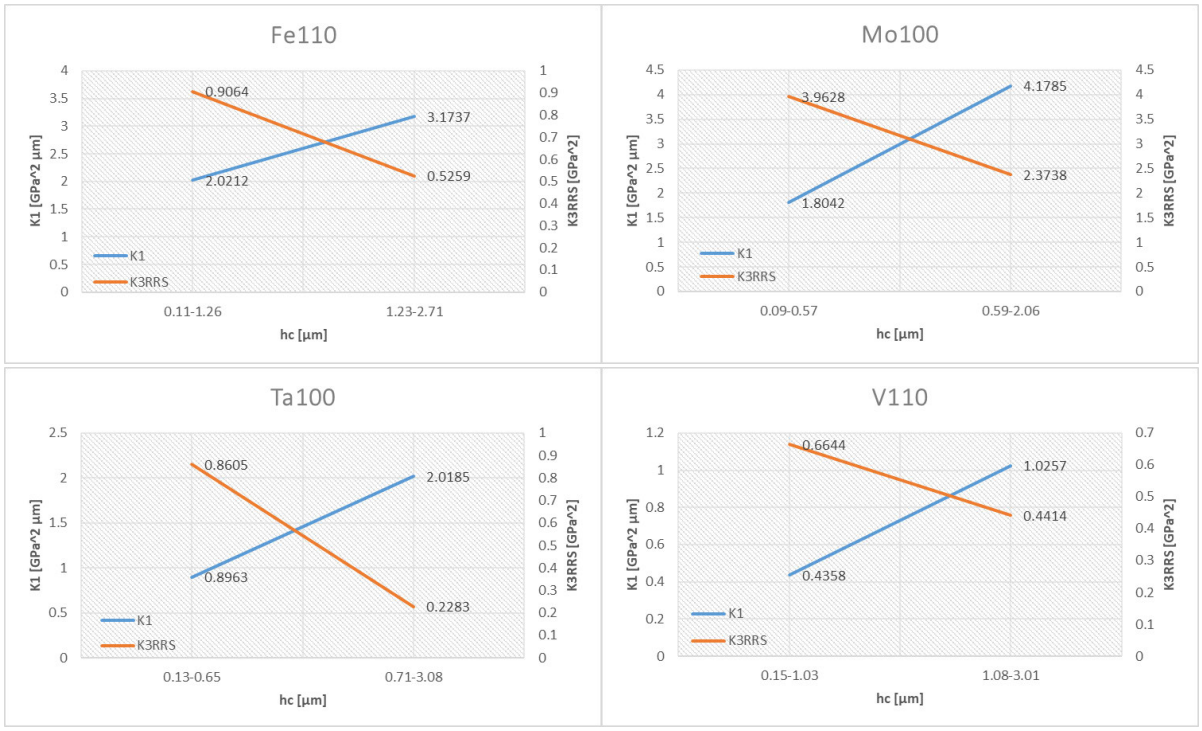

Fig. 79: Change of K_1 and $K_3\sqrt{\rho_s}$ of BCC materials in different length scales

Extracted dislocation density indicate Molybdenum with the highest number in the nano region and Investigation on single crystal Tungsten of different orientations using strain gradient plasticity to study length scale size effect [61] has found out a linear relationship for data at both micro- and nanoscales, but with different slopes for microhardness and nano-hardness data as depicted in figure 80 which is a similar trend in our findings.

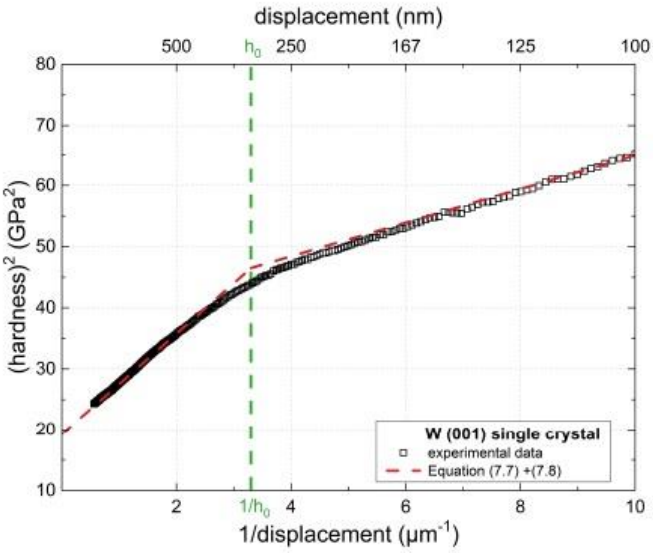

Fig. 80: Studies of BCC materials which covers micro- and nanoscales illustrates a non-linear behaviour [61]

Screw dislocations are the main type of dislocation in BCC structure metallic materials, and it should be noted that mobility of screw dislocation is significantly slower than edge dislocation, furthermore, due to the nature of the slip systems in BCC structure, the motion of dislocations is more restricted. The higher measured K_1 and $K_3\sqrt{\rho_s}$ values for BCC materials in comparison with FCC materials strength, implying that plasticity is likely driven by the intricate motion and interactions of dislocations.

K_1 in micro regime, where the first function has been fitted to the data and depicted in figures 81 and 82, indicates a linear relationship with shear modulus (G) and Elastic modulus (E) for all FCC and BCC samples.

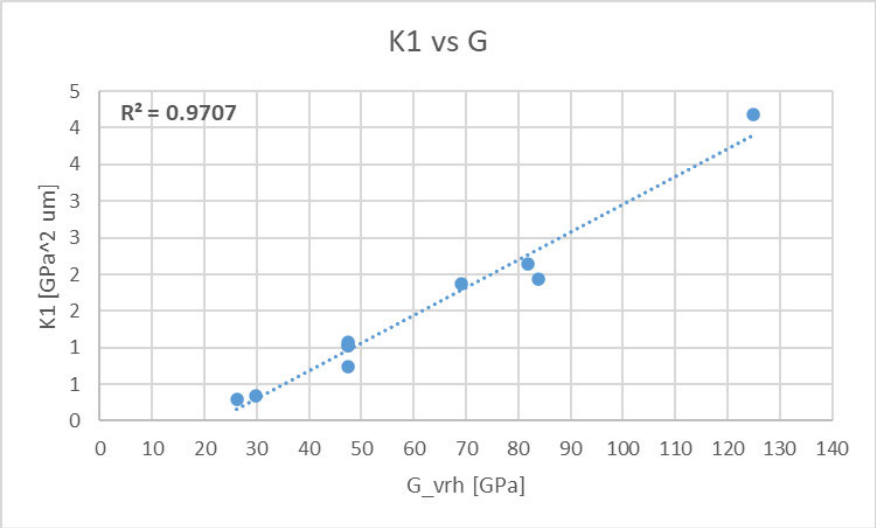

Fig. 81: K_1 indicates a linear relationship with shear modulus for BCC and FCC Materials

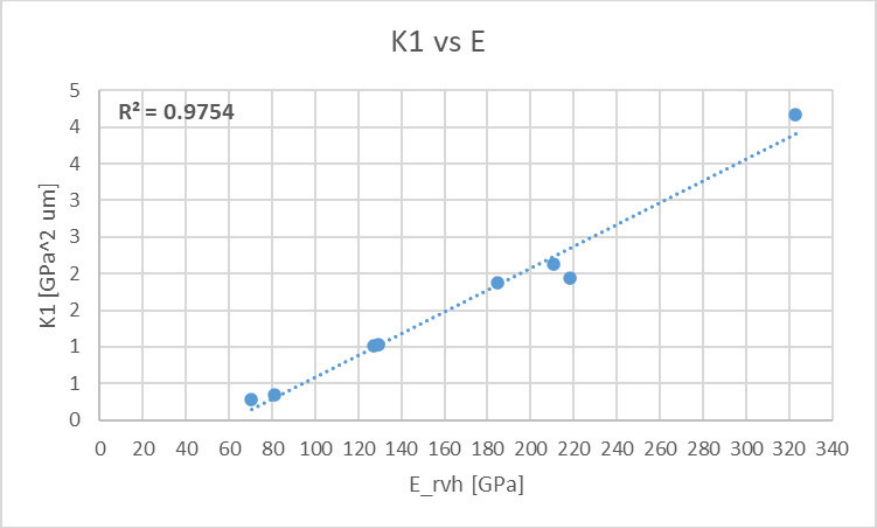

Fig. 82: K_1 indicates a linear relationship with shear modulus for BCC and FCC Materials

This observation might be an indicator that the size effect is fading away by increasing the length scale and other intrinsic properties of a bulk material i.e., elastic modulus and shear modulus are far more effective.

5. Transmission Kikuchi Diffraction Microstructural Investigation of Indentation

5.1 Introduction

A Molecular dynamic simulation study fcc and bcc metals of different plane orientations [164] shows formation of a complicated dislocation network beneath the indent and its length depends on dislocation reactions and orientation of slip planes. Higher extension of the dislocation network in fcc crystals is observed. 3D discrete dislocation simulation on the indentation on Cu single crystal [172] and calculation of plastic zone size using cavity model and comparison with TEM observation of indent induced plastic zone have shown a good agreement when active slip systems correspond to those observed experimentally was taken for nucleation. The highest dislocation density found out to be in the centre beneath the indentation. A comparative study [173] of the same material employing the same using boundary conditions extracted from experiments shows a good agreement in hardness value. Nano indentation study of Fe-9%Cr ODS [174] using various approaches of cavity model, FEM simulation and TEM observation has shown difference in result, however, evidence indicates that the plastic zone has an elongated shape that extends further below the indent than radially. Study of Finite element simulation of Berkovich indentation in copper [175] using modified model based on Nix and Gao model has figured out a factor 1.9 times of contact radius for plastic zone size. The result of this study found that factor to be approximately 3 times.

5.2 Experimental

FIB inside SEM was employed to perform in-situ lift-out of the indented samples. Thinning process of the lamellas were done stepwise to reach adequate electron transparency required for TKD.

To be able to look into microstructural evolution of the plastic zone area below indentation, two lamellas from each sample were taken out using FIB technique. One lamella with an indent of 100nm and the second one with an indent of 500nm depth. Lamellas were taken from Aluminium, Copper, and Nickel of 001 orientation as representative of FCC materials and two lamellas from Iron 110 orientation with depth of 100nm and 500nm as representative of BCC materials. Figure 83 shows the FIB performed on the samples as they are ready to be cut from the sides and be taken out using needle. The sizes of the lamellas before thinning process have been mentioned in the Table 8. Thinning was performed on the lamellas to reach the thickness of approximately 100nm for further TKD investigations. The optimum thickness of the lamella for TKD process should normally be the same as a TEM lamella to allow the transition of ions through the lamella.

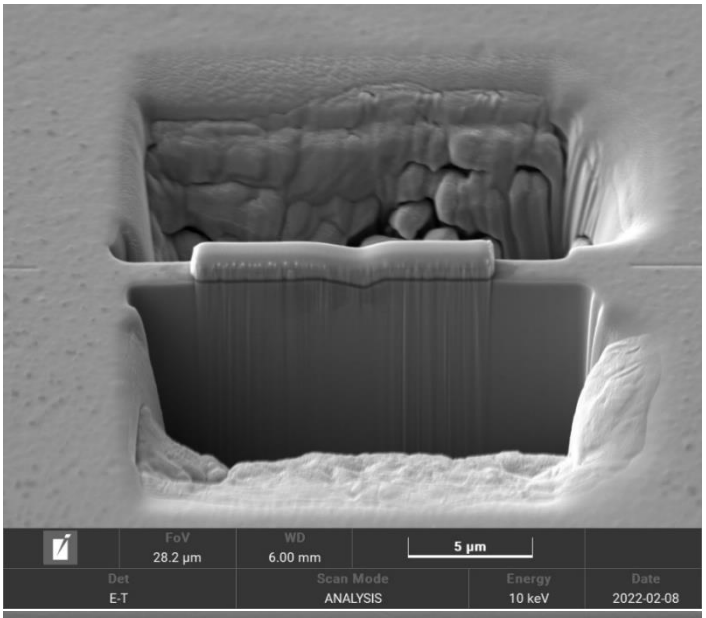
FoV
28.2 µm
WD
6.00 mm
5 µm
Det
E-T
Scan Mode
ANALYSIS
Energy
10 keV
Date
2022-02-08

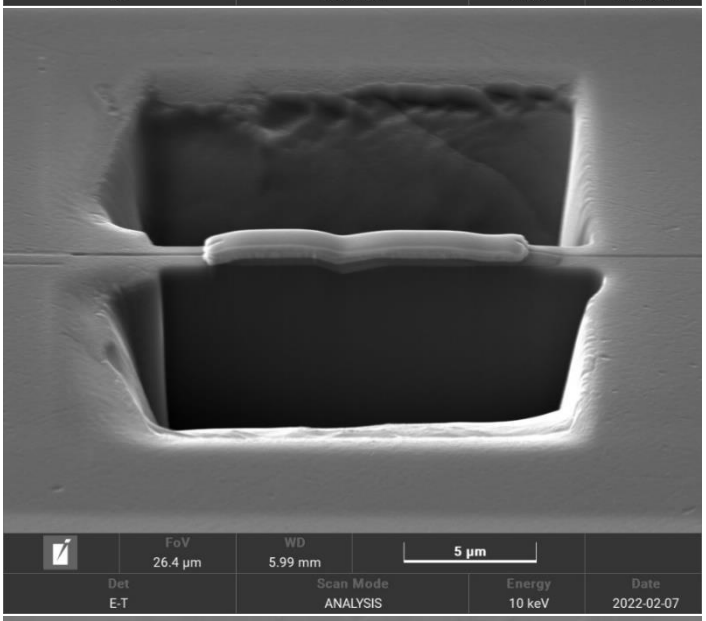
FoV
26.4 µm
WD
5.99 mm
5 µm
Det
E-T
Scan Mode
ANALYSIS
Energy
10 keV
Date
2022-02-07

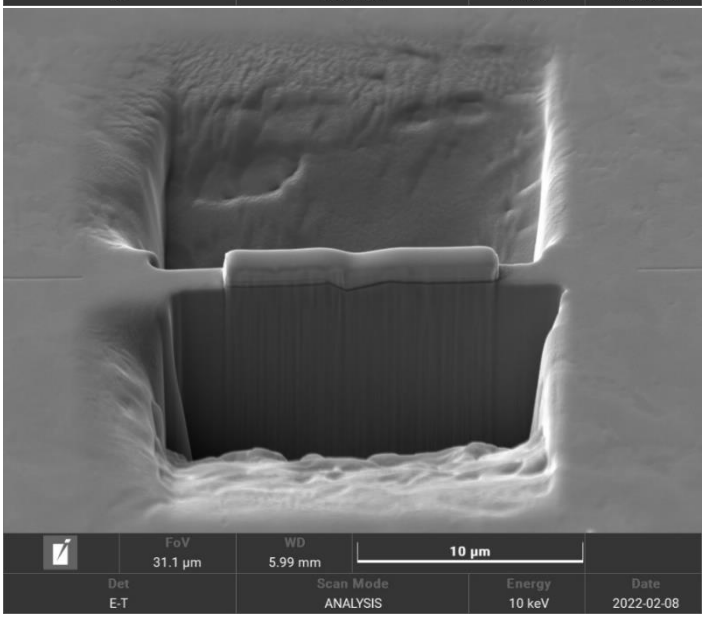
FoV
31.1 µm
WD
5.99 mm
10 µm
Det
E-T
Scan Mode
ANALYSIS
Energy
10 keV
Date
2022-02-08

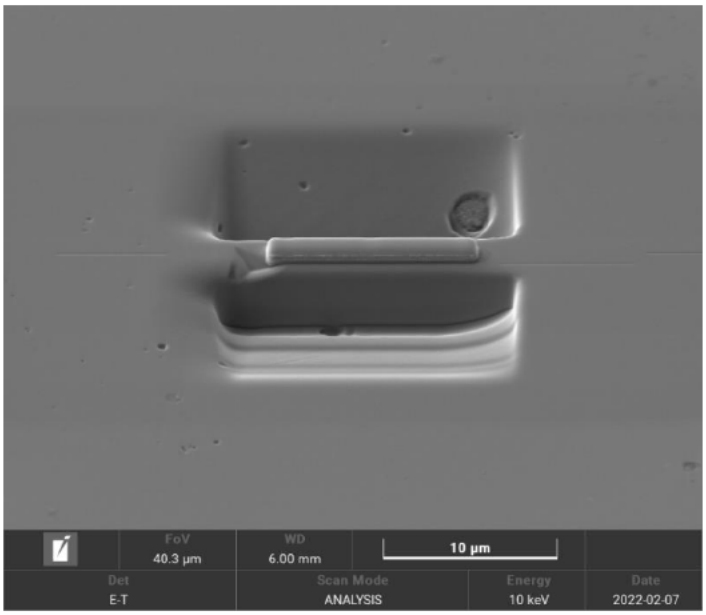

Fig. 83: FIB micrograph of lamellas of bulk material after drenching both sides of the lamella and before lift-out; from top to bottom: Copper, Aluminium, Nickel, and Iron. The shown cross section was taken from the middle of indent where the highest depth is reached.

Table 10: Lamella sizes taken out of bulk samples.

FIB/TKD lamellas	Depth (µm)	Width (µm)	Thickness (µm)
Al / 100nm deep indent	5	10.3	1.5
Al / 500nm deep indent	6.9	13.6	1.5
Ni / 100nm deep indent	5.6	12.8	1.5
Ni / 500nm deep indent	7.8	12.5	1.5
Cu / 100nm deep indent	6.2	13.1	1.5
Cu / 500nm deep indent	7.2	13.1	1.5
Fe / 100nm deep indent	5.2	12	1.5
Fe / 500nm deep indent	7.1	13.2	1.5

5.3 Result and Discussion

The analysis on the TKD results of the plastic zone generated below indents for Aluminium, Nickel and Copper is proving different evolution of the deformation-induced zone which can be related to difference in dislocation mobility of the materials with respect to stacking fault energy.

Figure 84 shows two scans of the area of interest from copper lamella below the indented surface of 500nm deep. Maximum misorientation was set to 2°.

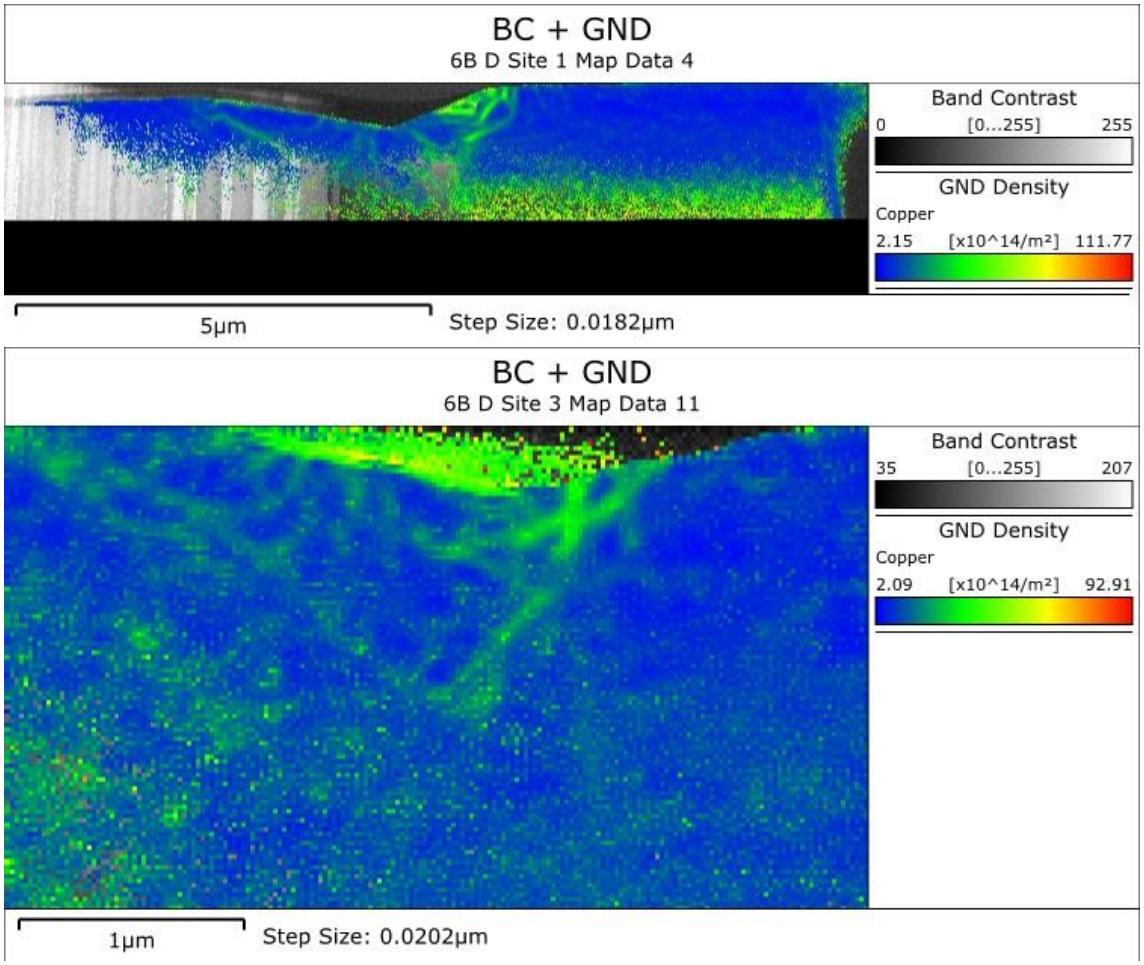

Fig. 84: TKD images of two scans of plastic zone below the indentation of copper with depth of 500nm using Berkovich indenter with maximum misorientation of 2°. The shown cross section was taken from the middle of indent where the highest depth is reached.

The images show the high density of GNDs on the surface of the indented area and activated slip systems in different directions below the indent, but the dislocations have gone away up to certain distance where they have interacted with each other to form a plastic zone which is not fully developed. The farthest the dislocation move happens where the tip of the indenter has pushed through the material.

The TKD images of Nickel for 100nm and 500nm indent depths are shown in figure 85.

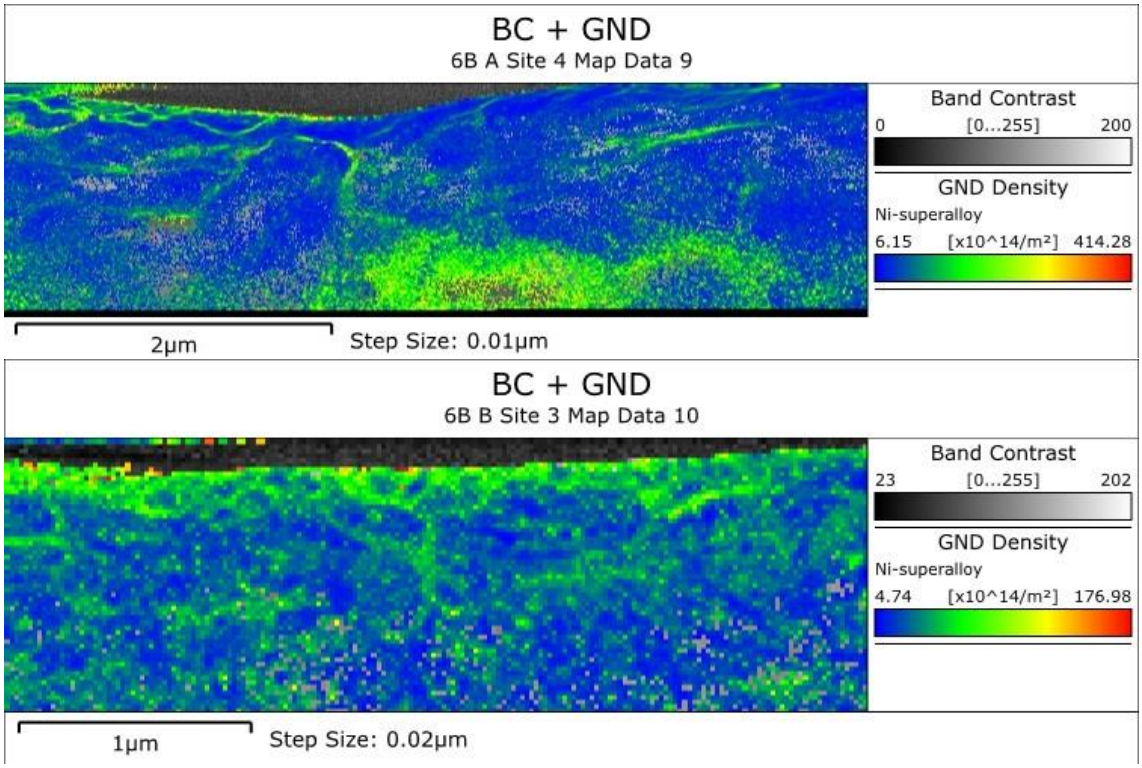

Fig. 85: TKD images of two scans of plastic zone below the indentation of nickel with maximum misorientation of 2°. The upper image with depth of 500nm and the lower image with depth of 100nm using Berkovich indenter. The shown cross section was taken from the middle of indent where the highest depth is reached.

In the image with 500nm depth of indentation, there is a similarity and a contrary with copper. The activation of slip systems in various direction can be seen in the deformation-induced zone below the indent while it seems that they are moving further and there is less of interaction. 100nm depth image shows and high density of GNDs, however, a bit more dispersed in comparison with copper.

Dislocation density measurement using TEM of compression tested Nickel samples with variety of diameters [176] shows increase in dislocation density by decreasing in pillar diameter. As it can be seen in indented Nickel samples, the density of the dislocation is higher in the low depth indentation with respect to the volume involved in deformation.

The TKD images of aluminium, as illustrated in figure 86, indicates another matter in respect to dislocation mobility. The upper image shows the scan of the whole lamella taken out by FIB technique. There are visible damages which have been created during FIB. The lower image is the area below indentation of 500nm depth. The maximum misorientation have been set to maximum 2°. The dislocations have spread more homogenously in comparison with nickel and copper with the similar indentation depth. Also, dislocations in aluminium have travelled a farther distance as well. The dislocation network for FCC materials with larger stacking fault ribbons (lower stacking fault energy) is more entangled and the highly entangled FCC networks hinder dislocation mobilization.

Misorientations increases as a result of dislocations accumulation which itself is a result of inhomogeneous straining. Dislocation density rises by accumulation of dislocations, and this is in definition called strain hardening. Therefore, effective plastic strain can be linked to misorientation. The role of geometrically necessary dislocations (GNDs) and statistically stored dislocations (SSDs) has been defined by allocating GNDs to deal with inhomogeneous straining and SSDs to carry homogeneous straining. So misorientation is a measure of GNDs and vice versa [162]. That indicates the change from homogeneous strain to inhomogeneous strain by decrease in stacking fault energy in FCC material since the misorientation is more visible first in copper and then Nickel and a homogeneous strain in Aluminium. As seen in figure 62, though the same strain has been applied (7& for Berkovich indenter), less misorientation is visible in TKD images of Aluminium. This indicates that the strain has been carried by to a longer distance into the material. However, having lower stacking fault energy in copper and nickel reduces that capability for their dislocation to be as mobile as aluminium and hence the raises the possibility of interaction of dislocations in the area close to the point of deformation applied by the indenter.

The presence of a relatively high and uniform SSD density in the background for Aluminium can be interpreted as a significant portion of the plastic strain being homogeneous.

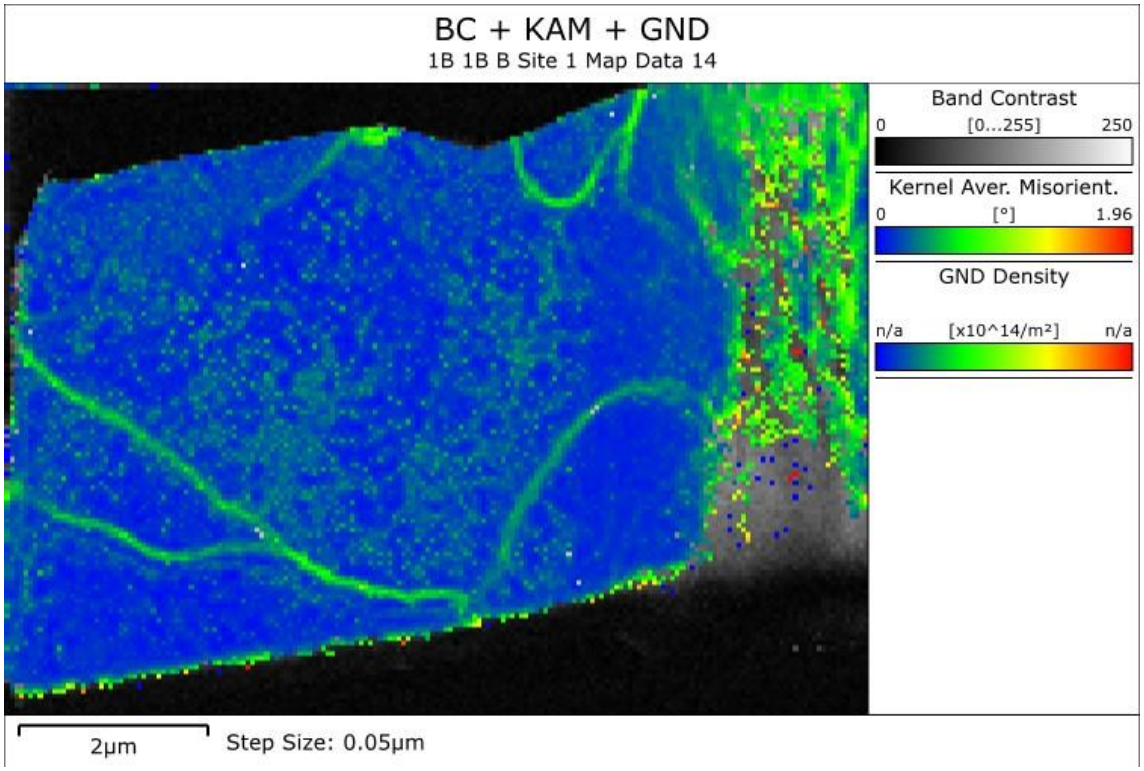

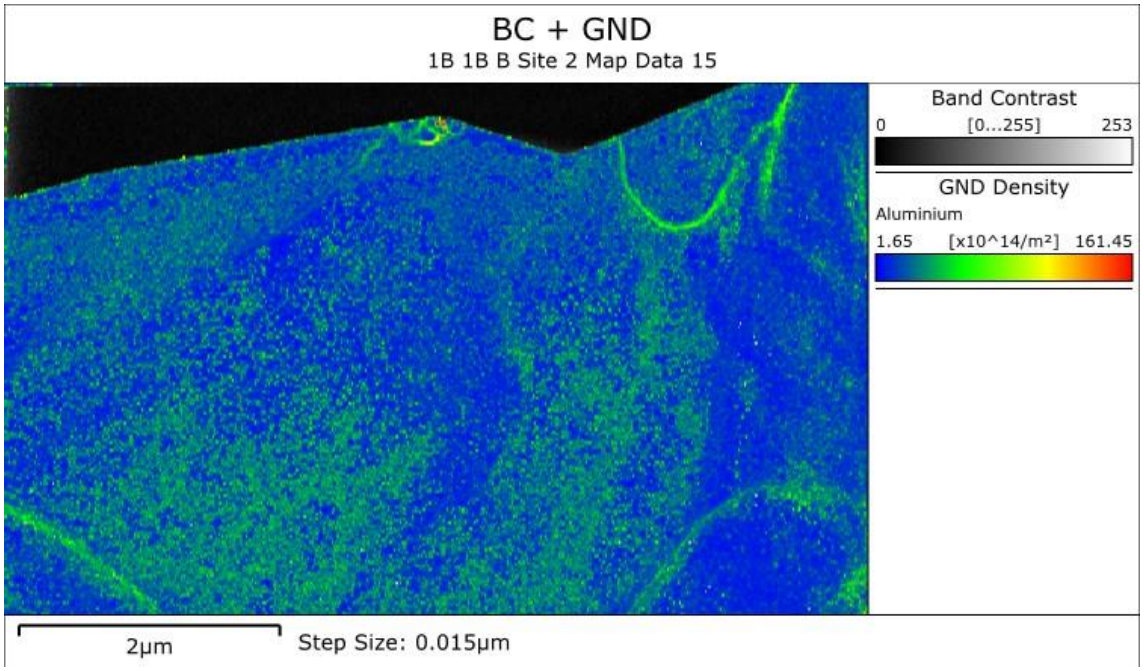

Fig. 86: TKD images of two scans of plastic zone below the indentation of aluminium with 500nm depth using Berkovich indenter and with maximum misorientation of 2°. The shown cross section was taken from the middle of indent where the highest depth is reached.

The results of compression testing on pillar of FCC materials shows that the dislocation travels outside of the pillar which causes increase in the strength of the tested pillar. This increase has been the basis for starvation model to explain size effect. Starvation model and the free surface effect are not applicable to nanoindentation, nevertheless, the compression testing gives an insight into inherent difference between BCC and FCC materials in dislocation nucleation and dislocation mobility. On the other hand, the similar trend was not observed in BCC materials.

The analysis on the TKD results of the plastic zone generated below indents of 500nm deep for Iron has been done to have a better understanding of the evolution of the deformation-induced zone generated below the indenter as seen in figure 87. The activation of different slip system from the surface where the indenter has touched the surface is clearly visible. The dislocations have moved away from the indent, however, up to a certain distance due to their interaction.

More misorientation is visible in Iron in comparison with FCC materials which is a proof for effective strain due to more accumulation of dislocations. That might be because of restricted possibilities for movement of dislocations in BCC materials in comparison with FCC materials. In comparison with the FCC materials, the plastic zone below the indent of the same depth has developed more. This might be attributed to low mobility of screw dislocations in bcc metals leading to either conventional dislocation-dislocation interactions or pile-ups of screw dislocations in the vicinity of dislocation sources [26].

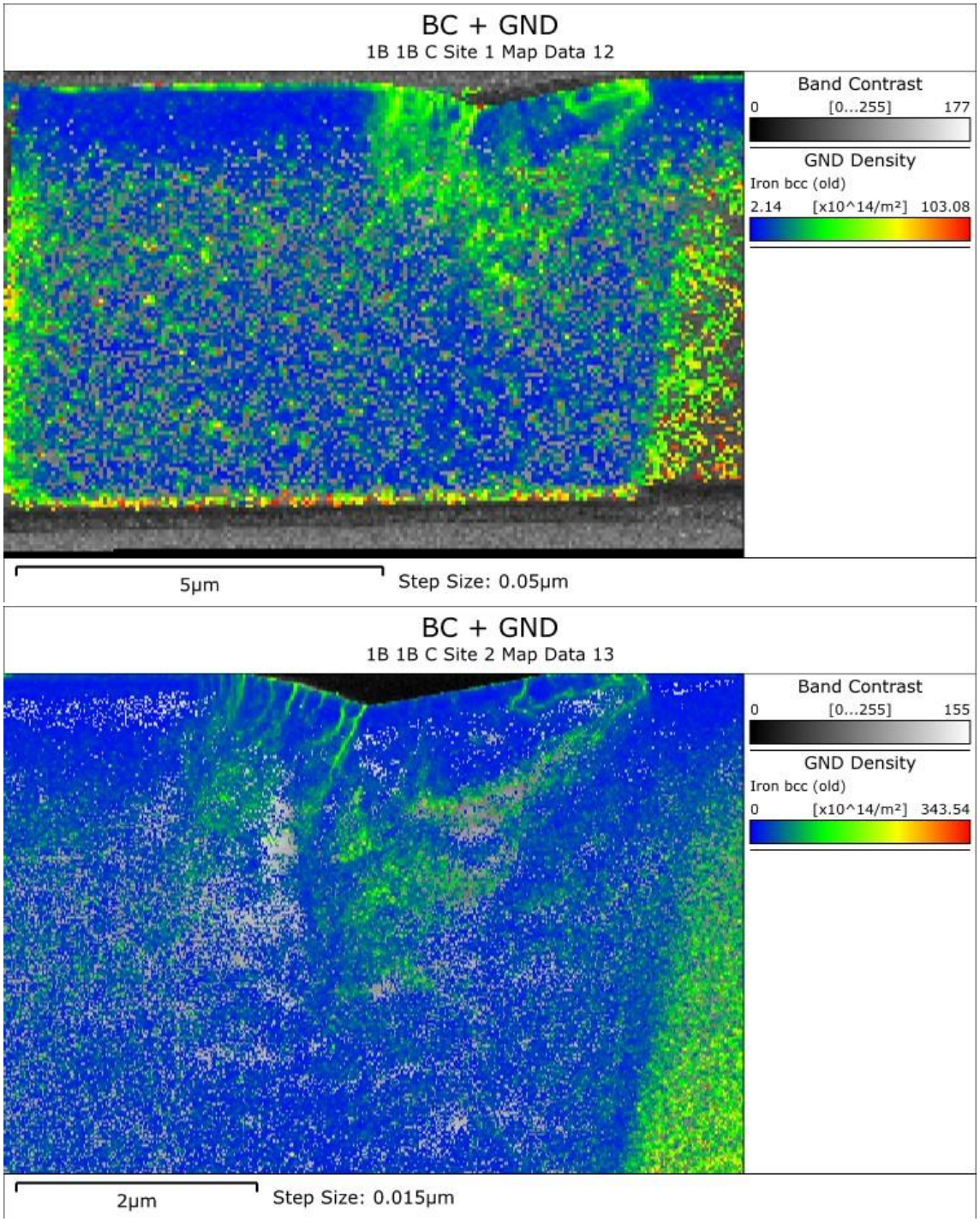

Fig. 87: TKD images of two scans of plastic zone below the indentation of iron with 500nm depth using Berkovich indenter and with maximum misorientation of 2°. The shown cross section was taken from the middle of indent where the highest depth is reached.

6. Conclusion:

In this study, Nanoindentation was performed on a variety of FCC and BCC structured single-crystal metallic materials to measure hardness, investigate size effect phenomena, and link stacking fault energy with the size effect behavior of the materials.

• The existence of indentation size effect in a depth range of 100nm to 5µm in all FCC and BCC metallic materials was observed. The measured hardness for the materials shows a good agreement with other studies and measured elastic modulus shows a good agreement with the calculated elastic modulus.

• A new model was verified and can be used to explain indentation size effect in a novel way. The model is based on slip distance theory and categorizes the coupling effect of plastic zone size and dislocation density which render every and each measured hardness value. A new way of interpretation of the analysis and its perception has been proposed based on decoupling the contribution of plastic zone size and dislocation density to the hardness. It is comprehended that discrete dislocation dynamics should be used to address plasticity mechanism in each length scale and not a single mechanism is accountable for explanation the size effect throughout indentation depths.

• Crystallographic structure affects the behavior of metallic materials at different length scales. The analysis of indentation testing reveals the difference between FCC and BCC materials in terms of change in the slope of the H^2–1/a curve. The transition in FCC materials happens in a continuous way, however, in BCC materials a distinctive kink or change in the slope is apparent. Throughout the indentation depth, three regions could be assigned to FCC materials and two regions to BCC materials. This means that alteration of plastic zone size and dislocation density in FCC materials happens continual throughout the indentation as well as the exchange in influence of each factor in hardness. In low depth indents, the plastic zone has not fully formed, therefore, its contribution to hardness is small. In contrast, dislocation density is high due to the accumulation of geometry necessary dislocation around the indent in a very small volume of material.

• The hardness values and the rise in hardness of the tested FCC materials coincide with each other after normalizing the hardness values by far-filed hardness. Since no trend in the size effect and rise in the hardness could be observed for sorting out the materials in this study, no connection could be made between size effect and stacking fault energy of FCC and BCC single-crystal metallic materials.

• TKD investigation show a restricted mobility of dislocation for low stacking fault FCC materials and BCC materials meaning there is an increase in the tendency of dislocation-dislocation interactions which leads to quicker formation of a plastic zone below the indentation. Based on observation through TKD investigation, it can be perceived that plastic zone growth does not happen in a similar

rate for materials. Also, plastic zone size evolution varies with indentation depth. In aluminium, the dislocations have moved 10 times the indentation depth of 500nm without forming a distinct plastic zone, however, copper has just started forming a plastic zone with an extension of approximately 1μm. Iron has a distinguished plastic zone at the same indentation depth.

Future work(s):

In spite of all the efforts put into this work to assure the precision and accuracy of the measurements, there is always room for improvement. There are other methodologies and facilities that can be employed to shed light on our understanding of the matter.

In this study, the effect of stacking fault energy as one of the intrinsic properties of materials, was investigated. However, the observed ISE mechanism transition also raises several fundamental questions about other intrinsic parameters of materials and their influence, which should be addressed in future studies. First, the effect of crystal structure—stacking fault energy for FCC and BCC structured materials with specific crystallographic orientation were examined, but how does the transition beyond the point where continuum mechanics hold true occurs in materials with other crystal structures, such as hexagonal close-packed (HCP), since alteration of crystal structure changes the slip systems and accordingly affecting the mobility of dislocation and the possibilities of interactions. The importance of crystallographic orientations should be taken into account, since indentation on surface with different crystallographic orientations activates different slip systems. Second, microstructural feature effects—how would existing dislocations affect the test result, hereby, this work explained the effect of sample preparation. Grain boundaries as another microstructural feature and its importance in pile-up effect and as a source for dislocation generation. Finally, chemistry effects—alloying elements are known to modify the microstructure by adding or replacing atoms in crystals which affect the strain field and energy of atomic bonds that moving dislocations are interacting with. Thus, how would alloying affect the ISE mechanism transition? A comparison between pure metals and alloys which have roughly similar stacking fault energies, may lead yet to better understanding of the effect of SFE.

It has been already emphasized that *"plasticity theories do not consider changes to the fundamental deformation mechanisms, such as those associated with truncating the mean-free-path, glide sources, kink migration distances, etc. that intrinsically occur with limiting the physical dimensions of a deforming volume. Especially for single crystals, there remains a fundamental challenge to systematically investigate length-scale effects on plastic flow at the sub-millimetre, micron, and nanometre dimensions"* [75]. Perhaps, any model which tries to fit a function using regression to the obtained data from testing, should consider a way of coupling microstructural deformation micro mechanisms and the obtained test data. Or the effect of each mechanism on dislocation mobility and dislocation nucleation which represent the plastic zone expansion and the mean free path. In-situ TEM or SEM/EBSD testing in conjunction with nanoindentation may help build a bridge between the data and plasticity mechanisms at different length scales.

Using a nanoindentation equipment with the capability of reaching indentation depth of a few nanometres, could help reach more comprehensive conclusion on even smaller length scales. Also, using different indenters can create different materials response and plastic zone shape and size. Berkovich indenter applies 7% strain at maximum load, whereas other indenters [that] apply different strains can cause variations in deformation mechanisms during indentation.

Performing tests at different temperatures may yield different results because of thermally activated deformation mechanisms in those materials. The activation of other deformation mechanism may enhance the effectiveness and influence of stacking faults through increased mobility of screw dislocations and cross slip.

These issues are worthy of further investigation, both experimentally and computationally.

Appendices

Appendix I

Sample preparation parameters

Sample	Grinding	Polishing	Polishing	Polishing	Polishing
Copper	800 10N 5min 1200 10N 5min 2500 10N 4min	9 µm Multicloth Polycrystal 20N 10min	3 µm Multicloth Polycrystal 20N 10min	1 µm Multicloth Polycrystal 20N 10min	0.06 µm Chemicloth Silica
Iron	800 15N 5min 1200 15N 5min 2500 20N 3min	9 µm Multicloth Polycrystal 35N 3min	3 µm Multicloth Polycrystal 35N 3min	1 µm Multicloth Polycrystal 35N 3min	0.06 µm Chemicloth Silica
Gold	800 17N 30s 1200 17N 30s 2500 17N 30s	9 µm Multicloth singlecrystal 20N 45sec	3 µm Multicloth singlecrystal 20N 45sec	1 µm Multicloth singlecrystal 20N 1:30min	
Silver	800 10N 4min 1200 10N 5min 2500 10N 4min	9µm Cashmere cloth Polycrystal 15N 5min	3µm Cashmere cloth Polycrystal 15N 5min	1µm Cashmere cloth Polycrystal 15N 5min	0.06 µm Chemicloth Silica
Vanadium	800 15N 5min 120015N 5min 2500 15N 4min	9µm Cashmere cloth Polycrystal 35N 4min	3µm Cashmere cloth Polycrystal 35N 4min	1µm Cashmere cloth Polycrystal 35N 4min	0.06 µm Chemicloth Silica
Tantalum	800 10N 5min 1200 10N 5min 2500 10N 4min	9µm Cashmere cloth Polycrystal 35N 5min	3µm Cashmere cloth Polycrystal 35N 5min	1µm Cashmere cloth Polycrystal 35N 5min	
Nickel	800 15N 5min 1200 15N 5min 2500 20N 3min	9 µm Multicloth Polycrystal 25N 3min	3 µm Multicloth Polycrystal 25N 3min	1 µm Multicloth Polycrystal 25N 3min	0.06 µm Chemicloth Silica

Since there is a big difference between hardness of the mentioned materials and due to their magnetic properties, different sets of cloths were employed for polishing to avoid embedding worn particles

from one material into another. Samples were cleaned ultrasonically after each step of grinding and polishing using high purity propanol or methanol.

Tendency to form oxidation layer on the surface and work hardening rate are other factors to deal with. Different sets of sample preparation adjustments are needed to tackle each issue.

SEM/EBSD examination proved that sample preparation using above mentioned parameters is well enough for samples like Nickel and Iron to give a surface finish, roughness and lack of work hardening on the surface which is needed for Nano indentation. For copper, vanadium, Tantalum samples, a perfect surface finish could be obtained, however, a work hardened layer forms on the surface which prevents Kikuchi patterns to be gained. As a solution, electropolishing was done which is capable of removing a few nanometres from surface and at the same time keeping surface roughness small enough for Nano indentation testing.

After each preparation SEM/EBSD measurement was performed in order to find out the best combination for surface finish and avoidance of creation of a work-hardened layer on the surface.

Forming a work-hardened layer on the surface of some samples is an aspect which was noticed after sample preparation and during EBSD measurements to find out crystallographic orientation. There is a need to perform electropolishing on more samples so that a very high and strong Kikuchi pattern could be obtained.

Whereas grinding and polishing tends to leave a thin layer of surface distortion due to nature of having mechanical contact and applied load during the process, electrolytic preparation can be employed as supplementary metallographic surface preparation. By proper adjustment of parameters such as voltage, flow, time and type of electrolyte, the formed layer of surface distortion can be removed. Electrolytic polishing can be followed by electrolytic etching to enhance contrasts in the specimen's microstructure. However, it must be taken into account to set the test parameters carefully to achieve the desired surface finish i.e. surface roughness of Ra (Ra is the arithmetical average of roughness [177] because prolonged electropolishing tends to roughen the surface which has an unwanted influence on both EBSD patterns and the roughness required for Nano indentation testing [178].

Different parameters were tested for samples which needed to be electropolished to get the best finish surface. It should be noted that even for the same materials with different crystallographic orientation, electropolishing parameters like time and voltage should be adjusted since they have different atomic packing factor in different orientations.

Electropolishing using D2 electrolyte (Struers) and process parameters 24v for polishing and 2v for etching and duration of 12 seconds and 2 seconds for polishing and etching of FCC materials and A3

electrolyte (Struers) for BCC materials were used respectively which gave a perfect surface. It was realized through those experiments that it is a good solution to use a higher load during metallography to achieve a better surface and then remove the induced work hardening layer on the surface using electropolishing.

Appendix II

Sample surface preparation considerations

We have tried to remove/reduce the extrinsic barriers to dislocation motion. Main source of those barriers are: Impurity atoms (alloying), Precipitates, Grain boundaries, Surface films (such as oxides) and Twin boundaries. The purpose is to concentrate on the intrinsic resistance to plastic deformation which is the internal resistance of crystal structure to movement of dislocation [18].

Because of the nature of Nano indentation and SEM/EBSD investigation, it is necessary to prepare the sample in a way that surface finish is flawless. Enough care must be given to avoid creating residual stress on the surface. Residual stress will have an effect on the result depends on being compression or tension state in which neither is going to result in the right hardness. Compression residual stress makes the indent impression to become smaller and tension residual stress has an opposite effect. Enough care must be taken into account that preparation gives a surface which causes Kikuchi patterns to be revealed perfectly. Through Kikuchi pattern a sound crystallographic orientation and later on microstructural investigation can be done. The quality of the diffraction pattern, which influences the confidence of the indexing of the diffraction pattern, depends on removal of damage in the lattice during specimen preparation.

On the other hand, surface finish is not the only factor since a work-hardened layer might be created on the surface which brings error into the hardness measurement [179]. A set of tests were done on Copper and Nickel which revealed the importance of sample preparation and it effect on indentation size effect. As shown in picture 88, Cu111 with two different electropolishing duration and another one with different voltage and electropolishing duration as final step in preparation were examined for indentation size effect, though the size effect can be clearly seen on all three, however, the hardness in all cases is higher than the hardness of the sample which were used in this study. The reason can be related to using of higher load (30mN) during grinding and polishing process which created a thicker work-hardened layer that cannot be removed completely by electropolishing. Special care should be given to choosing of the right sample preparation parameters. Since there is a trade of between removing scratches from the surface by increasing the load and increasing the thickness of the work-hardened layer by increasing the load. One should not assume to increase the load during sample preparation to create a flawless surface and then remove the top layer using electropolish as our experiments showed that is not how it works. A comprehensive study on nickel indicates the same consequence of sample preparation on indentation size effect and hardness [180].

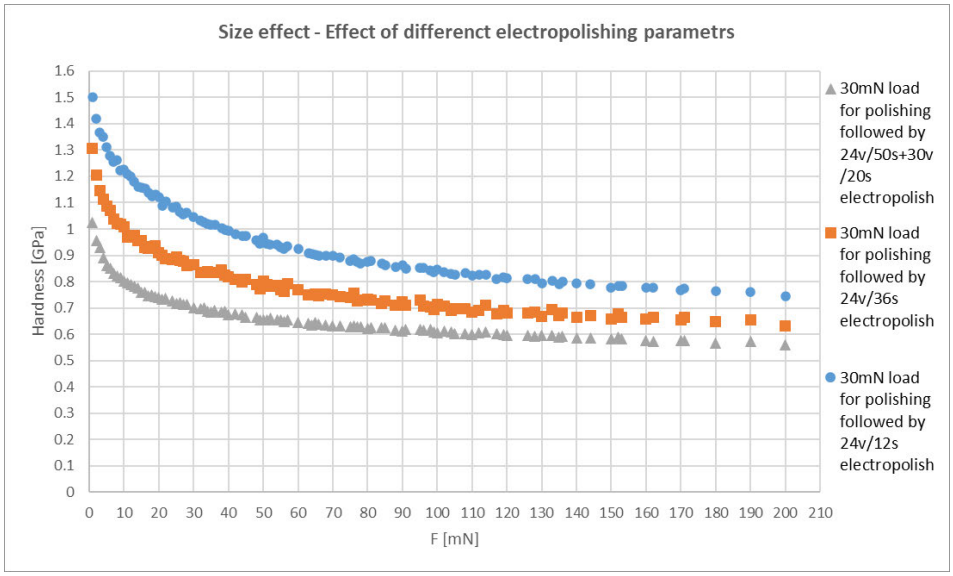

Fig. 88: Effect of sample preparation on indentation size effect

Appendix III

Considerations for performing Nanoindentation testing

The reliability of the results depends on sensitivity of observing and elimination of undesired factors. There are five main sources of uncertainties which can affect test results obtained by nano-indentation testing: 1- Force, 2- Displacement, 3- Stiffness (frame compliance), 4- Zero surface and 5- Area function. In order to tackle those sources of uncertainty, we went through detection, calibration, and adjustment processes for them:

1 and 2) Force and displacement were calibrated during installation of the equipment and during calibration it was found out that there is 0.3% inaccuracy in displacement measurement. According to ISO 14577, inaccuracy in displacement calibration is acceptable up to maximum 1%. Stiffness (frame compliance) measurement, calibration and adjustment has been investigated thoroughly.

3) Analysis of the indentation load-displacement curves was carried out using the well-known method proposed by Oliver and Pharr [88]. The frame compliance of the machine (0.23 nm/mN) and the thermal drift was corrected first and then the power law was fitted to the unloading curve.

4) Zero-point correction i.e. point of first contact between indenter and sample surface is checked automatically after testing and can be corrected manually. Moreover, extra surface detection points were employed on each sample in different locations to avoid this source of uncertainties to occur.

5) The area of indenter impression was found out by atomic force microscopy and the applied force was divided by that area to calculate the hardness.

Another aspect of nano indentation testing which its importance is being sometimes overlooked is creep. As illustrated in figure 14 and 15, one phase each nano indentation testing includes a holding period time for completion of time dependent deformation (creep) to happen. Creep is characterized as plastic deformation as a result of constant stress. It is a stress-activated, time-dependant and material-dependant phenomena. The highly controlled applied loads of the nanoindentation system can provide sensitive creep displacement measurements on materials. Holding period and/or unloading period were adjusted to full fill the mentioned criteria:

Equation 4-1 $$q_f > 10 \times q_c/C_t$$

q_F is the force removal rate; q_c is the contact creep rate at F_{max}; C_T is the measured compliance. Creep influences the measurement through variation in maximum depth and also the gradient of the upper part of unloading. The first one brings inaccuracy in hardness measurement and the second one affect measurement of stiffness and elastic modulus [181].

Creep is an on-going debate in this field of study and its importance should not be ignored since it will eventually affect measured hardness through changing measured contact area. By having more holding time, more creep will happen which means more plastic deformation during indentation. Therefore, contact area is going to be bigger which results is lower value for measured hardness and vice versa when shorter holding time is applied.

Additionally, creep and creep rate can lead to an error in measured stiffness which directly affects measured elastic modulus and eventually affects measured hardness through incorrect h_c which is used for contact area calculation.

Bearing in mind that indentation creep can be equal to load relaxation. During constant load period, both the microstructure of the material and the high contact stresses start to relax. The relaxation takes place because of (1) changes in the contact profile and, (2) redistribution of the localized strain field and dislocations in the deformed volume [148].

Loading rate can alters hardness in some way the same way as creep. Having lower strain rate gives sample more time to reach to the desirable force and therefore, more time is given to creep to take place during loading period since creep is happening during loading period as well.

Appendix IV

Matlab-based image analysis code

A Matlab-based image analysis code [150] was developed to automatically measure the indentation depth, projected area, contact depth, and contact area. This Matlab program provides users to import AFM images of the indents and then read the AFM image data using user define function to identify the size of the image and Image Array (pixel data). These pixel data are converted to height data and then the lowest height of the generated Image Array is set as the bottom point of the residual impression. The distance to the nearest edge is found and set to be the radius (R) of a circle. The line profiles of length R at each user-defined angel in degrees step for 360 degrees are drawn starting from the bottom point. R number of points along each line are generated. The nearest neighbour method is used to assign a pixilation value to each point. In order to increase the accuracy of the pixilation value assigned, each cell of the image array can be divided into small cells where values for the small cells would be estimated using spline interpolation. The maximum value along each line that has the highest distance from the endpoint of the line is set as the peak point of the pile-up or sink-in. A surface plane is then defined by taking the mean of the height array excluding the data points below the peak point of each line. A temporary value of depth for the residual plastic impression is then defined as the difference between mean surface height and the minimum value of the height array. This value is used to set a minimum depth point from the surface to have a contact point. Then the second derivative at every point along each line is calculated. The maximum second derivative which is nearest to the peak point and lies furthest to the minimum depth point is selected as the last contact point. Moreover, in order to eliminate the abnormal values chosen as the last contact point a predefined threshold value depending on the surface quality is used. The elimination process is done by comparing each last contact point with the mean of the preceding and following two values. If any abnormality is detected, then the value corresponding to that point is deleted and the new value is assigned as the last contact point taking the mean of the preceding and following three values. The last contact point corresponds to each line are resolved to get row and column data of an array. The row and column data are then used to calculate the area enclosed by the polygon and converted to an actual area using the actual X and Y scan sizes of the AFM Image.

Bibliography:

[1] X. Hou and N. M. Jennett, “Application of a modified slip-distance theory to the indentation of single-crystal and polycrystalline copper to model the interactions between indentation size and structure size effects,” *Acta Mater.*, vol. 60, no. 10, pp. 4128–4135, 2012.

[2] L. Zhou and Y. Yao, “Single crystal bulk material micro/nano indentation hardness testing by nanoindentation instrument and AFM,” *Mater. Sci. Eng. A*, vol. 460–461, pp. 95–100, 2007.

[3] W. D. Nix and H. Gao, “Indentation Size Effects in Crystalline Materials: A Law for Strain Gradient Plasticity,” *J. Mech. Phys. Solids*, vol. 46, no. 3, pp. 411–425, 1998.

[4] N. A. Fleck, G. M. Muller, M. F. Ashby, and J. W. Hutchinson, “Strain gradient plasticity: Theory and experiment,” *Acta Metall. Mater.*, vol. 42, no. 2, pp. 475–487, 1994.

[5] N. A. Fleck and J. W. Hutchinsons, “A Phenomenological Theory For Strain,” *J. Mech. Phys. Solids*, vol. 41, pp. 1825–1857, 1993.

[6] N. A. Stelmashenko, M. G. Walls, L. M. Brown, and Y. V. Milman, “Microindentations on W and Mo oriented single crystals: An STM study,” *Acta Metall. Mater.*, vol. 41, no. 10, pp. 2855–2865, 1993.

[7] M. S. D. E. Guzman, G. Neubauer, P. Flinn, and D. Nix, “The Role of Indentation Depth on the Measured Hardness of Materials,” *MRS Proc.*, vol. 308, no. 1, pp. 613–618, 1993.

[8] J. Kiely and J. Houston, “Nanomechanical properties of Au (111), (001), and (110) surfaces,” *Phys. Rev. B - Condens. Matter Mater. Phys.*, vol. 57, no. 19, pp. 12588–12594, 1998.

[9] J. William D. Callister, *Materials Science and Engineering An Introduction*, vol. 344, no. 11. 2007.

[10] A. G. Jackson, *Handbook of Crystallography For Electron Microscopists and Others*. Springer, 1991.

[11] D. Hull and D. J. Bacon, *Introductions to Dislocations*, Fifth. Elsevier, 2011.

[12] M. A. Meyers, O. Vöhringer, and V. A. Lubarda, “The onset of twinning in metals: A constitutive description,” *Acta Mater.*, vol. 49, no. 19, pp. 4025–4039, 2001.

[13] K. M. Davoudi and J. J. Vlassak, “Dislocation evolution during plastic deformation: Equations vs. discrete dislocation dynamics study,” *J. Appl. Phys.*, vol. 123, no. 8, pp. 1–23, 2018.

[14] M. F. Ashby and D. R. H. Jones, *Engineering Materials I An Introduction to Properties,*

Application and Design. 2005.

[15] G. E. Dieter, *Mechanical Metallurgy*. 1986.

[16] I. M. Hutchings, "The contributions of David Tabor to the science of indentation hardness," *J. Mater. Res.*, vol. 24, no. 3, pp. 581–589, 2009.

[17] J. Rösler, H. Harders, and M. Baeker, *Mechanical Behaviour of Engineering Materials*. 2007.

[18] J. J. Gilman, *Chemistry and Physics of Mechanical Hardness*. 2009.

[19] George W. Pearsall and John Wulff William G. Moffatt, *The Structure and Properties of Materials. Volume 1. Structure*. John Wiley & Sons, Inc., 1964.

[20] E. Arzt, "Size Effects in Materials Due to Microstructural and Dimensional Constraints: A Comparative Review," *Acta Mater.*, vol. 46, no. 16, pp. 5611–5626, 1998.

[21] J. W. Hutchinson, "Plasticity at the micron scale," *Int. J. Solids Struct.*, vol. 37, pp. 225–238, 2000.

[22] H. Gao and Y. Huang, "Geometrically necessary dislocation and size-dependent plasticity," *Scr. Mater.*, vol. 48, no. 2, pp. 113–118, 2003.

[23] G. Z. Voyiadjis and M. Yaghoobi, *Introduction: Size effects in materials*, no. 1638. 2019.

[24] M. D. Uchic, P. A. Shade, and D. M. Dimiduk, "Micro-compression testing of fcc metals: A selected overview of experiments and simulations," *Jom*, vol. 61, no. 3, pp. 36–41, 2009.

[25] M. D. Uchic, P. A. Shade, and D. M. Dimiduk, "Plasticity of micrometer-scale single crystals in compression," *Annu. Rev. Mater. Res.*, vol. 39, pp. 361–386, 2009.

[26] A. S. Schneider, B. G. Clark, C. P. Frick, and E. Arzt, "Correlation between activation volume and pillar diameter for Mo and Nb BCC pillars," *Mater. Res. Soc. Symp. Proc.*, vol. 1185, pp. 75–79, 2009.

[27] A. S. Schneider, B. G. Clark, C. P. Frick, P. A. Gruber, and E. Arzt, "Effect of orientation and loading rate on compression behavior of small-scale Mo pillars," *Mater. Sci. Eng. A*, vol. 508, no. 1–2, pp. 241–246, 2009.

[28] D. Kaufmann, R. Mönig, C. A. Volkert, and O. Kraft, "Size dependent mechanical behaviour of tantalum," *Int. J. Plast.*, vol. 27, no. 3, pp. 470–478, 2011.

[29] P. Moreau *et al.*, "Measurement of the size effect in the yield strength of nickel foils," *Philos. Mag. Lett.*, vol. 85, no. 7, pp. 339–343, 2005.

[30] S. Brinckmann, J. Y. Kim, and J. R. Greer, “Fundamental differences in mechanical behavior between two types of crystals at the nanoscale,” *Phys. Rev. Lett.*, vol. 100, no. 15, pp. 1–4, 2008.

[31] D. Liu *et al.*, “Toward a further understanding of size effects in the torsion of thin metal wires: An experimental and theoretical assessment,” *Int. J. Plast.*, vol. 41, pp. 30–52, 2013.

[32] J. S. Stölken and A. G. Evans, “A microbend test method for measuring the plasticity length scale,” *Acta Mater.*, vol. 46, no. 14, pp. 5109–5115, 1998.

[33] D. J. Dunstan *et al.*, “Micromechanical testing with microstrain resolution,” *Rev. Sci. Instrum.*, vol. 093906, no. 82, 2011.

[34] E. Tarleton, D. S. Balint, J. Gong, and A. J. Wilkinson, “A discrete dislocation plasticity study of the micro-cantilever size effect,” *Acta Mater.*, vol. 88, pp. 271–282, 2015.

[35] M. Atkinson, “Further analysis of the size effect in indentation hardness tests of some metals,” *J. Mater. Res.*, vol. 10, no. July, pp. 2908–2915, 1995.

[36] GANE N, “Direct Measurement of the Strength of Metals on a Submicrometer Scal,” vol. 317, no. 1530, pp. 367–391, 1970.

[37] N. Gane and J. M. Cox, “The micro-hardness of metals at very low loads,” *Philos. Mag.*, vol. 22, no. 179, pp. 881–891, 1970.

[38] W. C. Oliver and G. M. Pharr, “Nanoindentation in materials research: Past, present, and future,” *MRS Bull.*, vol. 35, no. 11, pp. 897–907, 2010.

[39] Q. Ma and D. R. Clarke, “Size dependent hardness of silver single crystals,” *J. Mater. Res.*, vol. 10, no. 4, pp. 853–863, 1995.

[40] G. Z. Voyiadjis and M. Yaghoobi, “Review of nanoindentation size effect: Experiments and atomistic simulation,” *Crystals*, vol. 7, no. 10, pp. 8–10, 2017.

[41] E. Demir, D. Raabe, N. Zaafarani, and S. Zaefferer, “Investigation of the indentation size effect through the measurement of the geometrically necessary dislocations beneath small indents of different depths using EBSD tomography,” *Acta Mater.*, vol. 57, no. 2, pp. 559–569, 2009.

[42] G. Po, M. S. Mohamed, T. Crosby, C. Erel, A. El-Azab, and N. Ghoniem, “Recent Progress in Discrete Dislocation Dynamics and Its Applications to Micro Plasticity,” *Jom*, vol. 66, no. 10, pp. 2108–2120, 2014.

[43] H. G. M. Kreuzer and R. Pippan, “Discrete dislocation simulation of nanoindentation,” *Comput. Mech.*, vol. 33, no. 4, pp. 292–298, 2004.

[44] G. Z. Voyiadjis and M. Yaghoobi, “Large scale atomistic simulation of size effects during nanoindentation: Dislocation length and hardness,” *Mater. Sci. Eng. A*, vol. 634, pp. 20–31, 2015.

[45] M. Yaghoobi and G. Z. Voyiadjis, “Effect of boundary conditions on the MD simulation of nanoindentation,” *Comput. Mater. Sci.*, vol. 95, pp. 626–636, 2014.

[46] M. Yaghoobi and G. Z. Voyiadjis, “Atomistic simulation of size effects in single-crystalline metals of confined volumes during nanoindentation,” *Comput. Mater. Sci.*, vol. 111, pp. 64–73, 2016.

[47] G. Z. Voyiadjis and M. Yaghoobi, “Role of grain boundary on the sources of size effects,” *Comput. Mater. Sci.*, vol. 117, pp. 315–329, 2016.

[48] M. R. Maughan, A. A. Leonard, D. D. Stauffer, and D. F. Bahr, “The effects of intrinsic properties and defect structures on the indentation size effect in metals,” *Philos. Mag.*, vol. 97, no. 22, pp. 1902–1920, 2017.

[49] J. H. Wu, W. Y. Tsai, J. C. Huang, C. H. Hsieh, and G. R. Huang, “Sample size and orientation effects of single crystal aluminum,” *Mater. Sci. Eng. A*, vol. 662, pp. 296–302, 2016.

[50] A. A. E. D.E. Stegall, M.A. Mamun, “The Role of Stacking Fault Energy on the Indentation Size Effect of FCC Pure Metals and Alloys,” *Mater. Res. Soc. Symp. Proc.*, vol. 1424, 2012.

[51] J. Alcalá, R. Dalmau, O. Franke, M. Biener, J. Biener, and A. Hodge, “Planar defect nucleation and annihilation mechanisms in nanocontact plasticity of metal surfaces,” *Phys. Rev. Lett.*, vol. 109, no. 7, 2012.

[52] X. Ma, W. Higgins, Z. Liang, D. Zhao, G. M. Pharr, and K. Y. Xie, “Exploring the origins of the indentation size effect at submicron scales,” *Proc. Natl. Acad. Sci. U. S. A.*, vol. 118, no. 30, pp. 1–7, 2021.

[53] C. Zhou, I. J. Beyerlein, and R. Lesar, “Plastic deformation mechanisms of fcc single crystals at small scales,” *Acta Mater.*, vol. 59, no. 20, pp. 7673–7682, 2011.

[54] L. Wang, Z. Zhang, and X. Han, “In situ experimental mechanics of nanomaterials at the atomic scale,” *NPG Asia Mater.*, vol. 5, no. 2, pp. 1–11, 2013.

[55] J. Varillas, J. Očenášek, J. Torner, and J. Alcalá, “Understanding imprint formation, plastic

instabilities and hardness evolutions in FCC, BCC and HCP metal surfaces," *Acta Mater.*, vol. 217, 2021.

[56] O. Kraft, P. A. Gruber, R. Mönig, and D. Weygand, "Plasticity in confined dimensions," *Annu. Rev. Mater. Res.*, vol. 40, pp. 293–317, 2010.

[57] D. M. Dimiduk, M. D. Uchic, and T. A. Parthasarathy, "Size-affected single-slip behavior of pure nickel microcrystals," *Acta Mater.*, vol. 53, no. 15, pp. 4065–4077, 2005.

[58] E. Demir, D. Raabe, and F. Roters, "The mechanical size effect as a mean-field breakdown phenomenon: Example of microscale single crystal beam bending," *Acta Mater.*, vol. 58, no. 5, pp. 1876–1886, 2010.

[59] M. F. Ashby, "The deformation of plastically non-homogeneous materials," *Philos. Mag.*, vol. 21, no. 170, pp. 399–424, 1970.

[60] Z. Zong, J. Lou, O. O. Adewoye, A. A. Elmustafa, F. Hammad, and W. O. Soboyejo, "Indentation size effects in the nano and microhardness of FCC single crystal metals," *Mater. Manuf. Process.*, 2007.

[61] J. Wang, "Characterization of the size-dependent indentation behavior and dislocation structures of single-crystalline tungsten," Karlsruher Instituts für Technologie (KIT), 2021.

[62] J. R. Greer, W. C. Oliver, and W. D. Nix, "Size dependence of mechanical properties of gold at the micron scale in the absence of strain gradients," *Acta Mater.*, vol. 53, no. 6, pp. 1821–1830, 2005.

[63] M. D. Uchic, D. M. Dimiduk, J. N. Florando, and W. D. Nix, "Sample dimensions influence strength and crystal plasticity," *Science (80-.).*, vol. 305, no. 5686, pp. 986–989, 2004.

[64] Z. C. Cordero, B. E. Knight, and C. A. Schuh, "Six decades of the Hall–Petch effect – a survey of grain-size strengthening studies on pure metals," *Int. Mater. Rev.*, vol. 61, no. 8, pp. 495–512, 2016.

[65] N. Hansen, "Hall-petch relation and boundary strengthening," *Scr. Mater.*, vol. 51, no. 8 SPEC. ISS., pp. 801–806, 2004.

[66] S. N. Naik and S. M. Walley, "The Hall–Petch and inverse Hall–Petch relations and the hardness of nanocrystalline metals," *J. Mater. Sci.*, vol. 55, no. 7, pp. 2661–2681, 2020.

[67] Y. Li, A. J. Bushby, and D. J. Dunstan, "The Hall – Petch effect as a manifestation of the general size effect Subject Areas :," 2016.

[68] X. D. Hou, A. J. Bushby, and N. M. Jennett, “Study of the interaction between the indentation size effect and Hall-Petch effect with spherical indenters on annealed polycrystalline copper,” *J. Phys. D. Appl. Phys.*, vol. 41, no. 7, 2008.

[69] H. Conrad, S. Feuerstein, and L. Rice, “Effects of grain size on the dislocation density and flow stress of niobium,” *Mater. Sci. Eng.*, vol. 2, no. 3, pp. 157–168, 1967.

[70] U. Messerschmidt, *Dislocation Dynamics During Plastic Deformation*. 2010.

[71] A. J. Bushby, T. T. Zhu, and D. J. Dunstan, “Slip distance model for the indentation size effect at the initiation of plasticity in ceramics and metals,” *J. Mater. Res.*, vol. 24, no. 3, pp. 966–972, 2009.

[72] X. Hou, “Geometrical Size Effects in the Plasticity of Metals by Micromechanical Testing,” no. March, pp. 1–164, 2009.

[73] A. A. H. Ameri, N. N. Elewa, M. Ashraf, and J. P. Escobedo-Diaz, “General methodology to estimate the dislocation density from microhardness measurements,” *Mater. Charact.*, vol. 131, no. January, pp. 324–330, 2017.

[74] W. T. R. F. C. FRANK, “Multiplication Processes for Slow Moving Dislocations,” *Phys. Rev.*, vol. 79, pp. 722–723, 1950.

[75] S. Xu, L. Xiong, Y. Chen, and D. L. Mcdowell, “An analysis of key characteristics of the Frank-Read source process in FCC metals,” *J. Mech. Phys. Solids*, vol. 96, pp. 460–476, 2016.

[76] W. D. Nix and H. Gao, “Indentation size effects in crystalline materials: A law for strain gradient plasticity,” *J. Mech. Phys. Solids*, vol. 46, no. 3, pp. 411–425, 1998.

[77] A. Gouldstone, N. Chollacoop, M. Dao, J. Li, A. M. Minor, and Y. L. Shen, “Indentation across size scales and disciplines: Recent developments in experimentation and modeling,” *Acta Mater.*, vol. 55, no. 12, pp. 4015–4039, 2007.

[78] A. C. Fischer-Cripps, “Critical review of analysis and interpretation of nanoindentation test data,” *Surf. Coatings Technol.*, vol. 200, no. 14–15, pp. 4153–4165, 2006.

[79] G. Genta, G. Maculotti, G. Barbato, R. Levi, and M. Galetto, “Effect of contact stiffness and machine calibration in nano-indentation testing,” *Procedia CIRP*, vol. 78, pp. 208–212, 2018.

[80] M. F. Doerner and W. D. Nix, “A method for interpreting the data from depth-sensing indentation instruments,” *J. Mater. Res.*, vol. 1, no. 4, pp. 601–609, 1986.

[81] A. C. Fischer-Cripps, *Nanoindentation*, Third. Springer, 2011.

[82] I. hardness testing Technical Committee ISE/101/5, "ISO 14577-2:2015 Metallic materials — Instrumented indentation test for hardness and materials parameters — Part 2: Verification and calibration of testing machines," *Br. Stand. Inst.*, 2015.

[83] TABOR D, "The hardness of solids," *Rev Phys Technol*, vol. 1, no. 3, pp. 145–179, 1970.

[84] F. Yang, J. C. M. Li, and W. D. Nix, *Micro and Nano Mechanical Testing of Materials and Devices*. .

[85] T. B. Britton, H. Liang, F. P. E. Dunne, and A. J. Wilkinson, "The effect of crystal orientation on the indentation response of commercially pure titanium: Experiments and simulations," *Proc. R. Soc. A Math. Phys. Eng. Sci.*, vol. 466, no. 2115, pp. 695–719, 2010.

[86] C. Zambaldi, C. Zehnder, and D. Raabe, "Orientation dependent deformation by slip and twinning in magnesium during single crystal indentation," *Acta Mater.*, vol. 91, pp. 267–288, 2015.

[87] W.C. Oliver and G.M. Pharr (1992)., "An improved technique for determining hardness and elastic modulus using load and displacement sensing indentation experiments.," *Journal of Materials Research*, vol. 7. pp. 1564–1583, 1992.

[88] W. C. Oliver and G. M. Pharr, "Measurement of hardness and elastic modulus by instrumented indentation: Advances in understanding and refinements to methodology," *J. Mater. Res.*, vol. 19, no. 1, pp. 3–20, 2004.

[89] K. W. McElhaney, J. J. Vlassak, and W. D. Nix, "Determination of indenter tip geometry and indentation contact area for depth-sensing indentation experiments," *J. Mater. Res.*, vol. 13, no. 5, pp. 1300–1306, 1998.

[90] S. Kucharski and D. Jarząbek, "Depth dependence of nanoindentation pile-up patterns in copper single crystals," *Metall. Mater. Trans. A Phys. Metall. Mater. Sci.*, vol. 45, no. 11, pp. 4997–5008, 2014.

[91] Y. Wang, D. Raabe, C. Klüber, and F. Roters, "Orientation dependence of nanoindentation pile-up patterns and of nanoindentation microtextures in copper single crystals," *Acta Mater.*, vol. 52, no. 8, pp. 2229–2238, 2004.

[92] S. P. Ju, C. T. Wang, C. H. Chien, J. C. Huang, and S. R. Jian, "The nanoindentation responses of nickel surfaces with different crystal orientations," *Mol. Simul.*, vol. 33, no. 11, pp. 905–917,

2007.

[93] M. Liu, C. Lu, K. A. Tieu, C. T. Peng, and C. Kong, “A combined experimental-numerical approach for determining mechanical properties of aluminum subjects to nanoindentation,” *Sci. Rep.*, vol. 5, no. January, pp. 1–16, 2015.

[94] K. Herrmann, N. M. Jennett, W. Wegener, J. Meneve, K. Hasche, and R. Seemann, “Progress in determination of the area function of indenters used for nanoindentation,” *Thin Solid Films*, vol. 377–378, pp. 394–400, 2000.

[95] T. Chudoba and N. M. Jennett, “Higher accuracy analysis of instrumented indentation data obtained with pointed indenters,” *J. Phys. D. Appl. Phys.*, vol. 41, no. 21, 2008.

[96] Technical and I. hardness testing Committee ISE/101/5, “ISO 14577-1:2015 Metallic materials — Instrumented indentation test of hardness and materials parameters Part 1 : Test method,” *Br. Stand. Inst.*, 2015.

[97] C. A. Schuh, “Nanoindentation studies of materials,” *Mater. Today*, vol. 9, no. 5, pp. 32–40, 2006.

[98] T. Ebisu and S. Horibe, “Analysis of the indentation size effect in brittle materials from nanoindentation load-displacement curve,” *J. Eur. Ceram. Soc.*, vol. 30, no. 12, pp. 2419–2426, 2010.

[99] P. S. FollanSbee, *Fundamentals of Strength*. John Wiley & Sons, Inc., 2014.

[100] R. E. R.-H. Reza Abbaschian, *Physical Metallurgy Principles*, no. Fourth Edition. Cengage Learning, 2009.

[101] W. F. Hosford, *Mechanical Behavior of Materials*. 2010.

[102] J. Gubicza, “Defect Structure in Low Stacking Fault Energy Nanomaterials,” *Defect Struct. Prop. Nanomater.*, no. 111, pp. 95–119, 2017.

[103] B. E. P. Beeston, I. L. Dillamore, and R. . Smallman, “The Stacking-Fault Energy of Some Nickel-Cobalt Alloys,” *Met. Sci. J.*, vol. 2, 1968.

[104] C. B. Carter and S. M. Holmes, “The stacking-fault energy of nickel,” *Philos. Mag.*, vol. 35, no. 5, pp. 1161–1171, 1977.

[105] Z. Yan and Y. Lin, “On the widths of stacking faults formed by dissociation of different types of full dislocations in a nanostructured Al alloy,” *Mater. Sci. Eng. A*, vol. 770, no. May 2019, p.

138532, 2020.

[106] J. Lu *et al.*, “Stacking fault energies in austenitic stainless steels,” *Acta Mater.*, vol. 111, pp. 39–46, 2016.

[107] J. W. Christian and S. Mahajan, “Deformation twinning,” *Prog. Mater. Sci.*, vol. 39, no. 1–2, pp. 1–157, 1995.

[108] I. L. Dillamore and R. E. Smallman, “The stacking-fault energy of F.C.C. metals,” *Philos. Mag.*, vol. 12, no. 115, pp. 191–193, 1965.

[109] E. Aerts, P. Delavignette, R. Siems, and S. Amelinckx, “Stacking fault energy in silicon,” *J. Appl. Phys.*, vol. 33, no. 10, pp. 3078–3080, 1962.

[110] A. W. Ruff, “Measurement of stacking fault energy from dislocation interactions,” *Metall. Trans.*, vol. 1, no. 9, pp. 2391–2413, 1970.

[111] R. E. Smallman and P. S. Dobson, “Stacking fault energy measurement from diffusion,” *Metall. Trans.*, vol. 1, no. 9, pp. 2383–2389, 1970.

[112] V. Vitek, “Multilayer stacking faults and twins on (211) planes in b.c.c. metals,” *Scr. Metall.*, vol. 4, no. 9, pp. 2–9, 1970.

[113] V. Vítek, “Intrinsic stacking faults in body-centred cubic crystals,” *Philos. Mag.*, vol. 18, no. 154, pp. 773–786, 1968.

[114] H. Sun, A. Kumar, and C. V. Singh, “Deformation behavior of BCC tantalum nanolayered composites with modulated layer thicknesses,” *Mater. Sci. Eng. A*, vol. 761, no. February, p. 138037, 2019.

[115] N. I. Medvedeva, Y. N. Gornostyrev, and A. J. Freeman, “Electronic origin of solid solution softening in bcc molybdenum alloys,” *Phys. Rev. Lett.*, vol. 94, no. 13, pp. 1–4, 2005.

[116] A. Machová, G. E. Beltz, and M. Change, “Atomistic simulation of stacking fault formation in bcc iron,” *Model. Simul. Mater. Sci. Eng.*, vol. 7, no. 6, pp. 949–974, 1999.

[117] C. J. Ruestes *et al.*, “Atomistic simulation of tantalum nanoindentation: Effects of indenter diameter, penetration velocity, and interatomic potentials on defect mechanisms and evolution,” *Mater. Sci. Eng. A*, vol. 613, pp. 390–403, 2014.

[118] M. S. Duesbery and V. Vitek, “Plastic Anistropy in B.C.C. Transition Metals,” *Acta Metall.*, vol. 46, no. 5, pp. 1481–1492, 1998.

[119] R. Pegel, “Stacking Faults on {110} Planes in the B.C.C. Lattice,” *phys. stat. sol. 18*, vol. 603, pp. 603–609, 1968.

[120] H. Eichler and B. Pegel, “Intrinsic Stacking Faults on {112} Planes in the B.C.C. Lattice,” vol. 333, pp. 333–338, 1969.

[121] M. Muzyk, Z. Pakiela, and K. J. Kurzydlowski, “Ab initio calculations of the generalized stacking fault energy in aluminium alloys,” *Scr. Mater.*, vol. 64, no. 9, pp. 916–918, 2011.

[122] G. Lu, N. Kioussis, and V. V. Bulatov, “Generalized-stacking-fault energy surface and dislocation properties of aluminum,” *Phys. Rev. B - Condens. Matter Mater. Phys.*, vol. 62, no. 5, pp. 3099–3108, 2000.

[123] P. C. J. Gallagher, “1970, Gallagher P., The influence of alloying, temperature, and related effects on the stacking fault energy.pdf,” vol. I, no. September, 1970.

[124] X. M. Wei, J. M. Zhang, and K. W. Xu, “Generalized stacking fault energy in FCC metals with MEAM,” *Appl. Surf. Sci.*, vol. 254, no. 5, pp. 1489–1492, 2007.

[125] A. Howie and P. R. Swann, “Direct measurements of stacking-fault energies from observations of dislocation nodes,” *Philos. Mag.*, vol. 6, no. 70, pp. 1215–1226, 1961.

[126] J. P. V. M. F. DENANOT, “The stacking fault energy in Cu-Al-Zn alloys,” *phys. stat. sol. g, K125*, vol. 125, pp. 125–127, 1971.

[127] D. J. H. Cockayne, M. L. Jenkins, and I. L. F. Ray, “The measurement of stacking-fault energies of pure face-centred cubic metals,” *Philos. Mag.*, vol. 24, no. 192, pp. 1383–1392, 1971.

[128] K. Q. Li, Z. J. Zhang, L. L. Li, P. Zhang, J. B. Yang, and Z. F. Zhang, “Effective Stacking Fault Energy in Face-Centered Cubic Metals,” *Acta Metall. Sin. (English Lett.*, vol. 31, no. 8, pp. 873–877, 2018.

[129] C. Wang, H. Wang, T. Huang, X. Xue, F. Qiu, and Q. Jiang, “Generalized-stacking-fault energy and twin-boundary energy of hexagonal close-packed Au: A first-principles calculation,” *Sci. Rep.*, vol. 5, no. 5988, pp. 1–11, 2015.

[130] C. C. Bampton, I. P. Jones, and M. H. Loretto, “Stacking fault energy measurements in some austenitic stainless steels,” *Acta Metall.*, vol. 26, no. 1, pp. 39–51, 1978.

[131] J. A. Yan, C. Y. Wang, and S. Y. Wang, “Generalized-stacking-fault energy and dislocation properties in bcc Fe: A first-principles study,” *Phys. Rev. B - Condens. Matter Mater. Phys.*, vol. 70, no. 17, pp. 1–5, 2004.

[132] P. Tu, Y. Zheng, C. Zhuang, X. Zeng, and H. Zhu, “A high-throughput computation framework for generalized stacking fault energies of pure metals,” *Comput. Mater. Sci.*, vol. 159, no. September 2018, pp. 357–364, 2019.

[133] S. Xu, Y. Su, L. T. W. Smith, and I. J. J. Beyerlein, “Frank-Read source operation in six body-centered cubic refractory metals,” *J. Mech. Phys. Solids*, vol. 141, p. 104017, 2020.

[134] R. Hill, “The elastic behaviour of a crystalline aggregate,” *Proc. Phys. Soc. Sect. A*, vol. 65, no. 5, pp. 349–354, 1952.

[135] S. F. Pugh, “XCII. Relations between the elastic moduli and the plastic properties of polycrystalline pure metals,” *London, Edinburgh, Dublin Philos. Mag. J. Sci.*, vol. 45, no. 367, pp. 823–843, 1954.

[136] Joachim Rösler, H. Harders, and M. Baeker, *Mechanical Behaviour of Engineering Materials*. 2007.

[137] J. K. M. W.Boas, “Anisotropy in Metals,” *Prog. Met. Phys.*, vol. 2, pp. 90–120, 1950.

[138] A. Wolfenden, “Dynamic Elastic Modulus Measurements in Materials,” *American Soc. Test. Mater.*, vol. 8, no. 5, p. 229, 2019.

[139] J. Liu, J. Song, and Y. Wei, “Size effects of elastic modulus of fcc metals based on the Cauchy-Born rule and nanoplate models,” *Acta Mech. Solida Sin.*, vol. 27, no. 2, pp. 111–121, 2014.

[140] S. M. Rassoulinejad-Mousavi, Y. Mao, and Y. Zhang, “Evaluation of copper, aluminum, and nickel interatomic potentials on predicting the elastic properties,” *J. Appl. Phys.*, vol. 119, no. 24, pp. 1–3, 2016.

[141] D. Raabe, P. Klose, B. Engl, K. P. Imlau, F. Friedel, and F. Roters, “Concepts for integrating plastic anisotropy into metal forming simulations,” *Adv. Eng. Mater.*, vol. 4, no. 4, pp. 169–180, 2002.

[142] M. N. Gussev and K. J. Leonard, “In situ SEM-EBSD analysis of plastic deformation mechanisms in neutron-irradiated austenitic steel,” *J. Nucl. Mater.*, vol. 517, pp. 45–56, 2019.

[143] W. Zhou, R. Apkarian, Z. L. Wang, and D. Joy, “Fundamentals of scanning electron microscopy (SEM),” *Scanning Microsc. Nanotechnol. Tech. Appl.*, pp. 1–40, 2007.

[144] T. Kogure, *Electron Microscopy*, 2nd ed., vol. 5, no. C. Elsevier Ltd., 2013.

[145] G. E. Lloyd, “Atomic number and crystallographic contrast images with the SEM: a review of

backscattered electron techniques," *Mineral. Mag.*, vol. 51, no. 359, pp. 3–19, 1987.

[146] J. Gubicza, *Characterization Methods of Lattice Defects*. 2017.

[147] W. Pantleon, "Resolving the geometrically necessary dislocation content by conventional electron backscattering diffraction," *Scr. Mater.*, vol. 58, no. 11, pp. 994–997, 2008.

[148] K. Durst and V. Maier, "Dynamic nanoindentation testing for studying thermally activated processes from single to nanocrystalline metals," *Curr. Opin. Solid State Mater. Sci.*, vol. 19, no. 6, pp. 340–353, 2015.

[149] "National Physical Laboratory - Instrumented Indentation Reference Blocks," 2015.

[150] N. Radaliyagoda, "Stronger, lighter, safer, materials by length scale engineering A next-generation, nano-particle-free, 3D additive manufacturing," 2022.

[151] G. Aldrich-Smith, N. M. Jennett, and U. Hangen, "Direct measurement of nanoindentation area function by metrological AFM," *Zeitschrift fuer Met. Res. Adv. Tech.*, vol. 96, no. 11, pp. 1267–1271, 2005.

[152] T. Volz, R. Schwaiger, J. Wang, and S. M. Weygand, "Comparison of three approaches to determine the projected area in contact from finite element Berkovich nanoindentation simulations in tungsten," *IOP Conf. Ser. Mater. Sci. Eng.*, vol. 257, no. 1, 2017.

[153] D. Nečas and P. Klapetek, "Gwyddion: An open-source software for SPM data analysis," *Cent. Eur. J. Phys.*, vol. 10, no. 1, pp. 181–188, 2012.

[154] L. A. Giannuzzi and F. A. Stevie, "A review of focused ion beam milling techniques for TEM specimen preparation," *Micron*, vol. 30, no. 3, pp. 197–204, 1999.

[155] A. Tryblom, "Optimizing Transmission Kikuchi Diffraction for Analysing Grain Size and Orientation of Nanocrystalline Coatings," 2015.

[156] A. J. Cackett, C. D. Hardie, J. J. H. Lim, and E. Tarleton, "Spherical indentation of copper: Crystal plasticity vs experiment," *Materialia*, vol. 7, no. June, 2019.

[157] A. Tryblom, "Optimizing Transmission Kikuchi Diffraction for Analysing Grain Size and Orientation of Nanocrystalline Coatings," no. November, 2015.

[158] X. Z. Liang, M. F. Dodge, J. Jiang, and H. B. Dong, "Using transmission Kikuchi diffraction in a scanning electron microscope to quantify geometrically necessary dislocation density at the nanoscale," *Ultramicroscopy*, vol. 197, no. November 2018, pp. 39–45, 2019.

[159] R. H. Geiss, K. P. Rice, and R. R. Keller, “Transmission EBSD in the Scanning Electron Microscope,” *Micros. Today*, vol. 21, no. 3, pp. 16–20, 2013.

[160] X. Zhang, A. Godfrey, G. Winther, N. Hansen, and X. Huang, “Plastic deformation of submicron-sized crystals studied by in-situ Kikuchi diffraction and dislocation imaging,” *Mater. Charact.*, vol. 70, pp. 21–27, 2012.

[161] R. R. Keller and R. H. Geiss, “Transmission EBSD from 10 nm domains in a scanning electron microscope,” *J. Microsc.*, vol. 245, no. 3, pp. 245–251, 2012.

[162] R. R. Shen, V. Ström, and P. Efsing, “Spatial correlation between local misorientations and nanoindentation hardness in nickel-base alloy 690,” *Mater. Sci. Eng. A*, vol. 674, pp. 171–177, 2016.

[163] W. Wang and K. Lu, “Nanoindentation study on elastic and plastic anisotropies of Cu single crystals,” *Philos. Mag.*, vol. 86, no. 33-35 SPEC. ISSUE, pp. 5309–5320, 2006.

[164] Y. Gao, C. J. Ruestes, D. R. Tramontina, and H. M. Urbassek, “Comparative simulation study of the structure of the plastic zone produced by nanoindentation,” *J. Mech. Phys. Solids*, vol. 75, pp. 58–75, 2015.

[165] Z. Wang *et al.*, “Coupled effect of crystallographic orientation and indenter geometry on nanoindentation of single crystalline copper,” *Int. J. Mech. Sci.*, vol. 148, no. August, pp. 531–539, 2018.

[166] Y. Shibutani, T. Tsuru, and A. Koyama, “Nanoplastic deformation of nanoindentation: Crystallographic dependence of displacement bursts,” *Acta Mater.*, vol. 55, no. 5, pp. 1813–1822, 2007.

[167] N. Naveen Kumar, R. Tewari, P. V. Durgaprasad, B. K. Dutta, and G. K. Dey, “Active slip systems in bcc iron during nanoindentation: A molecular dynamics study,” *Comput. Mater. Sci.*, vol. 77, pp. 260–263, 2013.

[168] G. M. Pharr and W. C. Oliver, “Nanoindentation of silver-relations between hardness and dislocation structure,” *J. Mater. Res.*, vol. 4, no. 1, pp. 94–101, 1989.

[169] D. E. Stegall, B. Crawford, and A. A. Elmustafa, “An examination of the indentation size effect and bi-linear behavior of FCC metals,” *Mater. Res. Soc. Symp. Proc.*, vol. 1424, pp. 85–90, 2012.

[170] G. Z. Voyiadjis, A. H. Almasri, and T. Park, “Experimental nanoindentation of BCC metals,”

Mech. Res. Commun., vol. 37, no. 3, pp. 307–314, 2010.

[171] V. Maier, C. Schunk, M. Göken, and K. Durst, "Microstructure-dependent deformation behaviour of bcc-metals - Indentation size effect and strain rate sensitivity," *Philos. Mag.*, vol. 95, no. 16–18, pp. 1766–1779, 2015.

[172] M. C. Fivel, C. F. Robertson, G. R. Canova, and L. Boulanger, "Three-dimensional modeling of indent-induced plastic zone at a mesoscale," *Acta Mater.*, vol. 46, no. 17, pp. 6183–6194, 1998.

[173] C. F. Robertson and M. C. Fivel, "A study of the submicron indent-induced plastic deformation," *J. Mater. Res.*, vol. 14, no. 6, pp. 2251–2258, 1999.

[174] C. K. Dolph, D. J. da Silva, M. J. Swenson, and J. P. Wharry, "Plastic zone size for nanoindentation of irradiated Fe—9%Cr ODS," *J. Nucl. Mater.*, vol. 481, pp. 33–45, 2016.

[175] K. Durst, B. Backes, and M. Göken, "Indentation size effect in metallic materials: Correcting for the size of the plastic zone," *Scr. Mater.*, vol. 52, no. 11, pp. 1093–1097, 2005.

[176] D. M. Norfleet, D. M. Dimiduk, S. J. Polasik, M. D. Uchic, and M. J. Mills, "Dislocation structures and their relationship to strength in deformed nickel microcrystals," *Acta Mater.*, vol. 56, no. 13, pp. 2988–3001, 2008.

[177] ISO 4287:1997, "Geometrical Product Specifications (GPS) - Surface texture: Profile method - Terms, definitions and surface texture parameters," *Int. Organ. Stand.*, 1997.

[178] "www.Struers.com," pp. 1–9, 2018.

[179] H. Bückle, "Progress in Mcro-Indentation," *Int. Mater. Rev.*, vol. 4, no. 13, 1959.

[180] Z. Wang, "Influences of sample preparation on the indentation size effect Influences of sample preparation on the indentation size effect and nanoindentation pop-in on nickel and nanoindentation pop-in on nickel," 2012.

[181] T. Chudoba and F. Richter, "Investigation of creep behaviour under load during indentation experiments and its influence on hardness and modulus results," *Surf. Coatings Technol.*, vol. 148, no. 2–3, pp. 191–198, 2001.